ML-TDR-64-53

603 75

AN INVESTIGATION OF LOW-CYCLE FATIGUE FAILURES USING APPLIED FRACTURE MECHANICS

106 - P - $2.50

TECHNICAL DOCUMENTARY REPORT ML-TDR-64-53
MAY 1964

AIR FORCE MATERIALS LABORATORY
RESEARCH AND TECHNOLOGY DIVISION
AIR FORCE SYSTEMS COMMAND
WRIGHT-PATTERSON AIR FORCE BASE, OHIO

Project 7381, Task 738101

(Prepared under Contract AF 33(657)-10251 by The Boeing Company, Aero-Space Division, Seattle, Washington 98124; C. F. Tiffany and P. M. Lorenz, authors)

Best
Available
Copy

FOREWORD

This report presents the work accomplished by The Boeing Company from February 15, 1963 to February 15, 1964, in "An Investigation of Low-Cycle Fatigue Failures Using Applied Fracture Mechanics," Contract AF 33(657)-10251. The work was administered by the Air Force Materials Laboratory, Systems Engineering Group, Research and Technology Division, Wright-Patterson Air Force Base, Ohio. The project engineer is Lt Robert M. Dunco, MAAE.

Boeing personnel who participated in the investigation described in this report include C. F. Tiffany, project supervisor; P. M. Lorenz, technical leader; and H. L. Southworth, J. N. Masters, F. A. Pall, A. A. Ottlyck, F. C. Fleming, and V. R. Robinson.

The information contained in this document is also released as Boeing Document D2-23141, dated April 1964.

ABSTRACT

Basic principles of fracture mechanics were applied to the investigation of cyclic flaw growth characteristics of Ladish D6A-C steel, tested at room temperature; 6Al-4V titanium, tested at -320°F; and 18Ni(300) maraging steel, tested at room temperature using uniaxially loaded, preflawed (fatigue cracked) test specimens. Applicability of such data to prediction of the cyclic life span of biaxially loaded pressure vessels has been verified by testing six 17-inch-diameter, preflawed Ladish D6A-C test tanks.

A brief discussion of technical background illustrates the experimental approach and the significance of resulting test data. A method for utilization of NDT inspection and proof-pressure testing in conjunction with the cyclic flaw growth data for design purposes is also presented.

PUBLICATION REVIEW

This technical documentary report has been reviewed and is approved.

FOR THE COMMANDER

W. P. CONRARDY, Chief
Materials Engineering Branch
Materials Applications Division
AF Materials Laboratory

CONTENTS

ILLUSTRATIONS

TABLES

INTRODUCTION

This program is intended to verify the applicability of basic fracture mechanics principles to the problem of premature, low-cycle fatigue failures of high-strength pressure vessels. Examination of such failures indicates that flaws, notches, or other crack-like defects are invariably present at the fracture origin. With stress cycles, these flaws gradually grow until one of them reaches a size large enough for the onset of rapid propagation and failure.

The approach taken in this investigation is based on the premise that, in the absence of uncontrolled metallurgical and environmental variables such as stress-corrosion, hydrogen embrittlement, etc., cyclic flaw growth can be investigated using the Griffith-Irwin stress parameter (K). Determining stress parameter K and measuring crack extensions in test specimens yield test data directly applicable to high-strength pressure vessels fabricated from the same material and subjected to a similar loading profile. The minimum life span of such pressure vessels can be predicted when the size of initial flaws and the operating stress levels are known.

Initial work on this concept was performed during 1960 (Reference 1), using 17-7PH precipitation-hardening steel specimens and pressure vessels. The investigation in the present program is extended to include three additional materials:

1) Ladish D6A-C steel plate 0.50 inch thick, tested at room temperature;

2) 6Al-4V titanium plate 0.50 inch thick, tested at -320°F;

3) 18Ni(300) maraging steel plate 0.25 inch thick, tested at room temperature.

The program consists of three major phases. Phase I is designed to provide preliminary information on the response of Ladish D6A-C and 18Ni(300) steel to heat treatments and to determine mechanical properties and static fracture toughness of 6Al-4V titanium.

Phase II consists of testing sharply notched round bar and flat surface-flawed tensile specimens made from Ladish D6A-C steel and 6Al-4V titanium, and flat surface-flawed and through-the-thickness-cracked tensile specimens made from 18Ni(300) maraging steel. The first two materials were used to demonstrate that, on the basis of the test data obtained using sharply notched round bar specimens, the conditions under which a flaw will become critical before growing through the thickness may be predicted. The 18Ni(300) maraging steel was used to show that conditions under which a flaw will grow through the thickness are likewise predictable on the basis of fracture toughness data.

Manuscript released by the authors 5 March 1964 for publication as an ML Technical Documentary Report.

Phase III is designed to provide verification of the applicability of fracture toughness data to actual pressure vessels. Only Ladish D6A-C was used in this phase. The pressure vessels were 17 inches in diameter and about 52 inches long, with two hemispherical heads. Artificial flaws of predetermined size were introduced into the shell section of all pressure vessels. Two tanks were burst-tested: the remaining four tanks were subjected to cyclic loading of various magnitudes. The cyclic life span of each of the four tanks was then compared with the test data obtained using sharply notched round bars and surface-flawed specimens.

TECHNICAL BACKGROUND

The elastic stress distribution in the vicinity of a crack or sharp-edged flaw tip indicates (References 2 and 3) that the elastic stresses always have the same functional form and differ only by a stress-intensity parameter designated by the symbol K. The stress-intensity parameter, K, is linearly dependent upon the applied gross stress and the square root of the flaw size. With increase in either flaw size or gross stress, the stress intensity increases until it reaches a critical value, when rapid flaw propagation and complete fracture result. The critical K value is denoted as K_c for the plane stress and K_{Ic} for the plane strain conditions.

For surface and embedded flaws, which attain critical size and become unstable prior to growing through the thickness, plane strain or so-called opening mode fracture conditions predominate. For through-the-thickness cracks in relatively thin materials, or for surface and embedded flaws that grow through the thickness before inception of instability, the plane strain conditions are replaced by the plane stress, resulting in a predominantly mixed mode or a shear fracture.

The K_{Ic} and K_c values for a material at a specific temperature can be determined experimentally. Probably the most common specimens for K_{Ic} determination are the sharply notched round bar and the surface-flawed tensile specimens. The stress field intensity for these specimens has been described by Irwin (References 4 and 5), who gives the following formulas for calculation of the plane strain (K_{Ic}) fracture toughness values:

$$K_{Ic} = \frac{0.233\,\sigma_n\sqrt{\pi D}}{\left[1 - \frac{1}{2\pi D}\left(\frac{K_{Ic}}{\sigma_{Y.S.}}\right)^2\right]^2} \qquad \text{(sharply notched round-bar specimen)} \qquad (1)$$

$$K_{Ic} = \frac{1.1\,\sigma\sqrt{\pi a}}{\left[\phi^2 - 0.212\left(\sigma/\sigma_{Y.S.}\right)^2\right]^{1/2}} \qquad \text{(surface-flawed specimen)} \qquad (2)$$

where:

D = shank diameter in inches

d = net diameter in inches

d/D = 0.6 to 0.8

σ = gross area fracture stress (ksi)

σ_n = net area fracture stress (ksi)

$\sigma_{Y.S.}$ = 0.2 percent offset tensile yield strength (ksi)

$$\phi = \int_0^{\pi/2} \left[1 - \left(\frac{c^2 - a^2}{c^2}\right) \sin^2\theta\right]^{1/2} d\theta$$

a = depth of the elliptical surface flaw in inches

$2c$ = length of the elliptical surface flaw in inches

θ = integration variable

Considering the bracketed quantity in the denominator of Equation (2), it will be observed that for a given stress level, the quantity in the brackets is a function of ϕ, which depends upon flaw shape or its length-to-depth ratio. Designating this quantity by a letter Q and calling it a "flaw shape parameter," Equation (2), after rearranging, takes the following form:

$$K_{Ic} = 1.1 \sqrt{\pi}\, \sigma \left(a/Q\right)^{1/2} \tag{3}$$

It is readily seen that the plane strain fracture toughness (K_{Ic}) is proportional to the fracture stress (σ) and the square root of the quantity in brackets (a/Q). The latter, incorporating the flaw depth, a, and the flaw shape parameter, Q, represents flaw size used for calculation of the plane strain (K_{Ic}) fracture toughness values in surface-flawed specimens.

The same relation applies to fully embedded elliptical flaws, except that the 1.1 constant is dropped from Equations (2) and (3). The 1.1 constant was originally introduced by Irwin (Reference 6) to compensate for the stress relaxation of the surface flaw at the exposed corners. Figure 1 shows a plot of the flaw shape parameter (Q) as a function of flaw depth-to-length ratios (a/2c) for different fracture stress levels.

For determination of plane stress (K_c) fracture toughness values, through-the-thickness, centrally cracked sheet specimens are used. The K_c values are calculated (Reference 7) by the use of the following relationship:

$$K_c = \sigma \sqrt{W \tan\left(\frac{\pi a}{W} + \frac{K_c^2}{2W\sigma_{Y.S.}^2}\right)} \quad \text{(thin sheet)} \tag{4}$$

where:

σ = gross area fracture stress (ksi)

$2a$ = critical crack length as measured at the inception of crack instability in inches

W = specimen width in inches

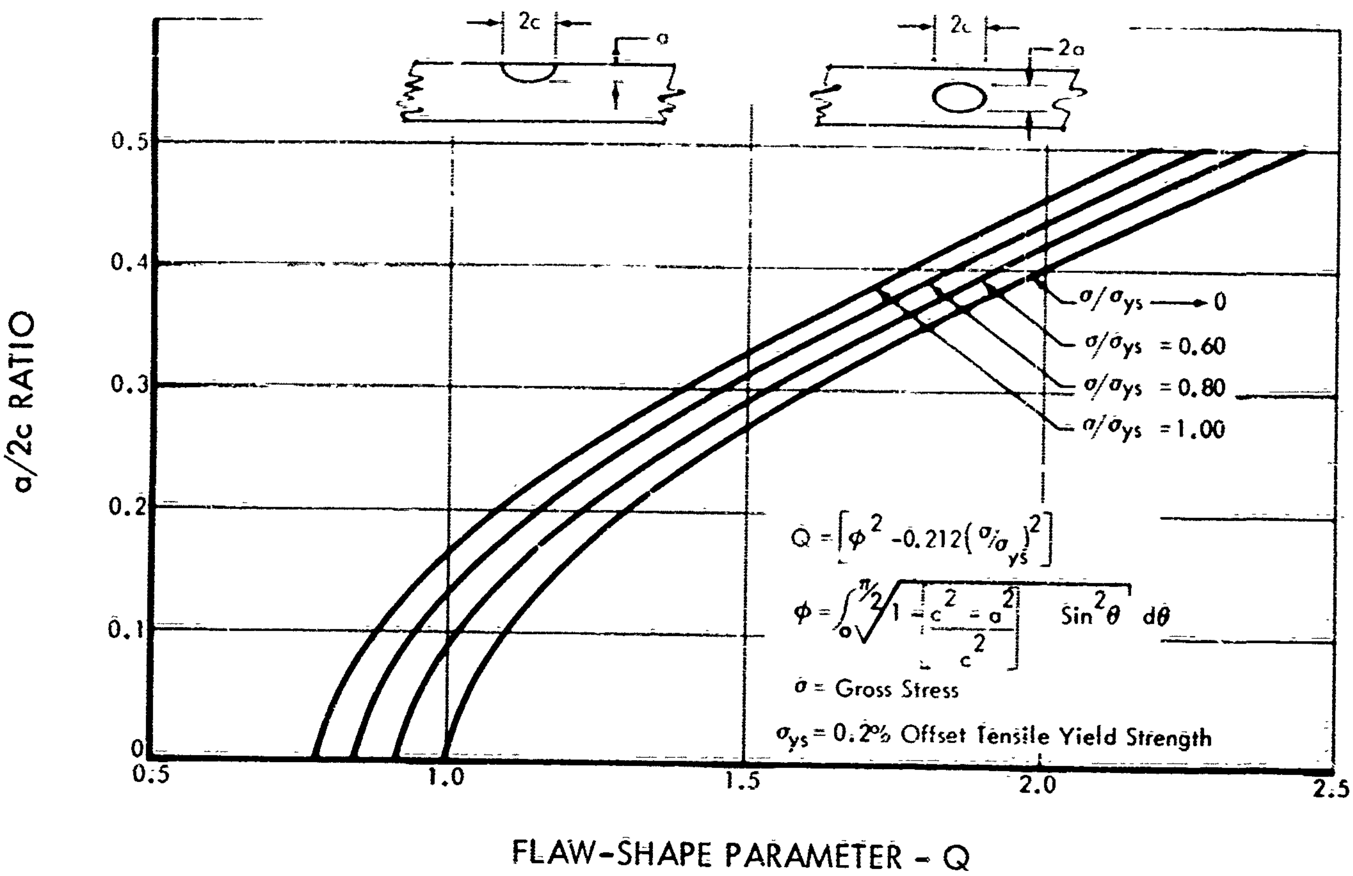

Figure 1: Flaw Shape Parameter Curves for Surface and Internal Cracks

Equation (4) may also be used for calculation of the plane strain value (K_{Ic}) by the testing of relatively thick through-the-thickness centrally cracked plate specimens. For the in-between thicknesses, calculated fracture toughness usually represents some intermediate value. Figure 2 illustrates the transition between thin sheet and thick plate in terms of measured fracture toughness.

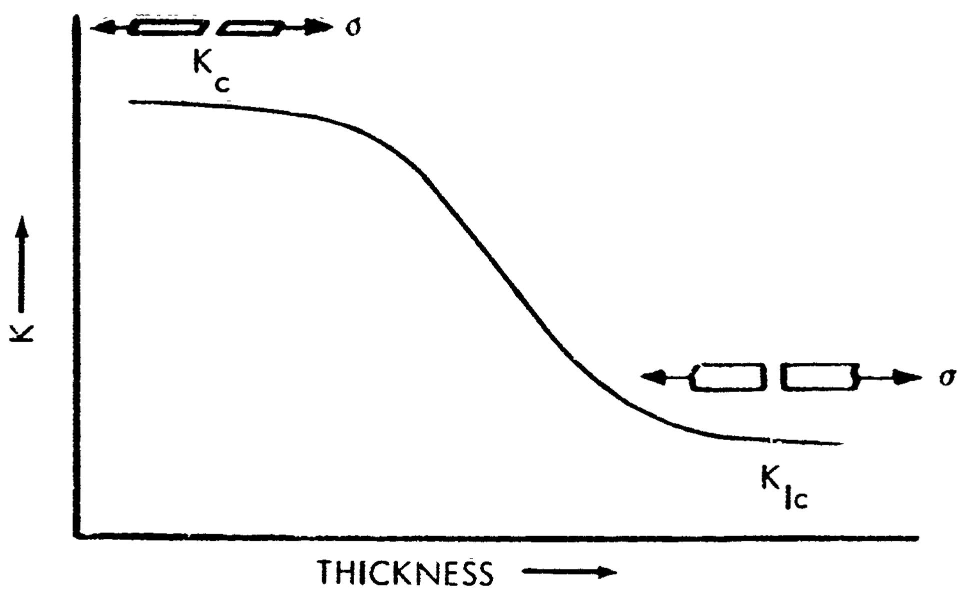

Figure 2: Fracture Mode Transition

In special cases, when the thickness of the material approaches that required for plane strain conditions, a through-the-thickness crack might become unstable (might "pop") during initial loading prior to complete fracture. The initial instability, whenever it is clearly defined, occurs under plane-strain conditions, and the calculated fracture toughness value at the instant of pop becomes representative of the plane strain (K_{Ic}) fracture toughness (Reference 8).

After brief consideration of various test methods for evaluation of plane stress (K_c) and plane strain (K_{Ic}) values of engineering materials, it is appropriate to extend this brief review to a consideration of the relationship between applied stress levels and corresponding flaw or crack sizes in test specimens and structural components, such as pressure vessels, and to illustrate the concept of flaw growth potential as a function of the proof pressure factor.

CRITICAL FLAW SIZE AND FRACTURE STRESSES

The relationship between critical flaw sizes and applied stress levels for a given fracture toughness value may be derived from Equation (3) for plane strain and from Equation (4) for plane stress conditions. For surface-flawed specimens, the relationship is represented schematically in Figure 3.

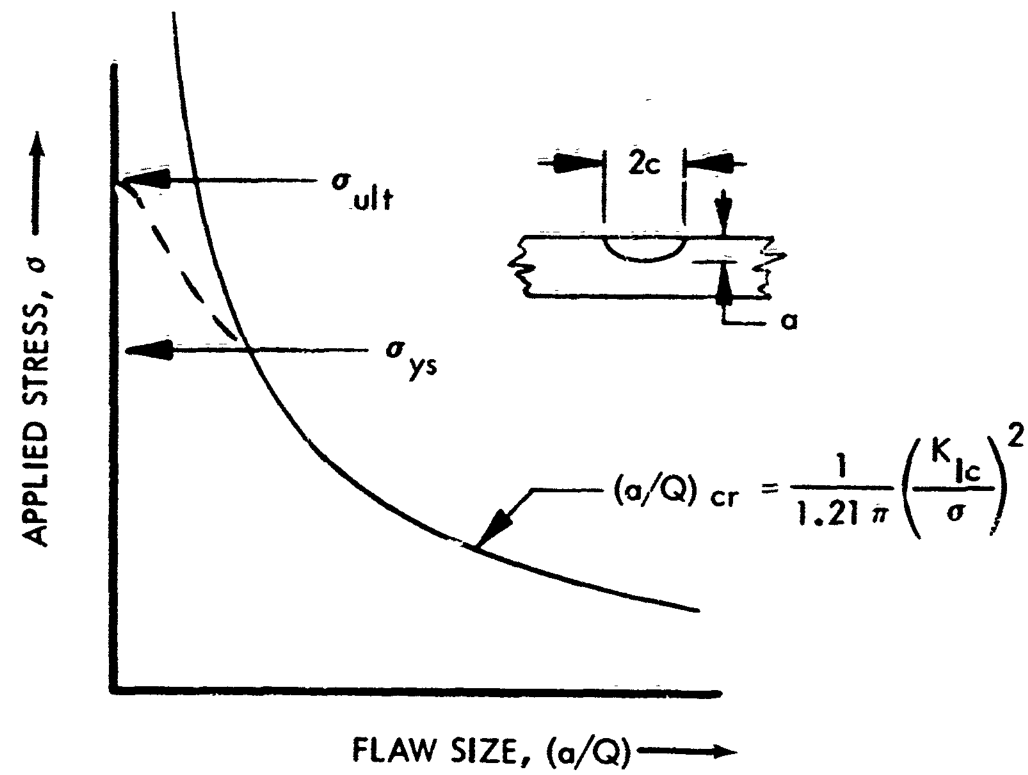

Figure 3: Relationship Between Critical Flaw Sizes and Applied Stress Level

The solid line in Figure 3 represents the theoretical relationship between critical flaw sizes $(a/Q)_{cr}$, and corresponding fracture stresses, σ, as defined by Equation (3). The relationship is found to hold as long as the applied stresses do not exceed uniaxial yield strength, σ_{ys}, of the material. As the applied stresses exceed the uniaxial yield strength, the relationship between stresses and flaw sizes follows some experimentally determined curve (represented schematically by a dotted line) until the ultimate strength of the material, σ_{ult}, is reached. For the present program the applied stresses were selected to be well below the yield strength of the material; consequently, the theoretical relationship between stresses and flaw sizes held at all test stress levels.

As applied to pressure vessels containing inevitable crack-like defects, the critical flaw size represents the size $(a/Q)_{cr}$, required for instability and fracture at a stress level generated by a given internal pressure.

At this point, the flaw exhibits a rapid acceleration in growth, and it can attain a maximum velocity in steel and aluminum alloys of approximately 5000 to 6000 feet per second. If the crack reaches this velocity while the driving forces (stresses) have not diminished, the crack will branch and the pressure vessel will shatter. The more brittle the material the more likely it is that shattering will occur.

In tough or relatively thin materials, the crack velocity is retarded through a combination of local stress relaxation and large plastic deformation, as well as the development of shear lips at the tip of a crack. Under this condition, the limiting velocity may not be reached, and the tank may split rather than shatter. Ensurance against either type of failure requires that the unavoidable sharp flaws or crack-like notches be considerably smaller than the critical size at a given operating stress level. The life span of the pressure vessel will then depend upon the number of cycles or time under sustained loading needed to propagate initial flaws or sharp notches until one of them reaches a critical size.

INITIAL FLAW SIZES AND FLAW GROWTH POTENTIAL

Initial flaws, either pre-existent or introduced during fabrication of pressure vessels, may be determined by nondestructive inspection techniques. As a guarantee against faulty interpretation or an outright error in inspection findings, the maximum possible initial flaw size may be determined by proof-pressure testing of pressure vessels. Knowledge of the maximum possible flaw size, together with the flaw growth characteristics of the pressure vessel material, may then be used to predict minimum service life of a pressure vessel.

Using Equation (3), critical flaw size versus applied stress-level curves can be established for various materials in the tank (weld, base metal, forgings, etc.) When symbol σ_0 represents operating stress level and α represents proof pressure factor — with α always greater than unity — the critical flaw sizes corresponding to proof stress, $\alpha\sigma_0$, and operating stress, σ_0, may be read directly from the curve in Figure 4, illustrating the relationship between maximum possible flaw sizes at proof and operating stress levels.

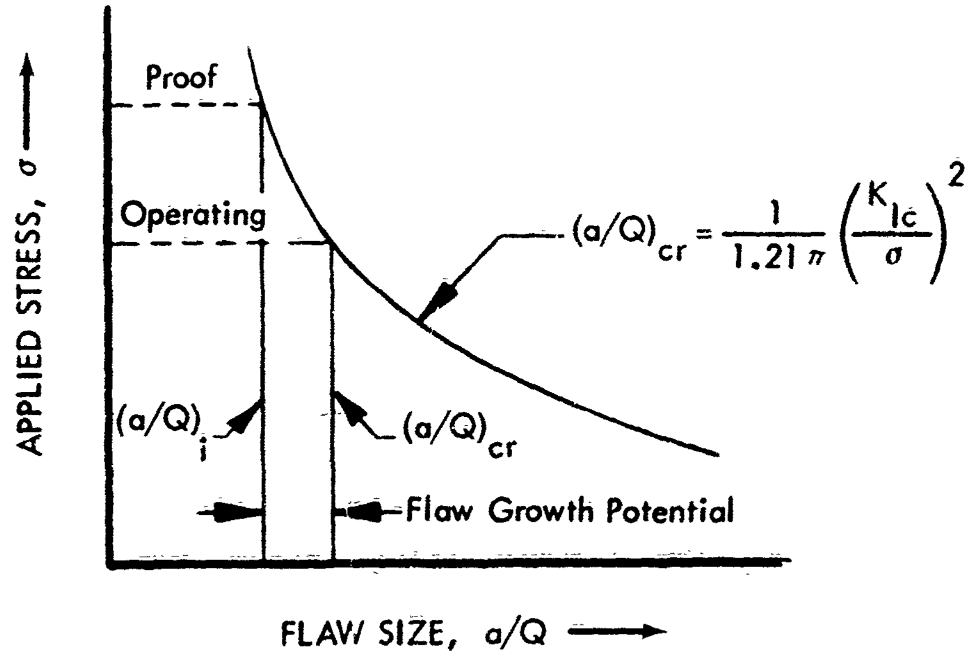

Figure 4: Flaw Growth Potential as a Function of Proof and Operating Stress Levels

From Figure 4 it may be observed that the critical flaw size $(a/Q)_{cr}$, at the proof-pressure stress level may be regarded as the largest possible initial flaw size $(a/Q)_i$ that could be retained in the pressure vessel before it is put in service. Given the ratio of the initial flaw size, $(a/Q)_i$, to the critical flaw size, $(a/Q)_{cr}$, at the operating stresses, the flaw growth potential may be conveniently expressed in terms of the proof pressure factor. Thus, from Equation (3), for a given K_{Ic} value for a material, the critical flaw size at the operating stress level (σ_0) becomes:

$$(a/Q)_{cr} = \frac{K_{Ic}^2}{1.21\pi\sigma_0^2} \quad (5)$$

Likewise, for the same K_{Ic} value, the critical flaw size at the proof stress level can be calculated by substituting proof stress $(\alpha\sigma_0)$ in place of σ in Equation (3). But since the very same flaw which was about to become critical at the proof stress level now (upon reduction of stresses from proof $(\alpha\sigma_0)$ to operating (σ_0) stress level) may be regarded as the largest possible initial flaw size which could be present in the tank as it is put in service. Therefore, it may be appropriately called the maximum possible intial flaw $(a/Q)_i$ at the operating stress level in the tank, which has been subjected to the described proof test. Thus

$$(a/Q)_i = \frac{K_{Ic}^2}{1.21\pi(\alpha\sigma_0)^2} \quad (6)$$

When Equation (5) is divided into Equation (6), the ratio of the initial to critical flaw sizes as a function of proof pressure factor is obtained.

$$\frac{(a/Q)_i}{(a/Q)_{cr}} = \frac{1}{\alpha^2} \tag{7}$$

The minimum possible flaw growth potential (i.e., inches of flaw growth remaining before failure) of the tank is then $(1-1/\alpha^2)$ multiplied by the critical flaw size at the operating stress level. It is to be noted that the finite critical flaw sizes and thus the flaw growth potential will vary throughout a tank, since the fracture toughness values will likely vary between base metal, weldments, forgings, etc. However, in terms of percent of the critical size, the flaw growth potential is a constant for a given proof factor.

SUBCRITICAL FLAW GROWTH

Although it is recognized that there are several kinds of subcritical flaw growth, the purpose of this program was to investigate only the cyclic flaw growth. For this purpose several sharply notched round-bar specimens are statically pulled to failure to determine the K_{Ic} value of the material. Additional specimens are then loaded to various percentages of the critical stress intensity and cycled to failure following a cyclic spectrum believed to be representative of the pressure vessel service loading. The initial stress intensities, K_{Ii}, are calculated using Equation (1) by substituting the initial net area stress, σ_i, in place of the net area fracture stress, σ_n. The σ_i is calculated by dividing the maximum cyclic load by the initial net area. As cycling progresses, the notch deepens in the same manner as when a flaw grows in a tank under cyclic load and, by virtue of the ever-increasing stress on the net area, the stress intensity increases from the initial value, K_{Ii}, to the critical value, K_{Ic}, at which time failure occurs. Test results are then plotted in terms of K_{Ii}/K_{Ic} versus cycles to failure on semilog paper. A schematic representation of the plot is shown in Figure 5.

Similarly, when surface-flawed specimens are subjected to cyclic loading until failure, a plot of K_{Ii}/K_{Ic} versus cycles to failure for surface-flawed specimens can also be established.

The equivalency between the two plots can be shown to exist by considering Equations (1) and (3). Both equations are used for determination of plane strain (K_{Ic}) fracture toughness. Barring excessive influences of pronounced anisotropy of the material, use of either equation should and does yield the same fracture toughness values. Therefore, it would be appropriate to take Equations (1) and (3) and equate their respective right-hand sides. Solving for $(a/Q)_{cr}$ yields the following relationship:

$$(a/Q)_{cr} = \frac{.045\, D(\sigma_n/\sigma)^2}{\left[1 - \frac{1}{2\pi D}\left(\frac{K_{Ic}}{\sigma_{Y.S.}}\right)^2\right]^6} \tag{8}$$

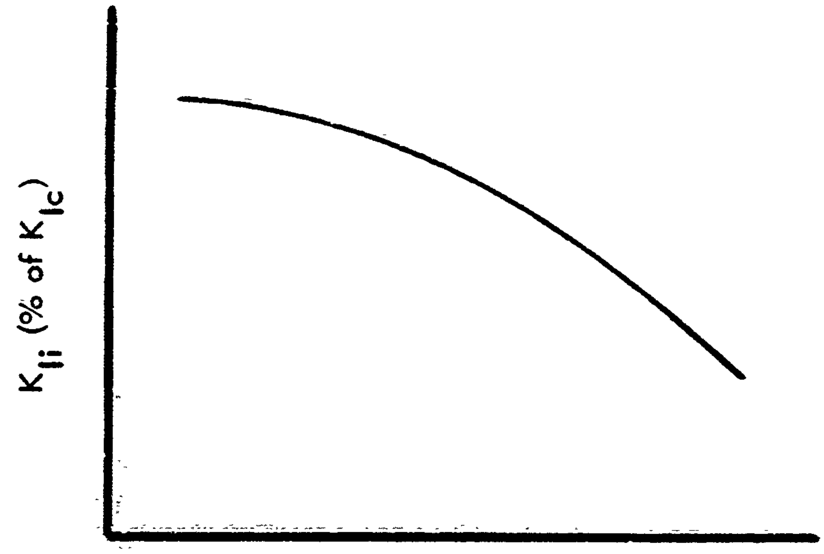

Figure 5: Cyclic Flaw Growth

When a stress lower than the net area fracture stress is applied to sharply notched round-bar specimens, a subcritical stress intensity, K_{Ii}, is generated. The expression for its value, obtained from Equation (1) by substituting σ_{ni} (initial net stress) in place of σ_n (fracture net stress), takes the following form:*

$$K_{Ii} = \frac{.233\,\sigma_{ni}\sqrt{\pi D}}{\left[1 - \frac{1}{2\pi D}\left(\frac{K_{Ic}}{\sigma_{YS}}\right)^2\right]^2} \tag{9}$$

A subcritical stress intensity (K_{Ii}) of the same magnitude can be also generated in a surface-flawed specimen subjected to a given stress level (σ) by appropriate selection of less-than-critical initial flaw size, $(a/Q)_i$. The K_{Ii} value is derived directly from Equation (3) by substituting $(a/Q)_i$ in place of $(a/Q)_{cr}$; thus, for surface-flawed specimens

$$K_{Ii} = 1.1\sqrt{\pi}\,\sigma(a/Q)_i^{1/2} \tag{10}$$

* The discrepancy introduced by using K_{Ic} rather than K_{Ii} for the yield-zone correction is considered to be negligibly small.

Because the left-hand sides of Equations (9) and (10) were set to be equal, the right-hand sides may be equated, and solving for $(a/Q)_i$ produces the following relationship for initial flaw size:

$$(a/Q)_i = \frac{.045\, D(\sigma_{ni}/\sigma)^2}{\left[1 - \frac{1}{2\pi D}\left(\frac{K_{Ic}}{\sigma_{Y.S.}}\right)^2\right]^4} \tag{11}$$

The ratio of initial flaw size $(a/Q)_i$, as expressed by Equation (11), to the critical flaw size $(a/Q)_{cr}$, as expressed by Equation (8), results in the following relationship:

$$\frac{(a/Q)_i}{(a/Q)_{cr}} = \left(\frac{\sigma_{ni}}{\sigma_n}\right)^2 \tag{12}$$

Equation (12) reveals that initial and critical flaw sizes in surface-flawed specimens are related to the initial and critical stress levels in the sharply notched round-bar specimens. The ratio of initial to critical flaw size also represents a flaw growth potential; consequently, Equation (7) shows that complete equivalency between flaw growth potential in sharply notched round-bar specimens, surface-flawed specimens, and proof-tested pressure vessels may be established; i.e.:

$$\frac{(a/Q)_i}{(a/Q)_{cr}} = \left(\frac{\sigma_{ni}}{\sigma_n}\right)^2 = \left(\frac{1}{\alpha}\right)^2 \tag{13}$$

APPLICATION OF CYCLIC FLAW GROWTH DATA

If the size, shape, and orientation of actual flaws in a pressure vessel are known, cyclic flaw growth data can be used to estimate cyclic life span of a pressure vessel. Conversely, if a requirement for certain cyclic life span of a pressure vessel is established, then the cyclic flaw growth data can be used to define the largest permissible initial flaw size. In either case, the validity of the estimates strongly depends upon the accuracy of the nondestructive inspection methods, ability to define existing stress levels, and exclusion of uncontrolled metallurgical and environmental variables. Further consideration should be also given to the manner in which a subcritical (initial) flaw grows to critical size.

As applied to pressure vessels there are three general types of subcritical flaw growth. These are discussed in detail in Reference 9 and are summarized below:

<u>Type I</u> A through-the-thickness crack grows to a critical size with stress cycles, causing failure.

<u>Type II</u> An initial internal or surface flaw grows through the thickness with stress cycles, and then to critical size, causing failure.

Type III Prior to growing through the thickness, an initial internal or surface flaw grows to critical size with stress cycles, causing failure.

For the Type I crack, onset of rapid fracture is governed by the measured fracture toughness related to the material thickness, as shown in Figure 2. As noted earlier, growth of the initial Type II crack is first governed by plane-strain toughness, regardless of material thickness, but after growth through the thickness, behavior is identical to the Type I flaw. Type III flaw growth is by far the most dangerous condition; both the initial growth and inception of instability are governed by the plane-strain (K_{Ic}) fracture toughness value. No advance warning, such as leakage, is given , and since the K_{Ic} value is considerably lower than the K_c value, the critical sizes of embedded or surface flaws can be quite small. Because of the importance of Type III, the major effort in this program was devoted to this type of subcritical flaw growth

With the Type III subcritical flaw growth in mind, consider a pressure vessel that has been proof tested at 40 percent above its operating stress level ($\alpha = 1.4$). The intersection of the 1.4 proof-pressure line with the critical flaw size curve (Figure 6, which has been plotted for a hypothetical 6Al-4V titanium tank to be operated at -320°F) gives a point on the abscissa that represents the largest possible initial flaw size that could be retained in the pressure vessel after the proof test. Obviously, the flaws retained in the pressure vessel could be smaller than the one read off the abscissa but certainly not larger; in that case, the vessel would have burst during the proof test.

The ratio of initial to critical flaw size is directly dependent upon $(1/\alpha)^2$ where α is the proof test factor (Equation 12), the successful proof test thus indicates that there are no greater initial flaws than $(1/\alpha)^2$ or 51 percent of the critical flaw size at the operating stress level. Since the initial-to-critical flaw ratio $(a/Q)_i/(a/Q)_{cr}$ is also proportional to the $(K_{Ii}/K_{Ic})^2$ ratio, the entire family of constant cycles to failure curves can be constructed as a plot of applied stress versus flaw size (a/Q) using cyclic flaw growth data from sharply notched round-bar or surface-flawed specimens. When these data are applied to the 6Al-4V titanium hypothetical tank, which has been proof-tested to 1.4 of its operating stress level, the expected minimum strength of the tank at any one time during its cyclic life can be established.

The minimum strength at proof test corresponds to point A' on Figure 6. This point gives the maximum possible initial flaw of 51 percent of critical at operating stress. The initial flaw as used from Figure 6A would grow to size B in about 100 cycles and the minimum strength at the end of 100 cycles is equal to B' on Figure 6B. During the additional 40 cycles the flaw grows to point C giving minimum strength at that point equal to C'. At the end of 150 cycles the maximum possible initial flaw will grow to critical size and cause failure.

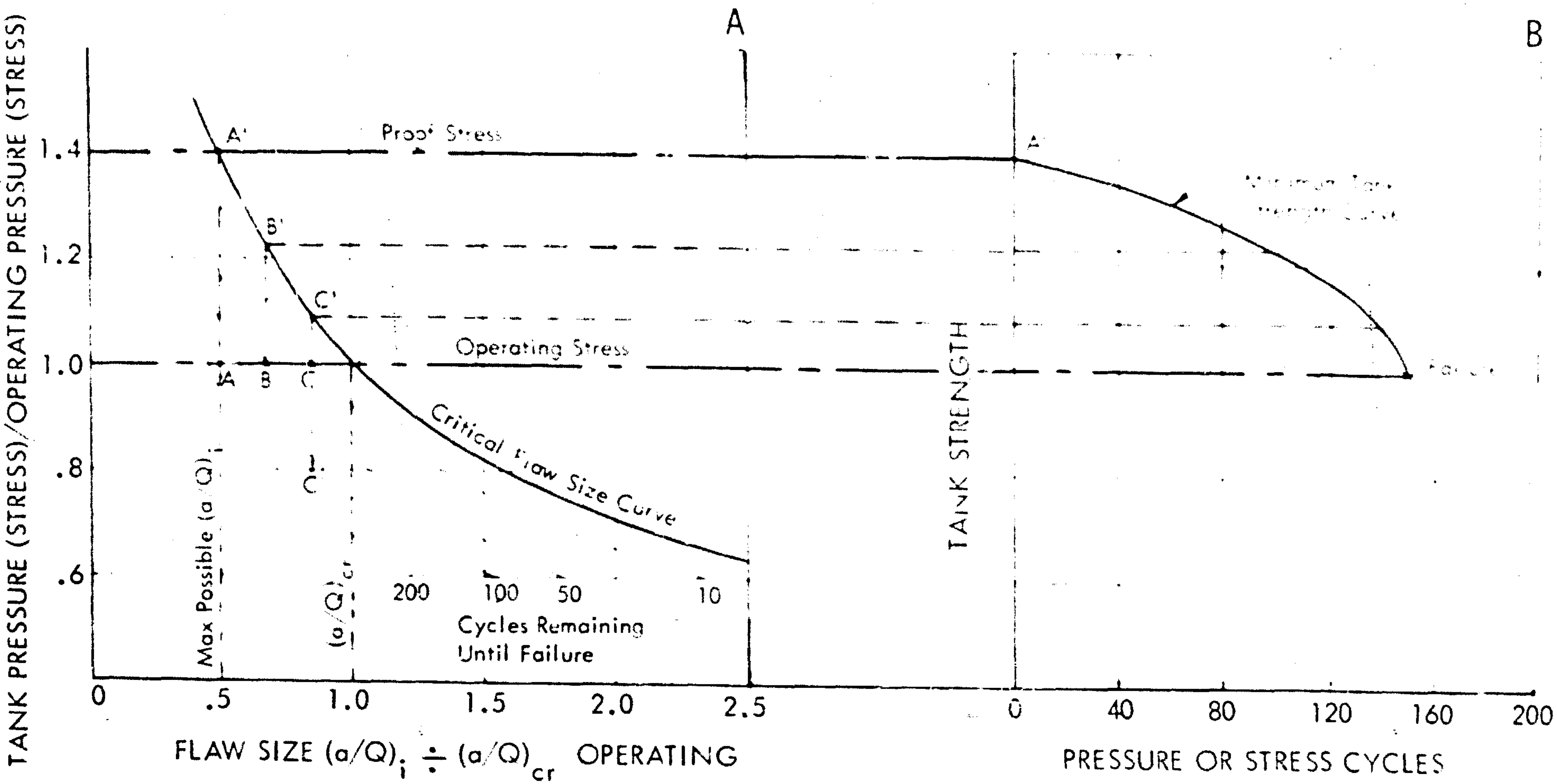

Figure 6: Sample Procedure for Estimating Minimum Cyclic Tank Life

Also, the minimum cyclic life span and the remaining strength of the tank may be estimated for different operating stress levels while using the same plot shown in Figure 6A. For example, if after the first 140 cycles the operating stress level is dropped to 80 percent of its original value (Point C" on Figure 6A) and then cycled at this stress level until failure, the tank should have the capacity to sustain at least 120 cycles until failure. The cyclic life span of the tank would, of course, be greater than predicted if the retained initial flaws after proof test were actually smaller than 51 percent of the critical size.

MATERIALS AND TEST SPECIMENS

The Ladish D6A-C steel plates (0.50 by 36 by 60 inches, Heat No. 3950937, and 0.375 by 36 by 60 inches, Heat No. 3950935) were purchased in hot-rolled, annealed, pickled, and oiled condition. Considerable variation in flatness (oil-canning of up to 0.40 inch) was noted in the 0.50-inch-thick plates. Although the deviations from flatness were within acceptable limits of AMS 2252, the plates did require straightening before fabrication of test specimens and 17-inch-diameter tanks. This has been accomplished by stress-relieving the Ladish D6A-C plates at 1225°F for 8 hours between heavy flat steel plates. The deviation from flatness in the 0.375-inch plates could be tolerated because they were to be deep-drawn and hot-spun to make 17-inch-diameter tank heads.

The 6Al-4V titanium plate (0.50 by 36 by 36 inches, Heat No. 321251) was purchased in hot-rolled, annealed, and cleaned condition per AMS 4911. The variation in flatness was also pronounced (waviness of up to 0.25 inch), and the plate had to be straightened by stress-relieving at 1300°F for 1 hour between heavy steel plates. Prior to the 1300°F stress-relieve cycle, the titanium plate was protective-coated with Turco 4367-Pretreat to prevent possible contamination during the stress-relieve.

The 18Ni(300) maraging steel plate (0.25 by 36 by 72 inches, Heat No. 3951003) was purchased in the annealed, pickled, and oiled condition. The variation in flatness, unlike Ladish D6A-C and 6Al-4V titanium plates, was not pronounced.

The weld wire for welding 17-inch-diameter test tanks was made available from existing stock. Two kinds of weld wires were evaluated prior to final selection. The first was with the very low carbon content produced by the Linde Company under code number M1-88. The other was Ladish D6A-C Armetco Weld Filler wire of slightly less-than-parent-metal carbon content. Chemical composition of the weld wires and all three materials is listed in Table 1, Appendix I.

Configuration of the smooth, round, tensile specimen used for determination of uniaxial tensile properties of Ladish D6A-C steel plate and 6Al-4V titanium plate is shown in Figure 21, Appendix II. The uniaxial tensile properties of 18 Ni(300) maraging steel were determined using the smooth, flat tensile specimen shown in Figure 22. Static fracture toughness and cyclic flaw growth characteristics of Ladish D6A-C steel and 6Al-4V titanium were obtained using sharply notched round-bar and surface-flawed flat specimens shown in Figures 23 and 24, respectively. The surface-flawed specimens of the same basic configuration shown in Figure 24 (except for uniform gage thickness) were used to generate cyclic flaw growth data and to determine plane-strain static fracture toughness values for 18Ni(300) maraging steel. In addition, the through-the-thickness cracked specimen shown in Figure 25 was also used to determine plane stress fracture toughness and develop some cyclic crack growth data for through-the-thickness cracks.

Weld test panels used for evaluation of weld filler wires are shown in Figure 26. The edge preparation was adopted directly from the 3/8-inch-thick, 36-inch-diameter production pressure vessels. This to some extent facilitated development of the weld settings. Tensile weld-joint specimens and weld-bend test specimens used for evaluation of weld test panels are shown in Figures 27 and 28, respectively. Initial development of the weld settings for welding 17-inch-diameter test tanks was done using short cylindrical sections (shells) shown in Figure 29. Configuration of the 17-inch-diameter tanks used for the Phase III testing is shown in Figure 30.

EXPERIMENTAL PROCEDURE

All Ladish D6A-C specimens were machined with the longitudinal axis of the specimens oriented parallel with the plate-rolling direction. The specimens were rough-machined into blanks, and given the following heat treatment:

Austenitized at 1550 ±25° F for 1 hour

Salt-quenched to 400° F

Held in salt at 400° F for 10 to 15 minutes

Rinsed in boiling water

Air-cooled below 150° F

Double-tempered at specified temperature for 2 hours each within 15 minutes after air-cooling

The normalizing cycle has been omitted in the heat treatment given to the Ladish D6A-C test specimens because during an earlier attempt to heat-treat Ladish D6A-C weld-test panels the material cracked severely (laminated) during air-cooling after normalizing at 1650°F for 1 hour. Omission of the normalizing cycle was also considered desirable to minimize distortion in the 17-inch diameter test pressure vessels fabricated from the same material.

The Phase I Ladish D6A-C test specimens, scheduled to provide the preliminary information on the response to heat treatment and to determine the mechanical properties and static fracture toughness of Ladish D6A-C steel as a function of tempering temperature, consisted of five groups. Each group contained four specimen blanks to make two smooth tensile and two sharply notched round bar specimens. The five groups, after being austenitized and quenched in one batch, were then separated and double-tempered at 400, 500, 600, 800, and 1000 ±10 °F, respectively.

After tempering, all tensile specimens and all sharply notched round bar specimens were finish-machined (Figures 21 and 23). Low-stress, uniaxial, tension-tension cyclic loading was applied to each specimen at room temperature until adequate notch acuity (fatigue extension) was developed in each specimen. For this purpose, an optical microscope was trained at the root of the notch to detect crack initiation and growth. To reduce the possibility of eccentric notch extension, each specimen was frequently rotated around its longitudinal axis.

The Phase II Ladish D6A-C specimens consisted of 8 surface-flawed and 30 sharply notched round bar specimen blanks. The eight surface-flawed specimen blanks were austenitized, salt-quenched, and double-tempered at 600 ±10° F in a single batch. The 30 round bar specimen blanks were similarly heat treated but in a different batch.

The sharply notched round bar specimens were finish-machined and subjected to low stress cyclic loading to extend the initial notch in the manner identical to that for the Phase I specimens. The surface-flawed specimen blanks were finish-machined (Figure 24). The initial surface flaw was introduced using the Electrical Discharge Machine (EDM). The terminating root radius of the EDM flaw was less than 0.003 inch. Subsequently, each surface-flawed specimen was cycled at low tension-tension stress to initiate adequate fatigue extension of the EDM flaw. The optical microscope was used to ascertain adequacy of the fatigue extension. Testing of the specimens usually followed immediately after fatigue extension, using the same tensile machine.

Development of the weld settings for the six Ladish D6A-C 17-inch diameter test tanks used in Phase III testing consisted of two parts. First, a suitable weld filler wire was selected on the basis of tensile and slow bend test results obtained from weld test panels shown in Figure 26. Then, a series of short cylindrical sections 17 inches in diameter and about 6 inches long (shown in Figure 29) were rolled, machined, and welded to simulate weld-joint configuration and welding conditions of the 17-inch-diameter tanks.

A total of three weld panels and six cylindrical shells were fabricated. The first panel was welded with MI-88 Linde weld filler wire. In the second panel the MI-88 wire was used only to make the root pass; the remaining filling passes were completed with Ladish D6A-C Armetco weld wire. The third panel was welded entirely with Ladish D6A-C Armetco weld filler wire. Preheat and postheat cycles of 600 and 900°F, respectively, were used for welding each weld-test panel, cylindrical shells, and later the 17-inch-diameter tanks. The cylindrical shells and the 17-inch diameter tanks were welded entirely with MI-88 weld filler wire because it offered an adequate combination of strength and ductility (see Table 8 and Figure 38), having the capacity of going into general yielding together with the base metal.

Selection of the preheat and postheat cycles was conditioned by prior experience in welding high-strength steels and by suggested procedures in the technical literature. Particular attention was devoted to keeping the parts at the preheat temperature of 600 ±50° F during the entire welding operation, subsequent cooling down to 350 ±50° F to affect more complete transformation to martensite, and postheat to 900 ±50° F for 15 to 30 minutes to temper the transformed martensite immediately upon completion of welding. The 17-inch-diameter tank sub assemblies were also stress-relieved at 1200 ±25° F for 2 hours each after the postheat cycle. Quality of the weld joints in test panels, cylindrical sections, and later in the 17-inch-diameter tank was inspected by X ray and by the Magnaflux in accordance with MIL-I-6865 and MIL-I-6868, respectively. All welds in weld test panels and cylindrical sections were found to be acceptable. One close-out weld in Tank VI was rejected because of inadequate penetration and excessive incidence of porosity. The tank, however, was later accepted to be used "as is" because the size and orientation of porous cavities, together with the lack of penetration, were estimated to be considerably smaller than the largest permissible initial flaw for that section of the weld. Later the tank was burst-tested with the fracture originating at the surface flaw in the base metal.

All 17-inch-diameter tanks were heat-treated according to the same schedule used for Ladish D6A-C specimens: i.e., austenitized at 1550°F for 1 hour, salt-quenched to 400°F, rinsed in boiling water, then double-tempered at 600 ±10 F for 2 hours each. A special heat-treat harness fixture was built to submerge the tanks during the salt-quench and rinsing operations.

Upon completion of the heat treatment, the tanks were proof-pressure tested at 3750 psi maximum pressure, which was above the expected burst pressures once the surface flaws were introduced into the tanks. The main purpose of the proof-pressure test was to ensure personnel safety during initial fatigue extension of the surface flaws in the tanks. During examination of the surface flaws, the tanks were kept pressurized at 600 psi to facilitate detection of the initial fatigue extensions.

The 6Al-4V titanium specimens scheduled for evaluation of mechanical properties and static fracture toughness as part of the Phase I testing consisted of three smooth tensile specimens (Figure 21) and three sharply notched round bar fracture-toughness specimens (Figure 23). The Phase II tests were conducted using seven additional sharply notched round bar specimens (Figure 23) and four surface-flawed specimens per Figure 24.

Because the 6Al-4V titanium plate was received and was to be tested in the annealed condition during the Phase I and II work, all specimens were finish-machined without heat treatment except for the previously mentioned stress-relieve to reduce waviness in the plate. Sharply notched round bar specimens were subjected to the low-stress cyclic loading to initiate adequate fatigue extension in the manner similar to Ladish D6A-C specimens. In addition to the major (largest) initial surface flaw located in the midportion of the gage area, the 6Al-4V surface-flawed specimens contained two additional (smaller) surface flaws, one on each side along the longitudinal axis of the specimen. All three surface flaws were 3 inches apart. The fatigue extension of the major surface flaw was done by low-stress, uniaxial, tension-tension cyclic loading. Although each of the smaller flaws also experienced the same cyclic loading, the stress intensity (due to their smaller size) was not high enough to start fatigue extension. Therefore, when initial fatigue extension was detected in the major flaw, the specimen was removed from the tension-tension fatigue machine and mounted as a cantilever beam in a specially designed bending fixture. The specimen was then subjected to cylic bending in a manner that generated highest tensile stresses in the region of the first minor flaw. After in-plane rotation of the test specimen, cyclic bending was repeated to generate highest stresses in the region of the second minor flaw until fatigue extension in both minor flaws was detected.

The 18Ni(300) maraging steel specimens (eight per Figure 22 and four per Figure 25) were scheduled to provide preliminary information as part of the

Phase I work on the response to heat treatment and to determine the mechanical properties and static fracture toughness as a function of aging temperature. The specimens were divided into four groups of two smooth tensile and one center-cracked specimen: then the four groups were aged at 800, 850, 900, and 950 ±10°F, respectively, for 3 hours each.

The Phase II group of 18Ni(300) specimens consisted of two center-cracked specimens (Figure 25) and four surface-flawed specimens of uniform thickness (Figure 24). All specimens in this group were finish-machined after aging at 900 ±10°F for 3 hours in a single batch. The center-cracked as well as surface-flawed specimens were then subjected to low-stress cyclic loading to generate adequate fatigue extension at the tips of center cracks and surface flaws. Only one surface flaw per specimen was used.

TEST CONDITIONS

All Ladish D6A-C test specimens were tested at room temperatures. Strain rates of 0.005 and 0.02 inch per inch per minute were used on all smooth tensile specimens. Statically tested sharply notched round bar and surface-flawed specimens were pulled to failure at a loading rate needed to produce a complete failure within 1 to 3 minutes.

With the exception of the initial fatigue extension of EDM flaws and machined notches (initial fatigue extension was done at the rate of 1800 cycles per minute) the cyclic flaw growth data was generated using a trapezoidal loading profile at a cyclic frequency of one cycle per minute. The trapezoidal loading profile was formed by breaking each cyclic period into four equal parts. The first part was spent in going from zero load to maximum load; the second in holding the specimen at a maximum load; the third in unloading; and the fourth part at zero load. Similar loading profile was also applied to 17-inch-diameter test tanks. The trapezoidal load programmer is shown in Figure 31.

All testing of Ladish D6A-C specimens was intended to take place in the ambient atmosphere. However, during the generation of cyclic flaw growth data using sharply notched round bar specimens large scatter of data points led to a suspicion that variations in the relative humidity in the air may be creating an undesirable effect upon flaw growth characteristics. As a check, several specimens were deliberately moisturized by wrapping the notched area with a moist cloth, one end of which was submerged in water. The notch area itself never came in direct contact with the water. The cyclic life span of such specimens was reduced by a factor of more than ten.

Concurrently, some specimens were also tested with the notch or surface flaw area covered with a dehydrating powder. The cyclic life span of these specimens appeared to be slightly higher than that of specimens tested in air. Although variation of relative humidity failed to show any trends, it was decided to dessicate the surface-flawed area in the remaining specimens and in the 17-inch diameter Ladish D6A-C test tanks.

In addition to checking the effect of moisture, several specimens were also tested to check the possible effect of the omission of normalizing cycle upon flaw growth characteristics. Some of these specimens were heat-treated using a normalizing cycle at 1650 ±25° F for 1 hour in addition to austenitizing at 1550 ±25° F, followed by a double temper at 600 ±10° F for 2 hours each. The behavior of these specimens, when subjected to cyclic loading, was not significantly different from that of non-normalized specimens. Consequently, a change of heat-treatment procedure appeared to be unnecessary.

Testing of the 17-inch-diameter tanks consisted of two tanks being burst-tested, while the remaining four tanks were pressure-cycled to failure using a trapezoidal loading profile. The pressurizing medium was hydraulic oil, per MIL 5606. The trapezoidal loading was generated by the same programmer used for cyclic testing of specimens. After initial low-stress fatigue extension, each surface flaw was covered with a pad containing dehydrating powder.

Fatigue extension of surface flaws was first attempted by using the hydraulic system of a Losenhauser Universal Tensile Machine, capable of generating a sinusoidal loading profile at a frequency of about 300 cycles per minute. However, the volumetric oil displacement of the machine operating at this frequency could not produce a large enough amplitude to effect fatigue extension. After two attempts and the loss of one tank because of inadequate fatigue extension, the hydraulic bench used for burst and trapezoidal testing was instrumented to deliver cyclic pressurization with acceptable amplitude and at about 25 to 30 cycles per minute. The changeover from sinusoidal to trapezoidal loading profile in the bench was relatively simple, and each tank was tested shortly after the initial fatigue extension of the surface flaw. Figure 32 shows a schematic representation of the tank test setup.

The applied hoop stress levels in the tanks were calculated using pressure readings and tank dimensions of diameter and thickness. In addition, the first two tanks tested were instrumented with Type A-5 SR-4 strain gages, located 120 degrees apart on a 3-inch radius, with the surface flaw in the center. Because one of the tanks suffered detectable distortion during the heat treatment good correspondence between strain gage readings and calculated hoop stresses on the first two tanks was considered sufficient to give full credence to the calculated stress values. The remaining tanks were tested without strain gages.

All 6Al-4V titanium specimens were tested at -320° F in liquid nitrogen, which was admitted into a removable cryostat. Figure 33 schematically shows the test fixture with the cryostat mounted around a sharply notched round bar specimen. A similar arrangement was also used for testing surface-flawed specimens under static and cyclic loading conditions. As in Ladish D6A-C specimens, the initial low-stress fatigue extension of notches and surface flaws was done at room temperature, with the sinusoidal loading administered at a frequency of 1800 cycles per minute. Cyclic flaw growth data were determined using a trapezoidal loading profile with frequency of 1 cycle per minute and using the load programmer shown in Figure 31.

The 18Ni(300) maraging steel specimens were tested in the manner similar to Ladish D6A-C specimens except that no additional tests on the effect of moisture were conducted. Furthermore, since there were also through-the-thickness cracked specimens, a 35-mm camera was used to record slow growth during static testing for determination of a total crack length at the inception of crack instability.

The camera setup consisted of one camera being trained at the test specimen while the other was trained at the load dial. Both cameras were actuated by the same electrical control. Satisfactory resolution of the film was achieved using a symmetrically oriented light source with a parabolic reflector and a polarizing screen. The polarizing screen was placed over the camera lens and adjusted by rotation until the contrast between the initial crack and the specimen surface reached its maximum. Figure 34 shows the 35-mm camera setup similar to the one used in this program.

In addition, each of the through-the-thickness cracked specimens and one surface-flawed specimen were instrumented for detection of pop-in (plane strain instability) during loading. The instrumentation consisted of two electrical resistance SR-4 strain gages applied to each specimen near both tips of the crack. The distance from the tip was about 0.10 inch. The strain gages were connected to the X-Y plotters, which recorded and plotted load in pounds versus strain near the crack tip. At the instant of pop-in, whenever one occurred, a sudden increase in strain registered on the X-Y plot. Taking the load at the instant of pop-in and the initial crack length, the plane strain (K_{Ic}) values could be calculated.

EXPERIMENTAL RESULTS

LADISH D6A-C STEEL

Because of the severe cracking of Ladish D6A-C plate during earlier attempts to heat-treat the steel, several small samples were given various heat-treatment cycles and then were submitted to metallurgical examination. Additional samples were sent to the chemical laboratory for spectrographic and gas analyses.

The results of the spectrographic analysis (shown in Table 1) checked well with the vendor's analysis. The gas analysis revealed only a trace of hydrogen (less than 4 ppm), oxygen 7 ppm, and nitrogen 90 ppm. Metallurgical examination of several sectioned samples failed to reveal any traces of pre-existent microfissures or cracks, which could have caused severe cracking and lamination during quenching.

Omission of the normalizing cycle and substitution of 400°F salt quench in place of quench to room temperature were found to produce uniform microstructure with only a small trace of bainite. The as-quenched hardness of such samples was 57-58 Rc as compared to 58-59 Rc for samples that were normalized and oil-quenched to room temperature. Both samples appeared to be completely homogenized upon subsequent double tempering, and, when examined under a 500-power optical microscope, could not be distinguished from each other.

Tensile properties and static fracture toughness of Ladish D6A-C steel plate are listed in Tables 2 and 3, respectively, and are plotted in Figure 7 as a function of tempering temperature. Table 2 shows a 0.02-percent offset yield strength as well as the conventional 0.2-percent offset yield strength. Cyclic flaw growth data, together with additional static fracture toughness data, are listed in Table 4 for sharply notched round bar specimens and in Table 5 for surface-flawed specimens.

The initial and critical flaw sizes were determined from fractographs taken from each fractured specimen and 17-inch-diameter test tanks. A wide-field optical microscope with a graduated eyepiece was used to facilitate detection of the exact outlines of initial and critical flaw boundaries. Because progression of surface flaws and round notches was not always consistent with the assumed shapes (semiellipse for surface flaw and cylindrical notch for round bar specimen), the flaw and notch dimensions were calculated with the aid of a polar planimeter.

In the case of sharply notched round bar specimens, the initial and critical notch areas, as measured from the fractograph using a polar planimeter, were used to calculate the equivalent net diameter that would be needed to generate exactly the same area for a truly circular shape. The initial and critical surface flaw areas were used to calculate equivalent flaw lengths (major axis of the

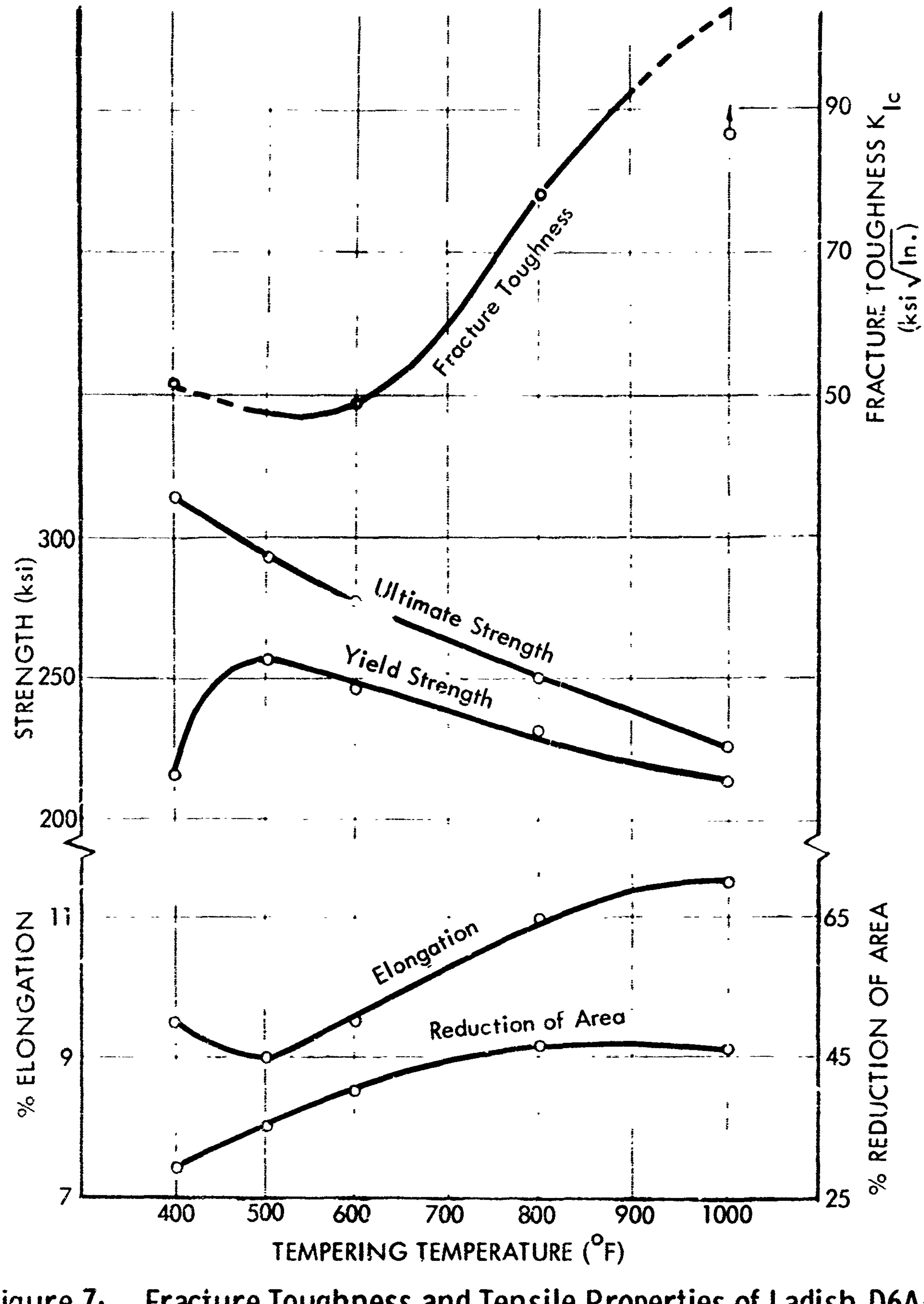

Figure 7: Fracture Toughness and Tensile Properties of Ladish D6A-C Steel Plate

ellipse) assuming that the flaw is truly semielliptical with the actual flaw depth being the minor semiaxes. The calculated values were then used in fracture toughness equations for calculation of initial and critical fracture toughness values.

Sample fractographs of sharply notched round bar specimens tested under static and cyclic loading conditions are shown in Figures 35 and 36, respectively. Sample fractographs of surface-flawed specimens are shown in Figure 37 in Appendix IV. Figures 35 and 36 illustrate some of the flaw growth irregularities encountered during cyclic testing of Ladish D6A-C sharply notched round bar specimens.

Possible relationships between flaw growth direction and grain orientation in sharply notched round bar specimens were checked by etching portions of the sharply notched round bar specimens and measuring the included angle between the two. The results are listed in Table 26 and plotted in Figure 8 in the form of a histogram.

Test results on the effect of moisture and variation of heat treatment cycles (normalized versus non-normalized specimens) are listed in Table 7. Tensile and bend test data of Ladish D6A-C weld test panels are listed in Table 8. General appearance of the tensile and bend weld joint test specimens after testing is shown in Figure 38.

The results of burst and cyclic testing of the 17-inch-diameter Ladish D6A-C test pressure vessels are listed in Table 9. General appearance of the six fractured tanks is shown in Figures 39 and 40. A composite view of the tank shell samples containing fracture origin is shown in Figure 41. For comparison, Figure 42 shows general appearance of the sample of the surface flawed specimens after testing.

Fractographs of the six Ladish D6A-C 17-inch-diameter test tanks are shown in Figures 43 and 44.

The combined cyclic flaw growth data obtained from sharply notched round bar specimens, surface-flawed specimens, and the 17-inch-diameter pressure vessels are plotted in Figure 9 in terms of initial stress intensity as a percent of critical K_{Ic} value versus cycles to failure on semilog paper.

Because of the large scatter of test data points for sharply notched round bar specimens, the K_{Ii}/K_{Ic} ratio was taken on the basis of individual K_{Ic} value for each respective specimen. In this manner, the scatter was suppressed and the relationship between sharply notched round bar, surface-flawed specimen, and 17-inch-diameter tanks became more apparent. The effect of flaw depth-to-material thickness ratio is shown in Figure 10.

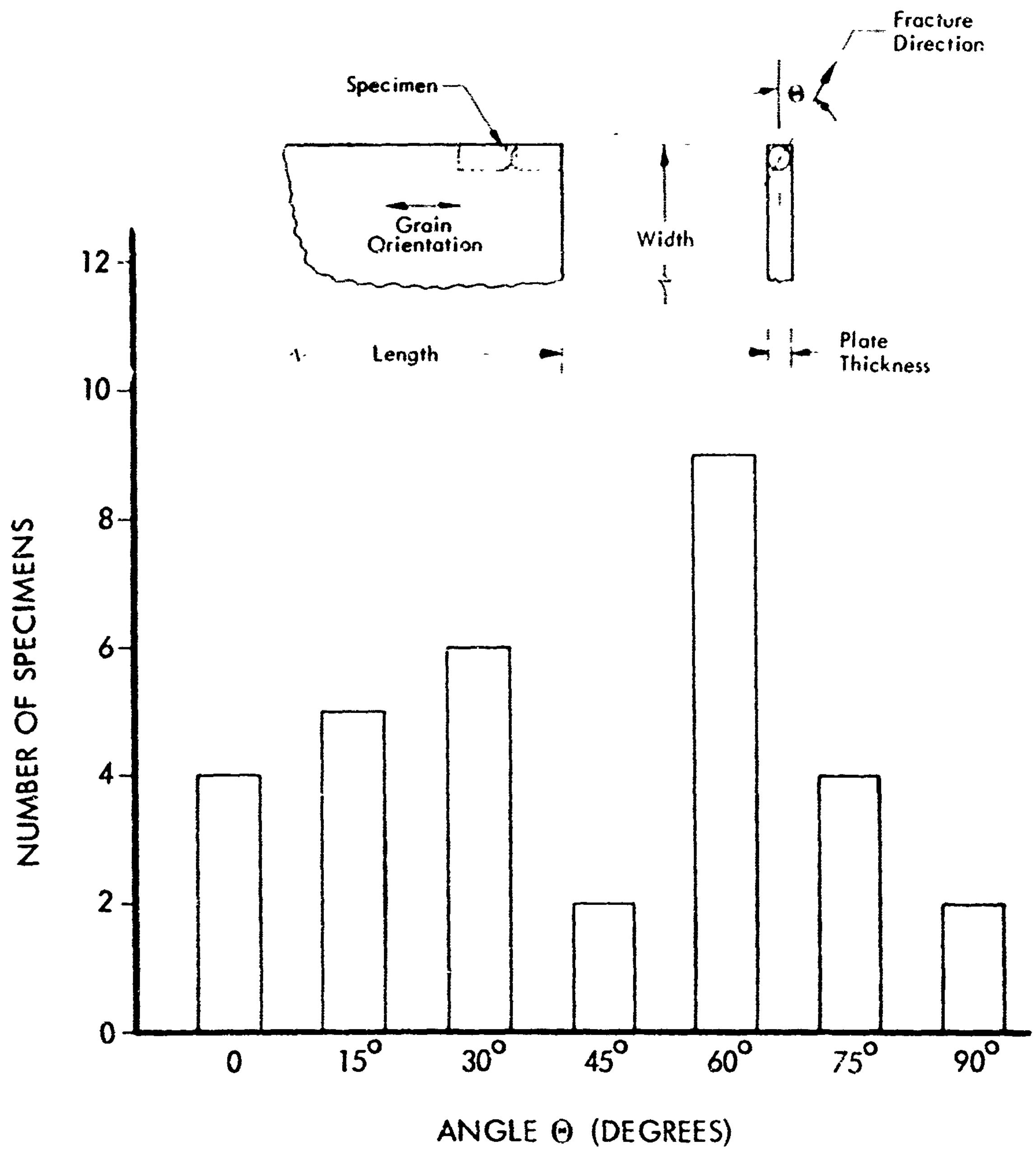

Figure 8: Frequency Distribution of Acute Angle Between Flaw Growth Direction and Grain Orientation in Ladish D6A-C

SHARPLY NOTCHED ROUND BAR SPECIMENS

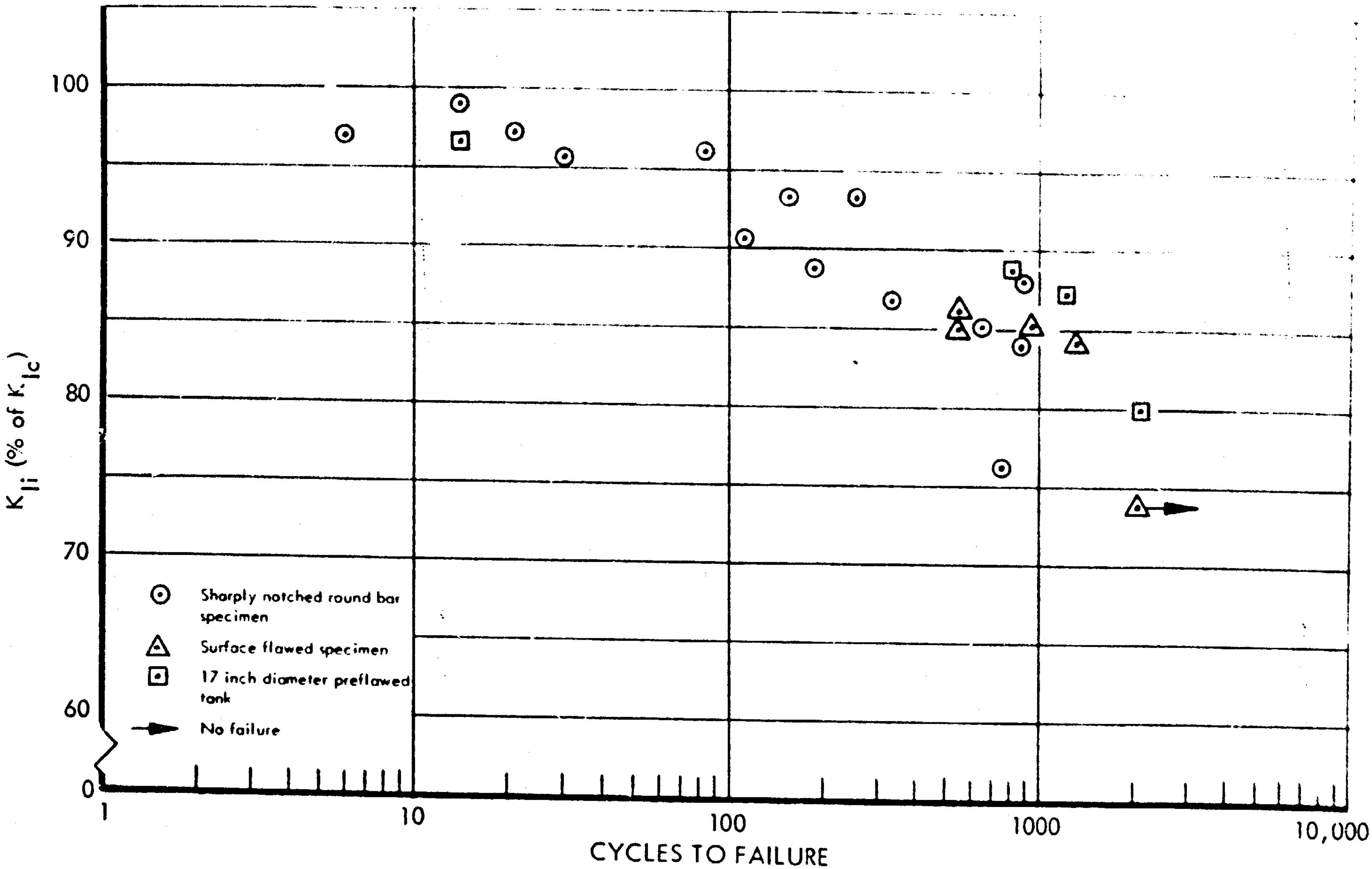

Figure 9: Combined Cyclic Flaw Growth Data of Ladish D6A-C Steel Plate
TESTED AT ROOM TEMPERATURE

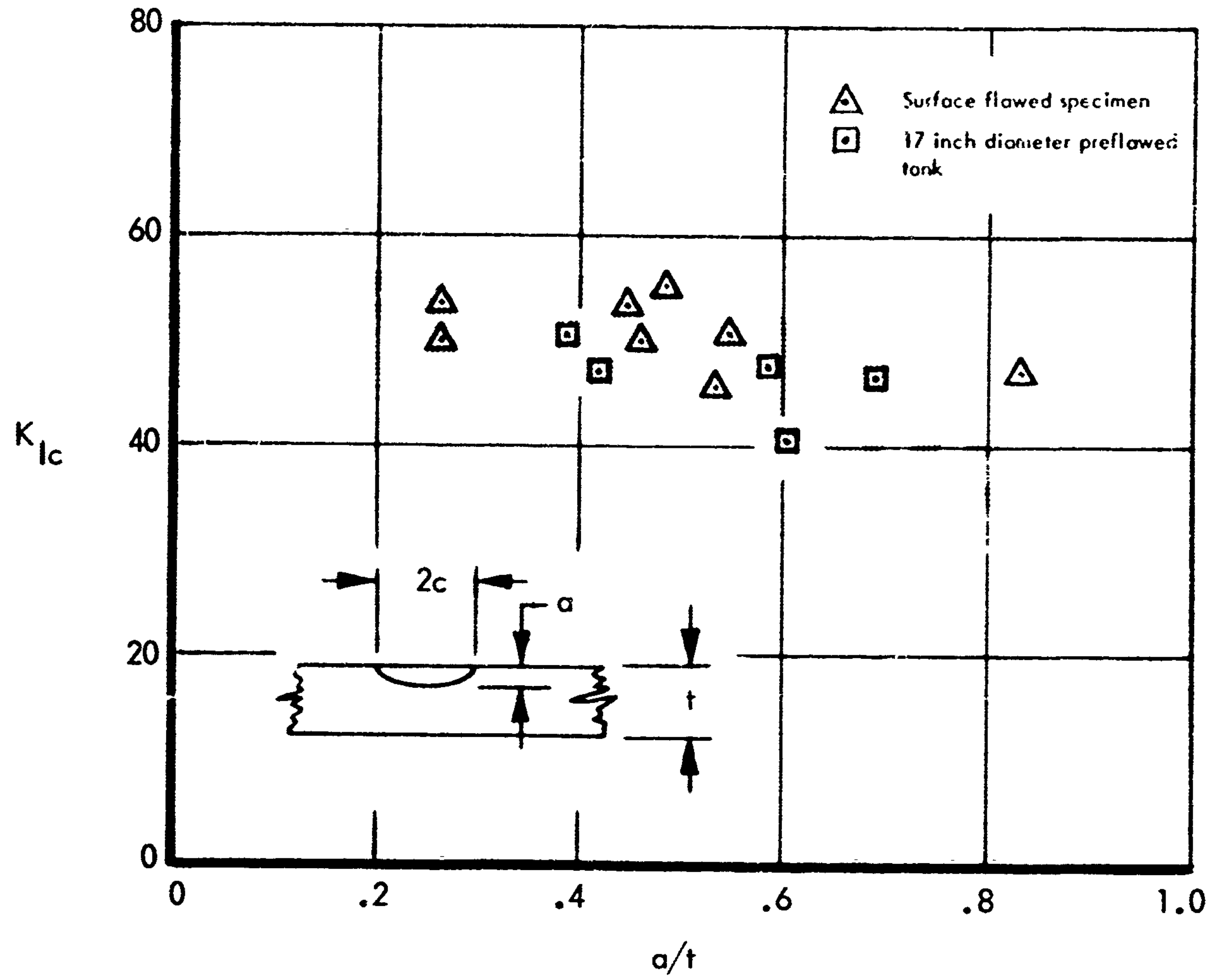

Figure 10: Effect of Depth-to-Thickness Ratio on Measured Fracture Toughness of Ladish D6A-C Steel

TESTED AT ROOM TEMPERATURE

The use of data points resulting from testing eccentric, sharply notched round-bar specimens and the use of actual rather than average K_{Ic} values for Ladish D6A-C to obtain K_{Ii} K_{Ic} versus cycle curves may be justified as follows. An eccentric, sharply notched round bar specimen, because of its eccentricity, will have an initial stress intensity that is higher than that of a concentric specimen. Similarly, after an eccentric specimen sustains a certain number of cycles, the eccentricity will become larger, and the actual stress intensity will again be higher than that of an identical but concentric specimen. There is no simple way to establish the extent of stress augmentation because of eccentricity, but this problem is circumvented by taking the ratio of calculated initial K_{Ii} and the actual measured K_{Ic} values. Of course, the method hinges on the assumption that the percentage of stress augmentation for initial and critical flaw sizes because of eccentricity is comparable.

6Al-4V TITANIUM

Tensile properties of the 6Al-4V titanium tested at -320°F in the environmen of liquid nitrogen are listed in Table 10. Static fracture toughness and cyclic flaw growth data obtained using sharply notched round bar specimens were calculated using planimeter technique and are listed in Table 11. Figure 1[illegible] shows a plot of static fracture toughness for annealed 6Al-4V titanium as a function of test temperature. Test data at other than -320°F temperature was obtained in connection with other Boeing programs. Sample fractographs of sharply notched 6Al-4V titanium specimens tested at -320°F are shown in Figure 45.

Cyclic flaw growth data obtained using surface flawed 6Al-4V titanium specimens are listed in Table 12. Figure 46 in Appendix IV shows sample fractographs of 6Al-4V titanium surface flawed specimen tested at -320°F. General appearance of the fractured 6Al-4V titanium surface flawed specimens is shown in Figure 47.

Combined cyclic flaw growth data obtained from sharply notched round bar and surface flawed specimens are plotted in Figure 12. The effect of depth to thickness ratio in the surface flawed 6Al-4V titanium specimens is shown in Figure 13.

18Ni(300) MARAGING STEEL

The tensile properties and static fracture toughness of 18Ni(300) maraging steel tested at room temperature are listed in Tables 13 and 14, and are plotted in Figure 14 as a function of aging temperature. Figure 15 shows a composite plot of crack growth during static testing of through-the-thickness cracked specimens as well as load versus strain as recorded by the X-Y plotters. These were the specimens instrumented for detection of "pop-in" plane strain crack instability during testing to determine the K_{Ic} value in addition to the plane stress (K_c) calculated from fracture stress and photographic crack growth records.

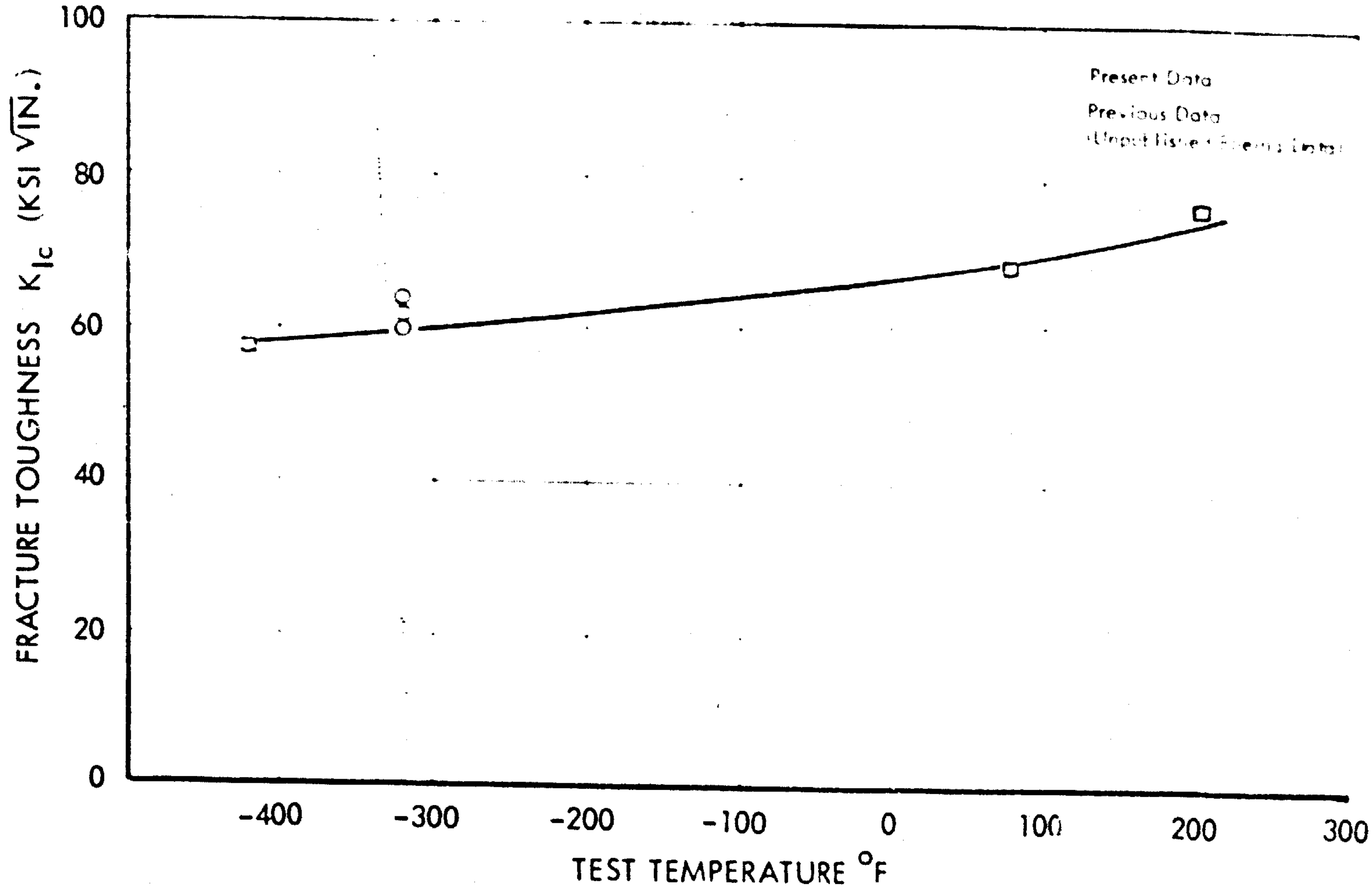

Figure 11: Fracture Toughness of Annealed 6Al-4V Titanium Plate at Various Test Temperatures

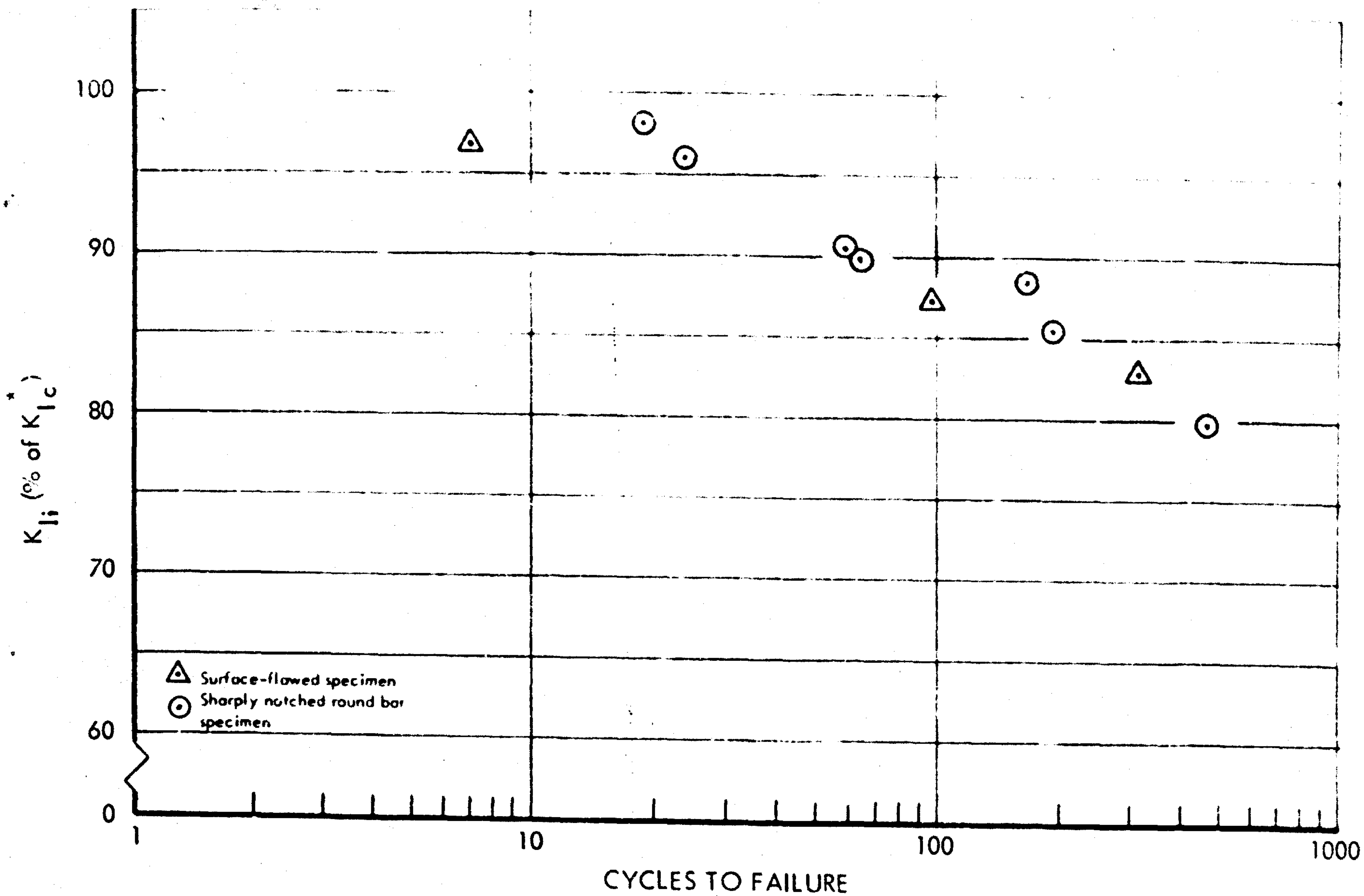

Figure 12: Cyclic Flaw Growth Data of 6Al-4V Titanium Plate
TESTED AT -320°F

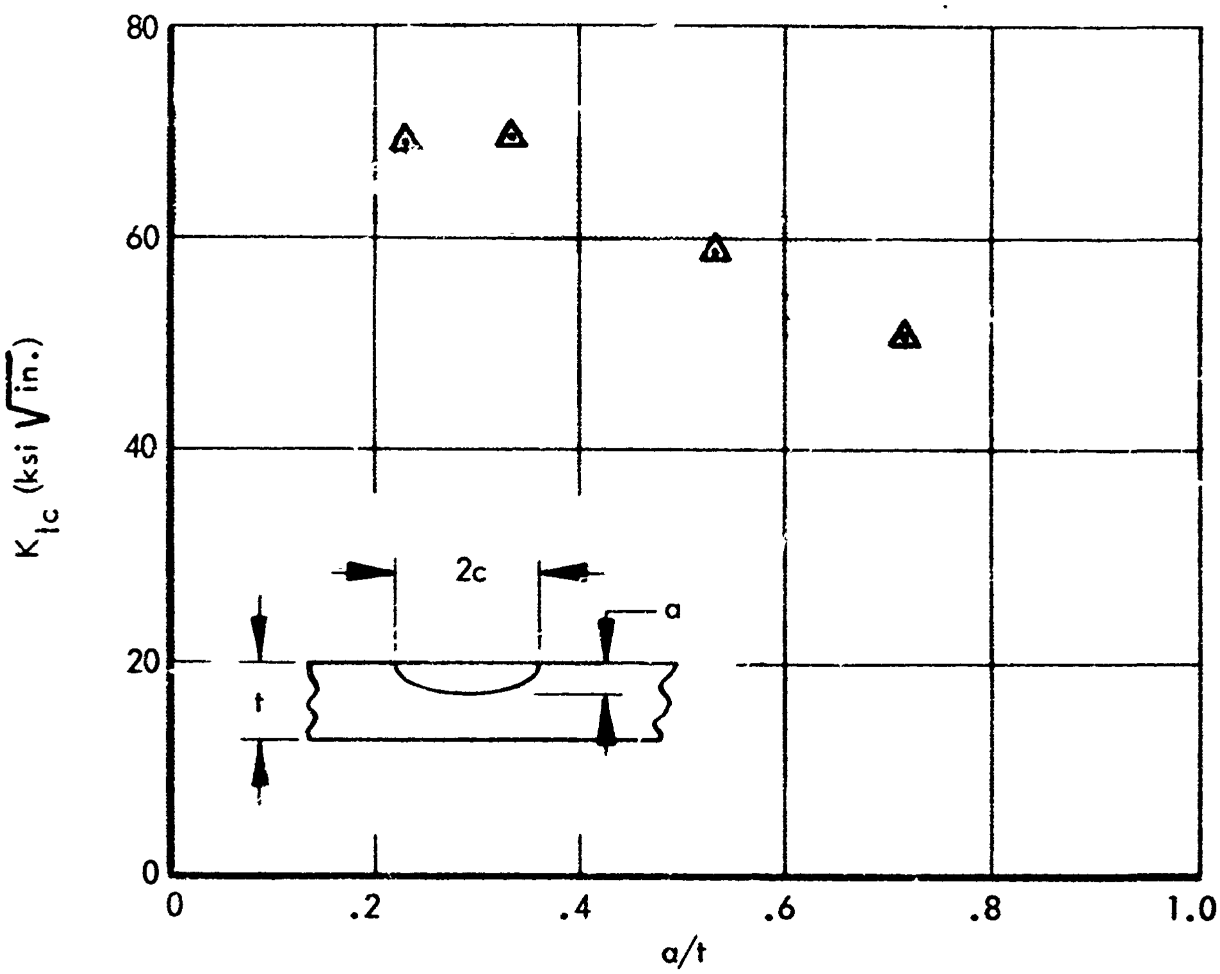

Figure 13: Effect of Depth-to-Thickness Ratio on Measured Fracture Toughness of 6Al-4V Titanium Plate Tested at -320^0 F

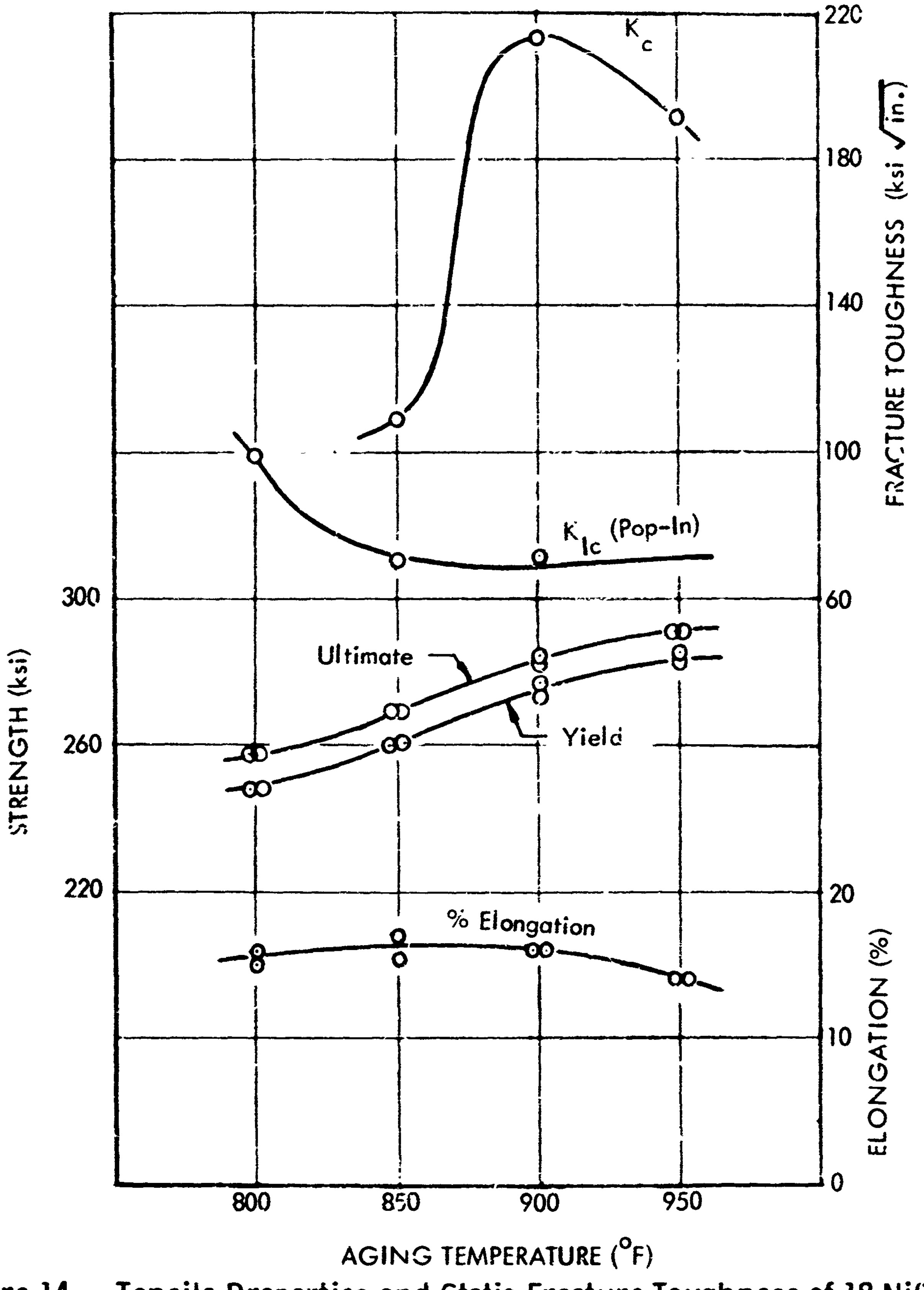

Figure 14: Tensile Properties and Static Fracture Toughness of 18 Ni(300) Maraging Steel

TESTED AT ROOM TEMPERATURE

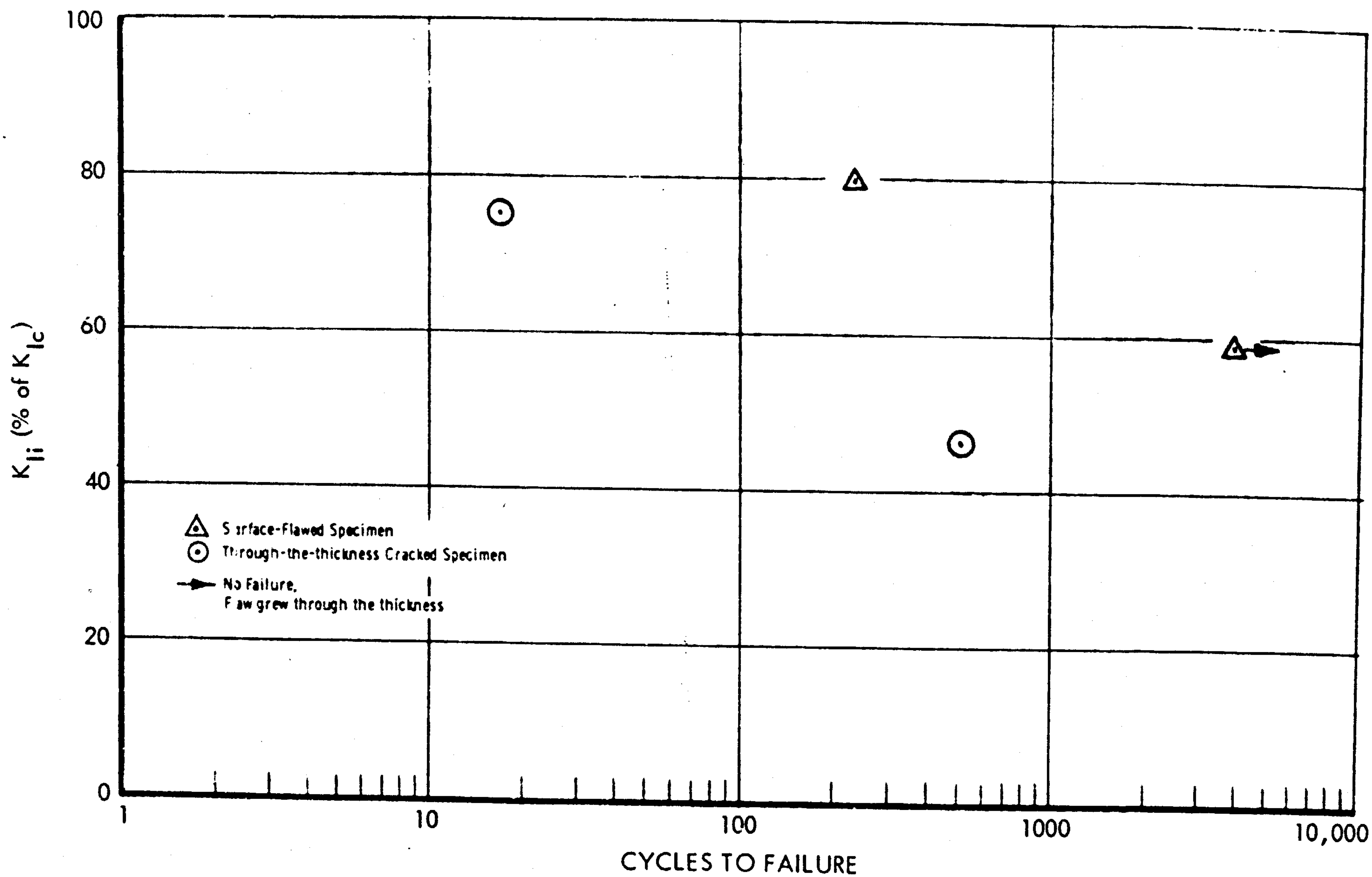

Figure 15: Cyclic Flaw Growth Data of 18 Ni(300) Maraging Steel
TESTED AT ROOM TEMPERATURE

In the absence of distinct pop, a point of tangency is sometimes taken to give the K_{Ic} value. Although the point of tangency in the present case (specimen MC-1 in Figure 16) is clearly defined, it was not used in the calculation because of the tentative nature of the point-of-tangency approach for determining K_{Ic} values. General appearance of fractured through-the-thickness cracked specimens is shown in Figure 48.

Static fracture toughness and cyclic flaw growth data of 18Ni(300) maraging steel tested at room temperature using surface-flawed specimens were calculated using previously described planimeter technique and are listed in Table 15. The MS-1 specimen failed in grip area at 247.0 ksi during static test. The MS-2 specimen failed in grip during cyclic test at the end of 1396 cycles. Both specimens were remachined to 3.5-inch widths and tested. The MS-1 specimen was pulled to failure at a fracture stress of 257.4 ksi. Cyclic testing at 112.6 ksi of the MS-2 specimen was resumed and continued for an additional 2514 cycles until the flaw grew through the thickness. The specimen was then pulled to a failure at a fracture stress of 118.2 ksi. Specimens MC-5 and MC-8 were machined to 3.5-inch widths, then tested. Figures 49 and 50 show sample fractographs of statically and cyclically tested 18Ni(300) surface flawed specimens, respectively.

Cyclic flaw growth data of 18Ni(300) maraging steel tested at room temperature using through-the-thickness centrally cracked specimens were determined from periodic crack growth measurements and post-fracture examination of test specimens, and are listed in Table 16. Figure 51 shows a general appearance of 18Ni(300) surface-flawed and centrally cracked specimens after cyclic testing.

A combined plot of cyclic flaw growth data for surface-flawed and through-the-thickness cracked 18Ni(300) specimens are shown in Figure 15. The data are plotted in terms of initial to critical stress intensities versus cycles to failure. For surface-flawed specimens the K_{Ii}/K_{Ic} ratio is used while for the through-the-thickness cracked specimen K_i/K_c is plotted The initial plane stress intensity (K_i) was calculated using Equation 4 by substituting initial half crack length (a_i) in place of critical crack length (a) and using applied stress in place of fracture stress σ.

The effect of flaw depth-to-thickness ratio upon measured K_{Ic} values for 18Ni(300) maraging steel is shown in Figure 17. Specimen MS-2 is also shown on the plot even though no actual K_{Ic} value was obtained. Due to limited amount of surface flawed specimens and complete absence of sharply notched round bar specimens no attempt was made to construct a σ versus a Q plot with different cycles-to-failure curves as was done for Ladish D6A-C steel.

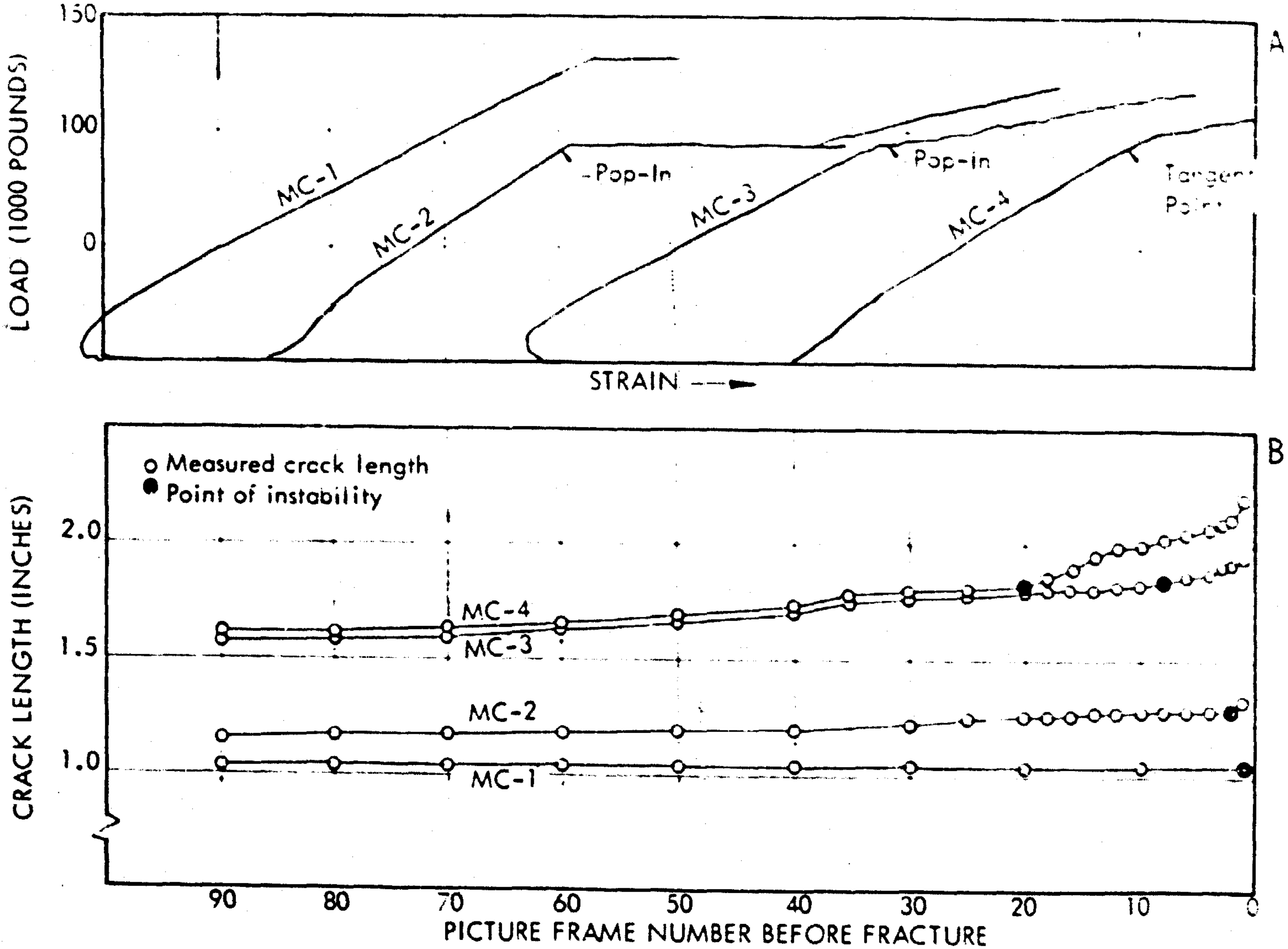

Figure 16: Summary of Pop-In and Crack Growth Data for 18 Ni(300) Maraging Steel

TESTED AT ROOM TEMPERATURE

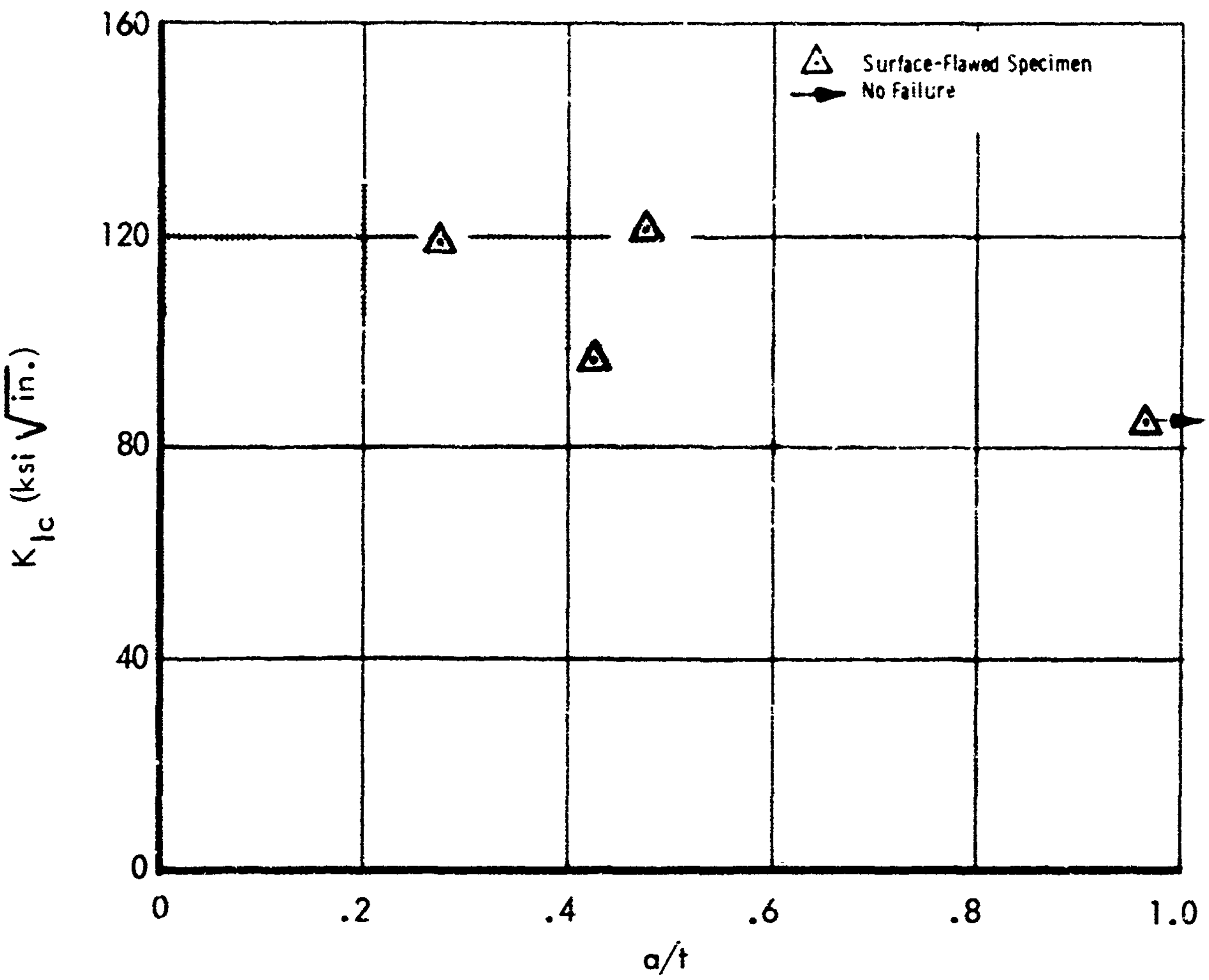

Figure 17: Effect of Flaw Depth-to-Thickness Ratio on Measured Fracture Toughness of 18 Ni (300) Maraging Steel
TESTED AT ROOM TEMPERATURE

DISCUSSION

Several aspects of the present program warrant some additional consideration. The following paragraphs illustrate a possible way of using flaw growth data for design purposes and point out the differences in behavior among various materials in spite of the apparent similarity in loading conditions. The prevalent tendency of fatigue flaws to assume balanced (usually circular) shape may be explained on a purely analytical basis by considering the variation of stress intensity, K, along the periphery of a flaw. The effect of natural barriers such as a pronounced anisotropy or tendency to delaminate will be pointed out as a possible explanation of apparent inconsistencies. Finally, the effect of flaw depth-to-thickness ratio will be discussed, together with some observed effects of environmental variables.

Returning now to the cyclic flaw growth data shown in Figure 9 and considering the lowest boundary of the scatter band, together with the minimum static facture toughness of K_{Ic} - 46.0 ksi $\sqrt{in.}$ as obtained from Figure 10, a minimum cyclic life span family of curves for different operating stress levels and various initial flaw sizes may be constructed. Such a family of curves is plotted to scale and is shown in Figure 18.

The process of constructing such curves consists of selecting a series of points for a different number of cycles to failure on the abscissa of Figure 9; then taking corresponding readings on the ordinate in terms of percent of minimum K_{Ic}, which was found to be equal to 46.0 ksi $\sqrt{in.}$ Using Equation (3), a plot of applied stress (σ) versus initial flaw size (a/Q) for each selected number of cycles to failure is then obtained.

It should be noted that since such a plot is based upon minimum values in terms of cyclic flaw growth and static fracture-toughness data, the predictions deduced from the plot will also represent a minimum cyclic life span of a component containing a known initial flaw size and subjected to a given cyclic loading.

Usefulness of the method for design purposes would be further enhanced by establishing required confidence limits for the original data shown in Figures 9 and 10, as well as by providing refined NDT inspection capabilities for definition of initial flaw shapes and sizes in the structural components.

Not to be overlooked of course are various metallurgical and environmental variables whose effect may significantly alter either flaw-growth characteristics or the actual fracture toughness of the material to the extent of making the comparison very difficult.

Of no less significance are the inherent differences in behavior of various materials. While being exposed to similar loading and under seemingly constant

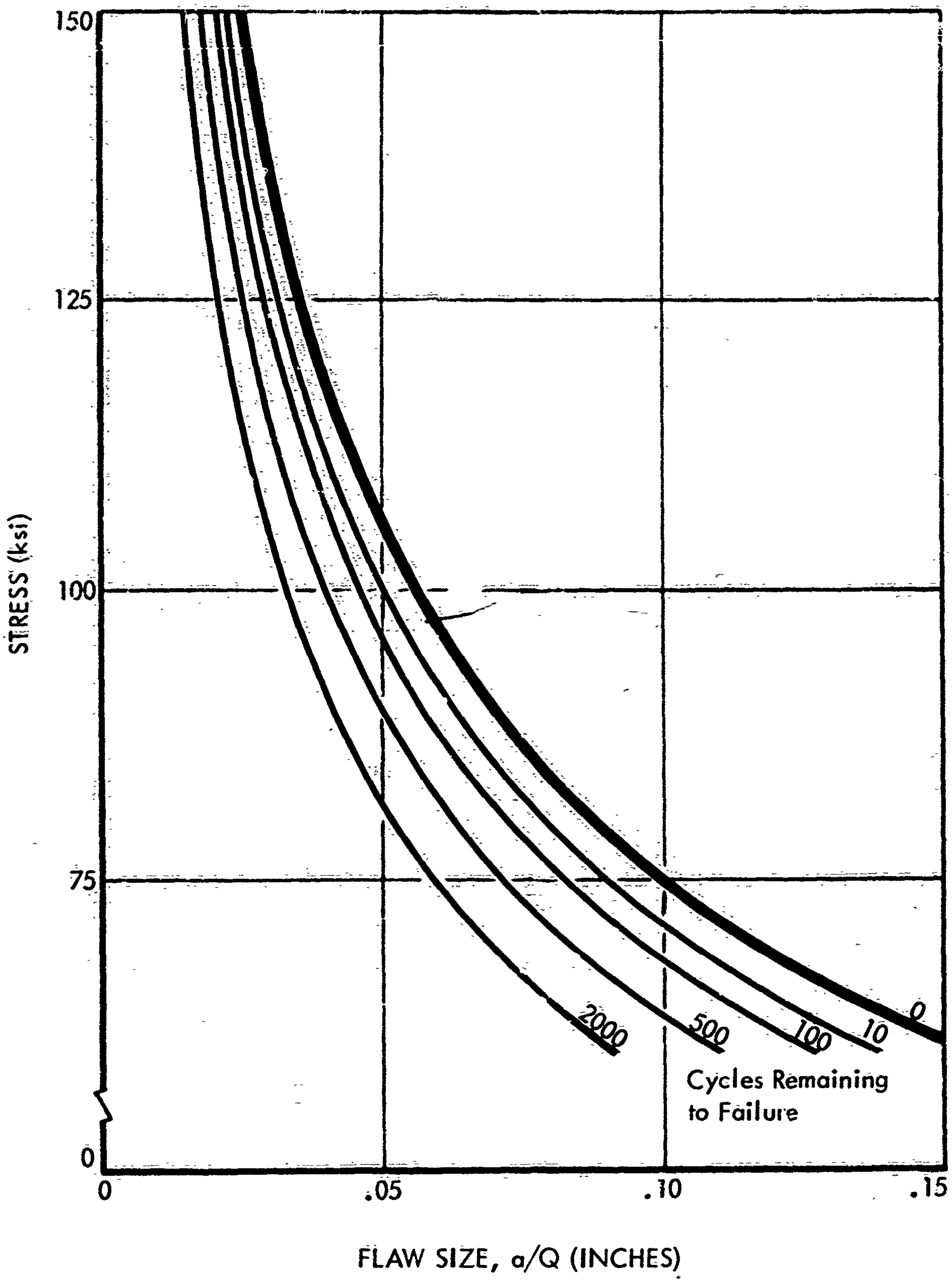

Figure 18: Minimum Cyclic Life Span Prediction Curves for Ladish D6A-C Steel

environmental conditions, significant differences in behavior were noted. The K-N plots (cyclic flaw growth data) shown in Figures 9, 12, and 16 are compared in Figure 19 with the previously obtained cyclic flaw growth data for other materials. The K-N curves plotted for various materials represent average values as obtained from the experimental scatter band. Since only a limited number of test specimens were used to generate the data, the relative values are not firmly established. Nevertheless, such comparison suggests significant variance in the behavior of different materials. Some degree of variance may also be expected as a result of variations in heat treatment or other process variables.

Now the attention will be directed to the prevalent tendency of relatively shallow surface (or embedded) flaws to grow faster in a certain direction until some balanced shape is assumed and then continue to propagate while maintaining the relative shape. Of course, some strongly pronounced directionality in material properties and possible variations in load distributions may have a decided effect on the final shape of the flaw. But before this facet of the problem is taken into account, consider Figure 20, showing the variation of stress intensity, K, along the flaw periphery (Reference 5) for different flaw depth-to-length ratios. The flaw shapes are all elliptical and are subjected to a uniaxial stress. Actual stress levels are irrelevant because the plots are made in terms of K/K_{max} ratios as a function of polar angle ϕ.

This plot is of interest for several reasons. For one thing, the plot shows that the stress intensity, K, is always maximum at $\phi = 0$ or at the deepest point of the flaw. It also shows that at the extremities of the flaw (the end points of the major axis, 2c) the stress intensity, K, is lowest. Finally, it shows that the transition from K_{max} to K_{min} is reducible to a functional form and depends upon the flaw depth-to-length ratio.

Consider now a relatively shallow surface flaw, such as that shown in Figure 46 for Specimen TS-3. Since the differences in stress intensity, K, at the exposed corners of the surface flaw and at its deepest point are large, the flaw, under cyclic loading, would be expected to propagate in depth, with very little growth along the surface. This will continue until the depth-to-length ratio increases, giving a higher K value at the corners (note the increase of K at the corners between flaws, with a/2c ratios of 0.10, 0.20, and 0.30 in Figure 20). At this point the flaw growth will be somewhat equalized along the entire periphery although the tendency to grow faster in depth continues to prevail until a completely circular shape and an even stress distribution along the flaw periphery are achieved.

The preceding discussion, while being simplified by ignoring higher restraints at the more advanced (deeper) flaw regions and the arresting tendencies of stress relaxation at the exposed corners of the flaw, serves to emphasize that certain tendencies for preferential flaw growth are inherent by virtue of differences in flaw shapes. This, however, is by no means the only phenomenon associated with changing flaw shapes.

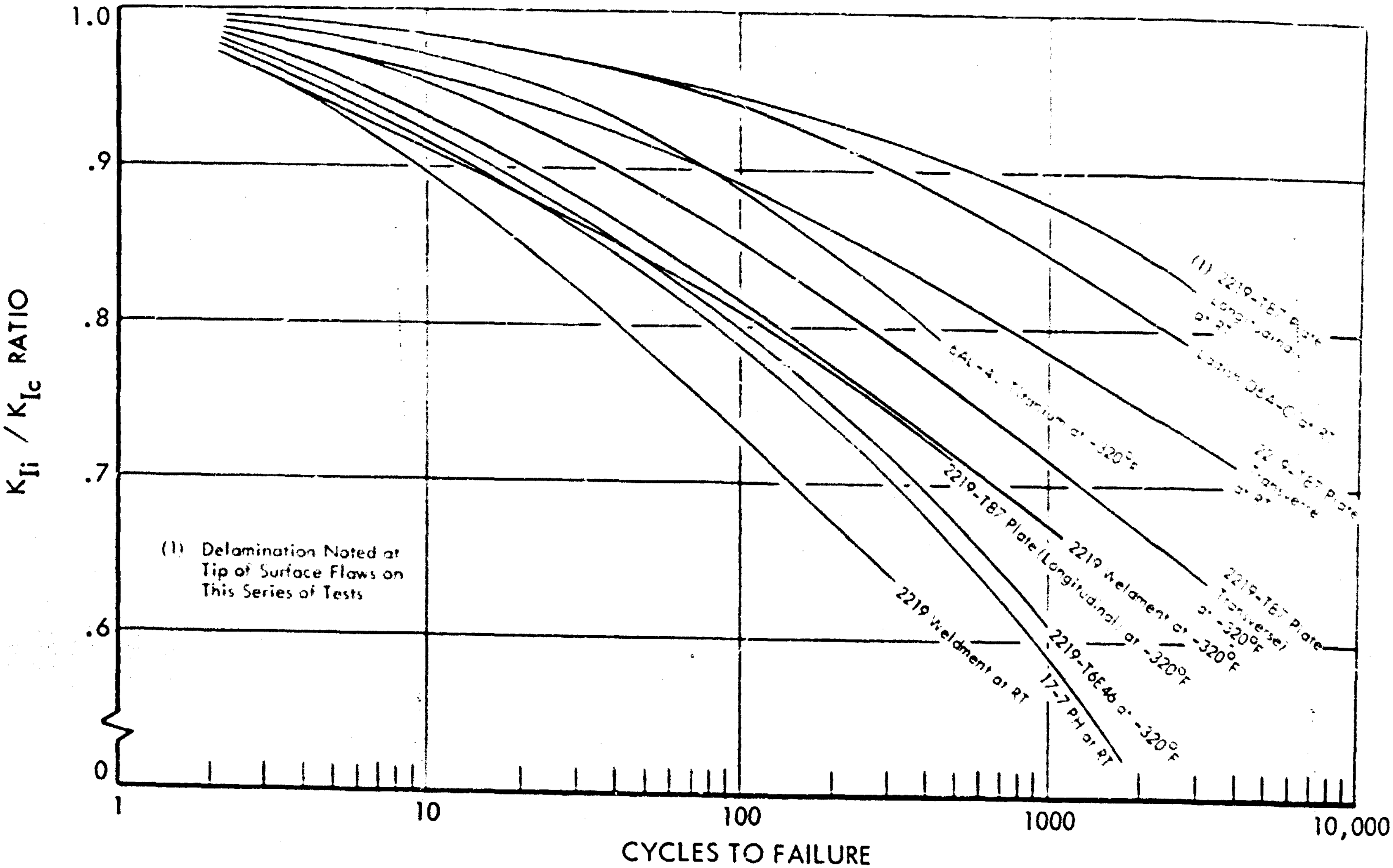

Figure 19: Comparison of Cyclic Flaw Growth Data Obtained Using Various Materials Subjected to Different Test Conditions

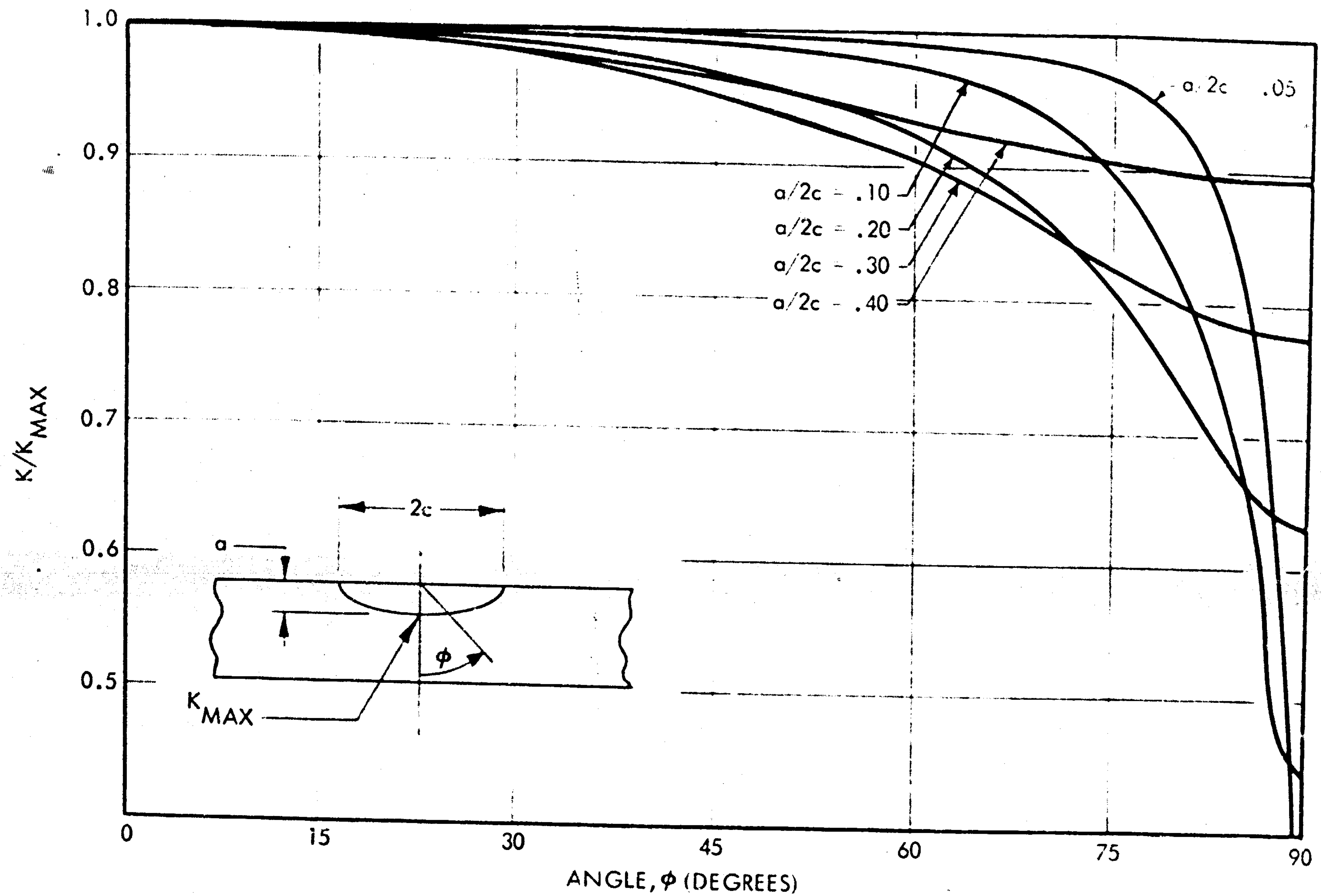

Figure 20: Variation of Stress Intensity Along Flaw Periphery

Attention is once more directed to the relatively shallow surface flaw. As the flaw begins to assume a more balanced shape (a larger a/2c ratio), the flaw shape parameter, Q, changes, bringing a corresponding change in the K_{max} value at the deepest point in addition to changes associated with the increasing a/2c value.

Summarizing, a shallow flaw grows faster in depth because of the large differences between K_{max} and K_{min}, as seen in Figure 20. The increase in the flaw shape parameter, Q, reduces the increase rate of K_{max}, while the increase rate of K_{min} continues to rise. Finally, the K_{max} begins to increase by virtue of increasing flaw size value, a/Q, until an equilibrium between the three influences is reached. Applying this consideration to a material with pronounced anisotropy, still another factor must be added.

For example, the 6Al-4V titanium plate, when tested using sharply notched round bar specimens yielded an average K_{Ic} value of 54.5 ksi $\sqrt{in.}$ (this is the average of all 6Al-4V titanium round bar specimens), while surface-flawed specimens gave a considerably higher value (K_{Ic} = 69.4 ksi $\sqrt{in.}$). Fractographic examination of sharply notched round bar specimens revealed that each of these specimens failed, with the fracture traversing the notch diameter along the grain direction (ϕ= 0 in Figure 8). The surface-flawed specimens because of the geometry, were imposing conditions that forced propagation of the flaw into (ϕ = 90) and across the grain layers, which met with greater resistance, as indicated by higher K_{Ic} values for surface-flawed specimens.

Ladish D6A-C plate, on the other hand, did not appear to have grain orientation problems of any consequence. Figure 8 suggests almost complete randomness in flaw propagation tendencies in sharply notched round bar specimens resulting in a fairly close correlation between sharply notched round bar and surface-flawed specimens.

The 18Ni(300) maraging steel plate once again appeared to have noticeable anisotropy, as seen by the differences in K_{Ic} values obtained from pop-in in through-the-thickness cracked specimens (K_{Ic} = 70.9 ksi $\sqrt{in.}$) and K_{Ic} of about 120.0 ksi $\sqrt{in.}$ obtained from the surface-flawed specimens. But in addition, as seen from Figure 50, some specimens (see Specimen MC-8) also delaminated in some regions ahead of the flaw front, thus providing natural barriers in the profile of the flaw growth and resulting in higher fracture toughness.

The built-in anisotropy of the material creates still another problem as a shallow surface flaw grows deeper into the material, creating conditions under which an edgewise propagation is facilitated, which then affects not only the flawgrowth characteristics but also the final fracture toughness value.

The effect of depth-to-thickness ratio of surface flaws is shown in Figures 10, 13, and 17 for Ladish D6A-C steel, 6Al-4V titanium, and 18Ni(300) maraging steel respectively. The decrease of measured fracture toughness as the flaw exceeds approximately one half of the material thickness is suspected to be caused by stress augmentation resulting from the restriction created as the space between the flaw front and the opposite surface becomes smaller. However, as seen in Figures 10 and 17, the trend appears to be reversing itself as a flaw approaches the opposite surface, apparently because of the associated stress relaxation caused by yielding in this local region just before the flaw grows all the way through the thickness. Both of these phenonema are under study now, and present descriptions of deep flaw growth mechanics would need additional substantiation.

An interesting observation may be made by comparing Ladish D6A-C Specimen LS-6 in Table 5 and 18Ni(300) maraging steel Specimen MS-2 in Table 15. Both specimens were subjected to trapezoidal cyclic loadings at room temperature, both specimens contained the same flaw size, and the maximum cyclic stress in both specimens was selected to be at the same percentage of their respective yield strengths. However, because of the lower fracture toughness of Ladish D6A-C as compared to 18Ni(300), the surface flaw in the Ladish D6A-C specimen became critical as it reached the 0.114-inch depth ($a/Q = 0.068$) at the end of 558 cycles, while in the 18Ni(300), the flaw grew all the way through the thickness without failure. While this observation is quite obvious and not at all surprising, if considered from the fracture mechanics point of view, it is rather odd, if viewed in the light of the respective yield strengths of the two materials as a criterion of comparison.

Another of the 18Ni(300) maraging steel surface-flawed specimens (MC-5 in Table 15) was instrumented to check experimentally the so-called "second line defense" contention advocated by Irwin (Reference 7). Briefly, it was suggested that while a surface flaw reaches its instability under plane strain (K_{Ic}) conditions, there is a built-in chance of arresting this rapidly running flaw as it propagates through the thickness. The stress relaxation occurring at that instant and the increasing influence of the K_c (plane stress) fracture toughness, which is considerably higher than the K_{Ic} value governing the initiation of instability, may be sufficient to arrest the running flaw, thus providing a second line of defense against catastrophic fracture.

The surface flaw in Specimen MC-5, Table 15, upon reaching the 173.0 ksi stress level, became unstable, popped through the thickness, and was arrested long enough for the observer to see (a faulty switch prevented it from being filmed) and remained arrested until the stress level was raised to 177.8 ksi, at which level the specimen fractured.

The effect of moisture and variations in heat treatment falls into the general category of environmental and metallurgical variables and was not intended to be looked into in this program. Additional testing was done to safeguard against introduction of new variables, not to investigate them. Nevertheless, the pronounced effect of moisture cannot escape th attention as well as the fact exceeds approximately one half of the material thickness is suspected to be caused by stress augmentation resulting from the restriction created as the space between the flaw front and the opposite surface becomes smaller. However, as seen in Figures 10 and 17, the trend appears to be reversing itself as a flaw approaches the opposite surface, apparently because of the associated stress relaxation caused by yielding in this local region just before the flaw grows all the way through the thickness. Both of these phenonema are under study now, and present descriptions of deep flaw growth mechanics would need additional substantiation.

An interesting observation may be made by comparing Ladish D6A-C Specimen LS-6 in Table 5 and 18Ni(300) maraging steel Specimen MS-2 in Table 15. Both specimens were subjected to trapezoidal cyclic loadings at room temperature, both specimens contained the same flaw size, and the maximum cyclic stress in both specimens was selected to be at the same percentage of their respective yield strengths. However, because of the lower fracture toughness of Ladish D6A-C as compared to 18Ni(300), the surface flaw in the Ladish D6A-C specimen became critical as it reached the 0.114-inch depth ($a/Q = 0.068$) at the end of 558 cycles, while in the 18Ni(300), the flaw grew all the way through the thickness without failure. While this observation is quite obvious and not at all surprising, if considered from the fracture mechanics point of view, it is rather odd, if viewed in the light of the respective yield strengths of the two materials as a criterion of comparison.

Another of the 18Ni(300) maraging steel surface-flawed specimens (MC-5 in Table 15) was instrumented to check experimentally the so-called "second line defense" contention advocated by Irwin (Reference 7). Briefly, it was suggested that while a surface flaw reaches its instability under plane strain (K_{Ic}) conditions, there is a built-in chance of arresting this rapidly running flaw as it propagates through the thickness. The stress relaxation occurring at that instant and the increasing influence of the K_c (plane stress) fracture toughness, which is considerably higher than the K_{Ic} value governing the initiation of instability, may be sufficient to arrest the running flaw, thus providing a second line of defense against catastrophic fracture.

The surface flaw in Specimen MC-5, Table 15, upon reaching the 173.0 ksi stress level, became unstable, popped through the thickness, and was arrested long enough for the observer to see (a faulty switch prevented it from being filmed) and remained arrested until the stress level was raised to 177.8 ksi, at which level the specimen fractured.

The effect of moisture and variations in heat treatment falls into the general category of environmental and metallurgical variables and was not intended to be looked into in this program. Additional testing was done to safeguard against introduction of new variables, not to investigate them. Nevertheless, the pronounced effect of moisture cannot escape the attention as well as the fact

CONCLUSIONS

While fully appreciating the limitations imposed by variations in material properties and environmental and loading variables, together with the significant influences of flaw shape and size relationship with respect to material thickness, the following conclusions have been reached:

1) Experimental correlation between cyclic flaw growth data generated using uniaxially loaded, sharply notched round bar and surface-flawed fracture toughness specimens has been obtained for Ladish D6A-C steel and 6Al-4V titanium alloy.

2) Applicability of basic principles of fracture mechanics to prediction of the minimum cyclic life span of biaxially loaded pressure vessels on the basis of uniaxial cyclic flaw growth data has been verified by testing six 17-inch-diameter, surface-flawed Ladish D6A-C test tanks.

3) Utilization of proof-pressure testing or a refined NDT inspection procedure for defining maximum-possible initial flaw size in conjunction with the static fracture toughness and cyclic flaw growth data for design purposes appears to be possible.

4) Limited experimental support of the "leak-before-break" and "second line defense" criteria was provided by cyclic and static testing of surface flawed 18Ni(300) maraging steel specimens.

REFERENCES

1. An Approach to the Prediction of Pressure Vessel Minimum Fatigue Life Based Upon Applied Fracture Mechanics, Boeing Document D2-22437

2. Williams. M. L., "On the Stress Distribution at the Base of a Stationary Crack," Journal of Applied Mechanics, March 1957

3. Irwin, G. R., "Analysis of Stresses and Strains Near the End of a Crack Traversing a Plate," Journal of Applied Mechanics, September 1957

4. Irwin, G. R., "Crack Toughness Evaluation Using Circumferentially Notched Round Bars," Note for Meeting of the ASTM Committee on Fracture Testing of High-Strength Metallic Materials, May 1961

5. Irwin, G. R., "Crack Extension Force for a Part-Through Crack in a Plate," Transactions of the ASME, Journal of Applied Mechanics, Paper No. 62-WA-13, November 1962

6. Irwin, G. R., "Fracture," Handbuch der Physik, Vol. VI, pp. 551-590, J. Springer Virlag, 1958

7. "Fracture Testing of High-Strength Sheet Materials," ASTM Special Bulletin, January 1960

8. Boyle, R. W., Sullivan, A. M., and Krafft, J. M., "Determination of Plane Strain Fracture Toughness with Sharply Notched Sheets," Welding Journal, Vol. 42 (9), Research Supplement, p. 428, 1962

9. ASTM Committee on FTHSSM, "Progress in the Measurement of Fracture Toughness and the Application of Fracture Mechanics to Engineering Problems," Materials Research and Standards, Vol. 4, No. 3, March 1964

APPENDIX I

TABLES

Table 1: CHEMICAL COMPOSITION OF MATERIALS

MATERIAL	CHEMICAL COMPOSITION (% by Weight)*													
	C	Mn	P	S	Si	Ni	Cr	Mo	Al	V	Co	Zr	Ti	Fe
6Al-4V Titanium Plate per AMS 4911 0.50 x 0.36 x 0.36 in. Heat No. 32125	0.02	--	--	--	--	--	--	--	6.[illegible]	4.[illegible]	--	--	Bal	0.17
18Ni (300) 0.250 x 36 x 72 in. Plate Heat No. 3951003	0.27	0.05	0.006	0.009	0.01	18.80	0.10	4.5[illegible]	0.05	--	8.98	--	0.63	Bal
Ladish D6A-C Steel Hot-rolled, Annealed 0.50 x 0.36 x 0.60 in. Heat No. 3950937 (8) pcs	0.4[illegible]	0.84 0.82**	0.006	0.006	0.24 0.30**	0.56 0.59**	1.10 0.98**	1.00 0.99**	--	0.08 0.08**	--	--	--	Bal
Ladish D6A-C 0.375 x 36 x 60 in. Plate (10) pcs Heat No. 3950935	0.44	0.78	0.008	0.007	0.24	0.56	1.09	0.98	--	0.09	--	--	--	Bal
Ladish D6A-C Ametco Weld Filler Wire (0.06 in. diam)	0.26 0.32	0.60 0.90	0.015 max	0.015 max	0.15 0.30	0.40 0.70	0.90 1.20	0.90 1.10	-- --	0.08 max	-- --	-- --	-- --	Bal
MI-88 Linde Weld Filler Wire (0.06 diam)	0.04 max	1.50 2.00	0.010 max	0.010 max	0.15 0.30	1.40 1.30	0.25 max	0.20 0.40	0.15 max	0.05 max	0.25 max	0.15 max	0.10 max	Bal

* As Certified by Material Suppliers

** Spectrographic Check Upon Receipt of the Material

Table 2: TENSILE PROPERTIES OF LADISH D6A-C STEEL PLATE
Tested at Room Temperature in Various Heat Treatment Conditions

SPECIMEN NUMBER	TEMPERING TEMPERATURE (°F)	GRAIN DIRECTION*	DIAMETER OF GAGE AREA (in.)	ULTIMATE STRENGTH (ksi)	YIELD STRENGTH (ksi)		ELONGATION (% in 1 in.)	REDUCTION OF AREA (%)
					Offset 0.2%	Offset 0.02%		
S-1	400	L	0.2509	309.3	219.4	167.8	11	38
S-2	400	L	0.2489	316.8	224.4	175.2	9	20
S-3	500	L	0.2479	292.9	257.8	239.0	7	25
S-4	500	L	0.2485	292.7	256.4	242.2	11	45
S-5	600	L	0.2492	278.4	247.2	240.1	9	37
S-6	600	L	0.2467	279.0	246.8	238.7	10	44
S-7	800	L	0.2495	250.3	232.1	224.9	11	44
S-8	800	L	0.2465	249.8	231.0	224.1	11	49
S-9	1000	L	0.2488	225.1	212.1	207.0	11	41
S-10	1000	L	0.2494	226.6	215.5	212.0	12	51

* L = Longitudinal grain direction

Table 3: STATIC FRACTURE TOUGHNESS OF LADISH D6A-C STEEL PLATE
Tested at Room Temperature in Various Heat Treatment Conditions

SPECIMEN NUMBER	DOUBLE TEMPERING TEMPERATURE (°F)	GRAIN DIRECTION *	INITIAL NOTCH EXTENSION BY FATIGUE **				SHANK DIAMETER (in.)	NOTCH DIAMETER (in.)		NET AREA FRACTURE STRESS (ksi)	σ_N/σ_{YS} Ratio ***	FRACTURE TOUGHNESS, K_{Ic} (ksi$\sqrt{\text{in.}}$)	REMARKS
			1st Run		2nd Run								
			Max Net Stress (ksi)	Cycles (1000)	Max Net Stress (ksi)	Cycles (1000)		After Machining	After Fatigue				
R-1	400	L	40	5	--	--	0.5015	0.351	0.351	250.8	1.13	79.8	Blunt Notch
R-2	400	L	40	47	60	28	0.5030	0.351	0.350	171.2	0.77	51.8	
R-3	500	L	60	14	--	--	0.5009	0.352	0.332	161.7	0.63	48.3	Eccentric Notch
R-4	500	L	60	18	--	--	0.5009	0.350	0.340	165.2	0.64	49.6	Eccentric Notch
R-5	600	L	40	100	50	28	0.5007	0.353	0.351	209.1	0.85	63.1	
R-6	600	L	60	50	70	11	0.5024	0.355	-----	-----	----	----	Broke in Fatigue
R-7	800	L	60	50	--	--	0.5011	0.356	0.353	245.2	1.05	76.9	
R-8	800	L	60	40	--	--	0.5012	0.350	0.348	260.7	1.13	82.9	
R-9	1000	L	60	23	--	--	0.4995	0.353	-----	-----	----	----	Broke in Fatigue
R-10	1000	L	60	11	--	--	0.5019	0.354	0.350	266.0	1.24	86.8	

* L = Longitudinal grain direction
** Initial notch extension by fatigue was done at room temperature with minimum/maximum stress ratio of 0.06
*** Ratio of the net area fracture stress over the average 0.2% offset yield strength

Table 4: STATIC FRACTURE TOUGHNESS AND CYCLIC FLAW GROWTH DATA OF LADISH D6A-C STEEL PLATE

Tested at Room Temperature (Sharply Notched Round Bar Specimens)

SPECIMEN NUMBER	INITIAL NOTCH EXTENSION BY FATIGUE		SHANK DIAMETER (IN)	NOTCH DIAMETER (IN)			UNIAXIAL YIELD STRENGTH	MAX. TRAPEZOIDAL NET STRESS		NET AREA FRACTURE STRESS (ksi)	K_{Ii} (ksi$\sqrt{in.}$)	K_{Ic} (ksi$\sqrt{in.}$)	K_{Ii}/K_{Ic} (%)	CYCLES TO FAILURE
	Max. Net Stress	Cycles (1000)		After Machining	After Initial Fatigue	After Trapezoidal Loading		Initial, σ_{ni} (ksi)	Critical, σ_n (ksi)					
R-11	70	7	0.500	0.354	0.349	--	247	--	--	177.6	--	53.5	--	--
R-12	70	2	0.501	0.350	0.347	0.332	247	149.0	163.1	163.1	44.4	48.9	90.8	112
R-13	70	2	0.501	0.353	0.352	--	247	--	--	176.2	--	53.0	--	--
R-14*	--	--	--	--	--	--	--	--	--	--	--	--	--	--
R-15	70	2	0.502	0.355	0.350	0.325	247	117.4	136.8	136.8	34.7	40.7	85.2	651
R-16	70	2	0.500	0.356	0.352	0.329	247	132.2	150.7	150.7	39.1	45.0	86.9	331
R-17	70	2	0.501	0.354	0.352	0.348	247	160.3	164.7	164.7	48.0	49.4	97.2	21
R-18	70	2	0.500	0.355	0.350	0.337	247	143.4	154.8	154.8	42.7	48.0	88.9	188
R-19	70	7	0.502	0.354	0.346	--	247	--	--	171.2	--	51.4	--	--
R-20	70	6	0.501	0.354	0.320	0.316	247	130.4	134.4	134.4	38.7	39.9	97.0	6
R-21	70	2	0.501	0.352	0.347	0.342	247	170.8	177.5	177.5	51.3	53.4	96.1	84
R-22*	--	--	--	--	--	--	--	--	--	--	--	--	--	--
R-23	70	6	0.501	0.354	0.330	0.323	247	123.2	128.5	128.5	36.6	38.1	95.8	30
R-24	70	6	0.500	0.350	0.340	0.290	247	115.5	136.6	136.6	34.1	40.6	84.0	866
R-25	70	2	0.500	0.354	--	--	247	--	--	225.0	--	69.7**	--	--
R-26	70	6.5	0.500	0.355	0.326	--	247	114.2	--	114.2	--	33.7***	--	--
R-27	70	7	0.500	0.355	0.349	0.306	247	109.7	142.8	142.8	32.4	42.5	76.2	745
R-28	70	7	0.500	0.354	0.350	--	247	--	--	186.2	--	56.2	--	--
R-29	70	7	0.502	0.353	0.343	--	247	--	--	145.7	--	43.4	--	--

*Not tested
**Inadequate fatigue extension
***Eccentric notch

Table 5: STATIC FRACTURE TOUGHNESS AND CYCLIC FLAW GROWTH DATA OF LADISH D6A-C STEEL PLATE

Tested at Room Temperature (Surface Flawed Specimens)

SPECIMEN NUMBER	SPECIMEN SIZE (in.)		INITIAL FLAW EXTENSION BY FATIGUE		INITIAL FLAW SIZE			UNIAXIAL YIELD MATERIAL STRENGTH (ksi)	CRITICAL FLAW SIZE			MAX TRAPEZOIDAL TENSILE STRESS (ksi)	MAX STRESS AT FRACTURE (ksi)	K_{Ii} (ksi $\sqrt{in.}$)	K_{Ic} (ksi $\sqrt{in.}$)	K_{Ii}/K_{Ic} (%)	CYCLES TO FAILURE
	Thickness, t	Width, w	Max Gross Stress (ksi)	Cycles (1000)	Depth, a_i (in.)	Length, $2c_i$ (in.)	Flaw-Shape Parameter, Q		Depth, a (in.)	Length, 2c (in.)	Flaw-Shape Parameter, Q						
LS-1	0.248	6.02	30.0	10	0.066	0.252	1.450	247	-	-	-	-	119.8	-	50.0	100.0	-
LS-2	0.248	6.02	30.0	15	0.132	0.453	1.575	247	-	-	-	-	80.2	-	45.4	100.0	-
LS-3	0.248	6.02	30.0	14	0.066	0.243	1.505	247	0.120	0.343	1.770	99.3	108.8	40.7	55.1	73.9	2067 *
LS-4	0.248	6.02	30.0	14	0.065	0.256	1.425	247	-	-	-	-	128.4	-	53.6	100.0	-
LS-5	0.247	6.02	30.0	30	0.076	0.237	1.665	247	0.110	0.331	1.735	108.2	108.2	45.2	53.2	85.0	549
LS-6	0.248	6.02	30.0	30	0.079	0.272	1.565	247	0.114	0.352	1.680	98.2	98.2	43.1	50.0	86.2	558
LS-7	0.248	6.02	30.0	30	0.078	0.255	1.615	247	0.136	0.337	1.995	99.3	99.3	42.6	50.6	84.2	1322
LS-8	0.249	6.02	30.0	13	0.141	0.457	1.637	247	0.158	0.473	1.730	68.0	-	39.0	-	-	136 **
					0.158	0.473	1.730	247	0.207	0.568	1.846	68.0	68.0	40.2	47.2	85.2	816

* No Failure

** No Failure — Test interrupted for 3.8 hours due to equipment failure; specimen was left under sustained stress of 9.7 ksi

Table 6: RELATIONSHIP BETWEEN DIRECTION OF RUNNING FRACTURE AND GRAIN ORIENTATION: Ladish D6A-C Sharply Notched Round Bar Specimens

NONNORMALIZED				NORMALIZED			
Static Test		Cyclic Test		Static Test		Cyclic Test	
Specimen No.	Angle (Degrees)	Specimen No.	Angle (Degrees)	Specimen No.	Angle (Degrees)	Specimen No.	Angle (Degrees)
R-1	72	R-12	60	S-1	14	S-[illegible]**	[illegible]
R-2	82	R-14	37	S-4*	48	S-[illegible]**	[illegible]
R-3	27	R-15	48				
R-4	20	R-16	60				
R-5	78	R-17	25				
R-7	53	R-18	30				
R-8	90	R-20	30				
R-10	12	R-21	53				
R-11	0	R-22	18				
R-13	3	R-24	0				
R-19	85	R-27	67				
R-25	62						
R-26	58	S-64*	57				
R-29	77	S-65	54				
S-66*	37						

* Moist
** Dessicated

Table 7: EFFECT OF VARIATIONS IN HEAT TREATMENT AND TEST CONDITIONS UPON MEASURED FRACTURE TOUGHNESS OF LADISH D6A-C STEEL

Sharply Notched Round Bar Specimens

SPECIMEN NUMBER	INITIAL NOTCH EXTENSION BY FATIGUE		SHANK DIAMETER (in.)	NOTCH DIAMETER (in.)			HEAT TREATMENT	ENVIROMENTAL CONDITIONS	MAXIMUM TRAPEZOIDAL NET STRESS		NET AREA FRACTURE STRESS (ksi)	K_{Ii} (ksi$\sqrt{in.}$)	K_{Ic} (ksi$\sqrt{in.}$)	K_{Ii}/K_{Ic} (%)	CYCLES TO FAILURE
	Max. Net Stress (ksi)	Cycles (1000)		After Machining	After Initial Fatigue	After Trapezoidal Loading			Initial, σ_{ni} (ksi)	Critical, σ_{ni} (ksi)					
S-1	40	120	0.500	0.357	0.357	--	1	Air	--	--	268	--	84.4*	--	--
S-2	70	9	0.500	0.351	0.346	0.335	1	Dry	143.6	153.5	153.5	42.8	45.8	93.4	256
S-3	60 70	11 5	0.500	0.352	0.346	0.325	1	Dry	120.2	136.1	136.1	35.6	40.4	88.1	891
S-4	70	9	0.500	0.348	0.328	--	1	Wet	132.5	--	132.5	--	39.3**	--	--
S-64	70	6	0.500	0.352	0.349	0.347	2	Wet	118.0	119.5	119.5	34.9	35.1	99.0	14
S-65	70	6	0.500	0.353	0.349	0.342	2	Air	118.0	122.9	122.9	34.9	37.4	93.3	157
S-66	70	6	0.500	0.352	0.348	--	2	Wet	119.0	--	119.0	--	35.2	--	--

*Inadequate fatigue extension

**Eccentric fatigue extension

1 Normalize at 1650°F for 1 hour, austenitize at 1550°F for 1 hour salt quench to 400°F, double temper at 600°F for 2 hours each

2 Same as 1 except normalizing cycle was omitted

Table 8: TENSILE AND BEND TEST DATA OF LADISH D6A-C WELD TEST PANELS

Tested at Room Temperature

PANEL NUMBER	WELD WIRE	SPECIMEN NUMBER	SPECIMEN SIZE (in.) Thickness	SPECIMEN SIZE (in.) Width	BEND DIRECTION (TENSION SIDE)	BEND ANGLE (DEGREES)	[illegible] (0.2% [illegible])	Ult[illegible]	[illegible]
1	MI-88	1T	0.355	0.488	---	---	197.6	219.6	
		1F	0.339	1.00	Face	50	---	---	No Failure
		1R	0.339	1.00	Root	19	---	---	
2	MI-88 + ARMETCO	2T	0.362	0.500	---	---	229.2	258.5	
		2F	0.339	1.00	Face	20	---	---	
		2R	0.339	1.00	Root	22	---	---	
3	ARMETCO	3T	0.352	0.494	---	---	232.7	266.0	
		3F	0.343	1.00	Face	15	---	---	
		3R	0.343	1.00	Root	20	------		

Table 9: STATIC FRACTURE TOUGHNESS AND CYCLIC FLAW GROWTH DATA FOR LADISH D6A-C PLATE

Tested at Room Temperature (17-inch Diameter Tanks)

TANK NUMBER	TANK SIZE (in.)		INITIAL FLAW EXTENSION BY FATIGUE			INITIAL FLAW SIZE			UNIAXIAL YIELD STRENGTH OF MATERIAL (ksi)	CRITICAL FLAW SIZE			MAXIMUM CYCLIC HOOP STRESS (ksi)	BURST HOOP STRESS (ksi)	K_{Ii} (ksi$\sqrt{in.}$)	K_{Ic} (ksi$\sqrt{in.}$)	K_{Ii}/K_{Ic} (%)	CYCLES TO FAILURE
	Thickness, t (in.)	Inside Diameter (in)	Cyclic Stress (ksi) Maximum	Cyclic Stress (ksi) Minimum	Cycles	Depth, a_i (in.)	Length, $2c_i$ (in.)	Flaw-Shape Parameter, Q		Depth, a (in.)	Length, 2c (in.)	Flaw-Shape Parameter, Q						
I	0.253	17.07	25.4 33.6 168.6 50.6	19.2 30.1 0 10.1	30,000 50,000 1* 12,000	0.067	0.278	1.400	247.0	0.098	0.300	1.630	104.9	--	44.7	50.4	88.7	812
II	0.250	17.05	33.9	29.6	170,000	0.060	0.260	1.345	247.0	--	--	--	--	168.8	--	--	--	---
III	0.253	17.09	33.5 50.7	29.3 10.1	148,000 10,000	0.096	0.300	1.670	247.0	0.106	0.326	1.685	[illegible]	--	45.0	47.0	[illegible]	14
IV	0.232	17.16	40.9	8.5	6,250	0.127	0.427	1.605	247.0	0.174	0.540	1.695	74.9	--	40.9	46.8	87.4	1214
V	0.254	17.06	50.4	10.1	9,226	0.082	0.267	1.630	247.0	0.148	0.393	1.885	87.3	--	38.1	47.6	80.0	2092
VI	0.251	17.10	40.9	8.5	6,000	0.151	0.500	1.860	247.0	--	--	--	--	73.2	--	40.6	---	---

*Unsuccessful attempt to burst-test

†Inadequate fatigue extension, calculated K_{Ii} = 68.9 ksi $\sqrt{in.}$

‡Burst test

Table 10: TENSILE PROPERTIES OF 6Al-4V TITANIUM PLATE IN ANNEALED CONDITIONS
Tested at -320°F in Liquid Nitrogen

SPECIMEN NUMBER	GRAIN DIRECTION*	DIAMETER OF GAGE AREA (in.)	ULTIMATE STRENGTH (ksi)	YIELD STRENGTH (ksi)		ELONGATION (% in 1 in.)	REDUCTION OF AREA (%)
				Offset 0.2%	Offset 0.02%		
T-1	L	0.2484	224.3	212.1	189.4	8.0	17.9
T-2	L	0.2485	223.7	210.7	189.0	7.5	22.9
T-3	L	0.2493	224.1	214.1	194.6	8.5	18.4
		Average	224.0	212.3	191.1	8.0	19.7

* L = Longitudinal Grain Direction

Table 11: STATIC FRACTURE TOUGHNESS AND CYCLIC FLAW CHARACTERISTICS OF 6Al-4V TITANIUM PLATE

Tested at -320 F (Sharply Notched Round Bar Specimens)

SPECIMEN NUMBER	INITIAL NOTCH EXTENSION BY FATIGUE AT R.T.*		SHANK DIAMETER (in.)	NOTCH DIAMETER (in.)			UNIAXIAL YIELD STRENGTH	MAXIMUM TRAPEZOIDAL NET STRESS		NET AREA FRACTURE STRESS (ksi)	K_{Ii} (ksi $\sqrt{in.}$)	K_{Ic} (ksi $\sqrt{in.}$)	K_{Ii}/K_{Ic} (%)	CYCLES TO FAILURE
	Maximum Net Stress (ksi)	Cycles		After Machining	After Initial Fatigue	After Trapezoidal Loading		Initial, σ_{ni} (ksi)	Critical, σ_n (ksi)					
R-1	40	1205	0.499	0.353	0.349	0.325	212.3	144.2	166.7	166.7	43.2	50.5	85.5	195
R-2	40	1000	0.501	0.353	0.350	0.335	212.3	157.3	172.0	172.0	47.5	52.5	90.5	60
R-3	40	800	0.501	0.354	0.353	--	212.3	--	--	203.8	--	63.1	--	--
R-4	40	753	0.501	0.354	0.353	--	212.3	--	--	195.4	--	60.2	--	--
R-5	40	1000	0.501	0.354	0.350	0.343	212.3	174.8	181.5	181.5	53.2	55.4	96.0	24
R-6	40	1000	0.501	0.352	0.348	0.313	212.3	113.3	140.4	181.5	33.6	42.1	79.8	470
R-7	40	703	0.500	0.353	0.352	--	212.3	--	--	205.0	--	63.5	--	--
R-8	40	1021	0.498	0.354	0.351	0.331	212.3	128.7	144.3	144.3	38.4	43.4	85.5	168
R-9	40	2500	0.500	0.352	0.345	0.326	212.3	167.9	187.0	187.0	51.5	57.3	89.9	64
R-10	40	2000	0.501	0.353	0.345	0.342	212.3	183.5	186.7	186.7	56.1	57.2	98.1	19

*R.T. Room Temperature

Table 12: CYCLIC FLAW GROWTH DATA FOR 6Al-4V TITANIUM PLATE

Tested at -320°F (Surface Flawed Specimens)

SPECIMEN NUMBER	SPECIMEN SIZE (in.)		INITIAL FLAW EXTENSION BY FATIGUE AT R.T.*		INITIAL FLAW SIZE			UNIAXIAL YIELD STRENGTH OF MATERIAL (ksi)	CRITICAL FLAW SIZE			MAXIMUM TRAPEZOIDAL TENSILE STRESS (ksi)	MAXIMUM STRESS AT FRACTURE (ksi)	K_{Ii} (ksi $\sqrt{in.}$)	K_{Ic} (ksi $\sqrt{in.}$)	K_{Ii}/K_{Ic} (%)	CYCLES TO FAILURE
	Thickness, t	Width, w	Max. Gross Stress (ksi)	Cycles (1000)	Depth, a_i (in.)	Length, $2c_i$ (in.)	Flaw Shape Parameter, Q		DEPTH, a (in.)	LENGTH, 2c (in.)	Flaw Shape Parameter, Q						
TS-1	0.257	6.00	50	6	0.081	0.563	1.115	212.3	0.065	0.622	1.095	128.1	128.1	67.5	69.7	96.8	7
TS-2	0.255	5.99	50	7	0.109	0.436	1.425	212.3	0.136	0.632	1.350	94.7	94.7	51.2	58.7	87.2	97
TS-3	0.266	6.00	50	7	0.134	0.639	1.330	212.3	0.190	0.709	1.505	75.0	75.0	46.4	56.0**	82.9	317
TS-4	0.252	6.01	50	7	0.058	0.450	1.045	212.3	--	--	--	--	150.2	--	69.1	--	--

* R.T. = Room temperature

** Average K_{Ic} value for the average a/t ratio for initial and critical flaw depths as read from Figure 13.

Table 13: TENSILE PROPERTIES OF 18Ni (300) MARAGING STEEL PLATE
Tested at Room Temperature (Flat Tensile Specimens)

SPECIMEN NUMBER	SPECIMEN SIZE (in.)		GRAIN DIRECTION	AGING TEMPERATURE (°F) 3 HOURS	ULTIMATE STRENGTH, σ_{ult} (ksi)	YIELD STRENGTH (ksi)		HARDNESS, R_c	ELONGATION (%)	
	Thickness, t	Width, w				0.2% Offset in 2-in. Gage, σ_{ys}	0.02% Offset in 2-in. Gage, σ_{pl}		Gage Length (0.5 in.)	Gage Length (1.0 in.)
MT-1	0.285	0.498	L	800	257.2	248.0	219.8	52.0	25	16
MT-2	0.287	0.503	L	800	257.1	248.0	223.8	51.0	28	15
MT-3	0.288	0.503	L	850	268.9	260.0	233.1	52.0	28	15
MT-4	0.289	0.502	L	850	268.9	260.6	231.0	52.0	28	17
MT-5	0.290	0.502	L	900	284.5	277.6	248.7	53.0	28	16
MT-6	0.291	0.503	L	900	283.1	273.5	239.3	53.5	28	16
MT-7	0.291	0.504	L	950	291.7	283.5	246.7	53.5	22	14
MT-8	0.292	0.503	L	950	291.5	284.7	247.9	53.5	22	14

Table 14: EFFECT OF AGING TEMPERATURE UPON STATIC FRACTURE OF 18Ni (300) MARAGING STEEL

Tested at Room Temperature (Centrally Cracked Flat Specimens)

SPECIMEN NUMBER	SPECIMEN SIZE (in.)		INITAL CRACK EXTENSION BY FATIGUE		TOTAL CRACK LENGTH, 2c (in.)			AGING TEMPERATURE (°F)	UNIAXIAL YIELD STRENGTH (ksi)	MAX. STRESS AT POP-IN (ksi)	MAX. STRESS AT FRACTURE (ksi)	POP-IN K_{Ic} (ksi $\sqrt{in.}$)	K_c (ksi $\sqrt{in.}$)
	Thickness, t	Width, w	Max. Gross Stress (ksi)	Cycles	After EDM Machining	After Initial Fatigue	At Inception of Instability (Fracture)						
MC-1	0.291	5.94	34.5	1,550	0.80	1.04	1.04	800	248.0	76.5	76.5	99.2	--
MC-2	0.292	5.94	34.5	2,000	0.80	1.04	1.29	850	260.3	54.4	75.7	70.1	109.4
MC-3	0.290	5.94	34.5	4,000	0.80	1.05	1.80	900	275.5	54.5	119.9	70.9	213.5
MC-4	0.284	5.94	34.5	8,000	0.80	1.03	1.82	950	284.1	--	108.6	--	191.5

Table 15: STATIC FRACTURE TOUGHNESS AND CYCLIC FLAW GROWTH DATA FOR 18Ni (300) PLATE

Tested at Room Temperature (Surface Flawed Specimens)

SPECIMEN NUMBER	SPECIMEN SIZE (in.)		INITIAL FLAW EXTENSION BY FATIGUE		INITIAL FLAW SIZE			UNIAXIAL YIELD STRENGTH, σ_{ys} (ksi)	CRITICAL FLAW SIZE			MAXIMUM TRAPEZOIDAL TENSILE STRESS (ksi)	MAXIMUM STRESS AT FRACTURE (ksi)	K_{Ii} (ksi $\sqrt{in.}$)	K_{Ic} (ksi $\sqrt{in.}$)	K_{Ii}/K_{Ic} (%)	CYCLES TO FAILURE
	Thickness, t	Width, w	Max. Gross Stress (ksi)	Cycles	Depth, a_i (in.)	Length, $2c_i$ (in.)	Flaw Shape Parameter, Q		Depth, a_f (in.)	Length, $2c$ (in.)	Flaw Shape Parameter, Q						
MS-1	.289	6.01	30.0	33,000	.079	.273	1.415	275.5	--	--	--	--	247.0*	--			
	.289	3.50	--	--	.079	.273	1.415	275.5	--	--	--	--	257.4	--	118.5	--	--
MS-2	.291	6.01	30.0	30,000	.077	.271	1.575	275.5	--	--	--	112.6	--	48.7	--	--	1396 *)
	.291	3.51	--	--	.111	.328	1.730	275.5	.280	.690	1.995	112.6	118.2	--	82.3+)	59.1	2514**
MC-5	.288	3.50	30.0	28,000	.123	.401	1.566	275.5	--	--	--	--	173.0-)	--	94.8-)		
													177.8	--	97.4	--	--
MC-8	.290	3.50	30.0	30,000	.073	.262	1.425	275.5	.138	.390	1.705	220.0	220.0	97.4	121.8	80.0	232

*Grip failure at 247.0 ksi; specimen remachined to 3.5-inch wide gage area, then pulled to failure

*)Specimen failed in grip, then remachined to 3.5 gage area width and subjected to the same cyclic stress

**Flaw grew through the thickness

-)At the instant of pop

+)As calculated using 112.6 ksi stress

Table 16: CYCLIC CRACK GROWTH DATA FOR 18Ni (300) MARAGING STEEL
Tested at Room Temperature (Centrally Cracked Flat Specimens)

SPECIMEN NUMBER	SPECIMEN SIZE (in.)		INITIAL CRACK EXTENSION BY FATIGUE		TOTAL CRACK LENGTH, 2a* (in.)			UNIAXIAL YIELD STRENGTH (ksi)	MAXIMUM TRAPEZOIDAL TENSILE STRESS (ksi)	MAXIMUM STRESS AT POP-IN (ksi)	MAXIMUM STRESS AT FRACTURE (ksi)	K_f (ksi $\sqrt{in.}$)	K_{Ic} (POP) (ksi $\sqrt{in.}$)	K_c (ksi $\sqrt{in.}$)	$K_f/$[illegible] ([illegible])	CYCLES TO FAILURE
	Thickness, t	Width, w	Max. Gross Stress (ksi)	Cycles (1000)	After EDM Machining	After Initial Fatigue	At Fracture									
MS-3	0.288	6.012	30	15	.350	.502	1.50	275.5	140.0	--	140.0	176.4	--	235.5	74.9	17
MS-4	0.288	6.012	30	18	.350	.550	2.50	275.5	100.0	--	100.0	104.0	--	225.0	46.2	503

*As measured on fractured specimen taking [illegible] distance between tips of the tunnel and surface [illegible]

Best Available Copy

APPENDIX II

TEST SPECIMENS

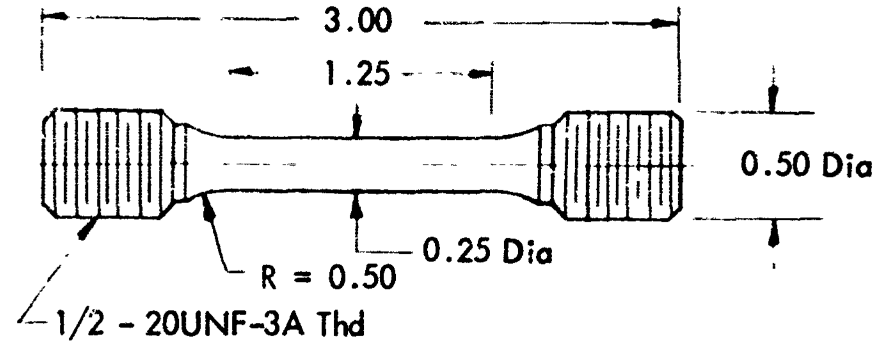

Dimensions in Inches

Figure 21: Smooth Tensile Specimen

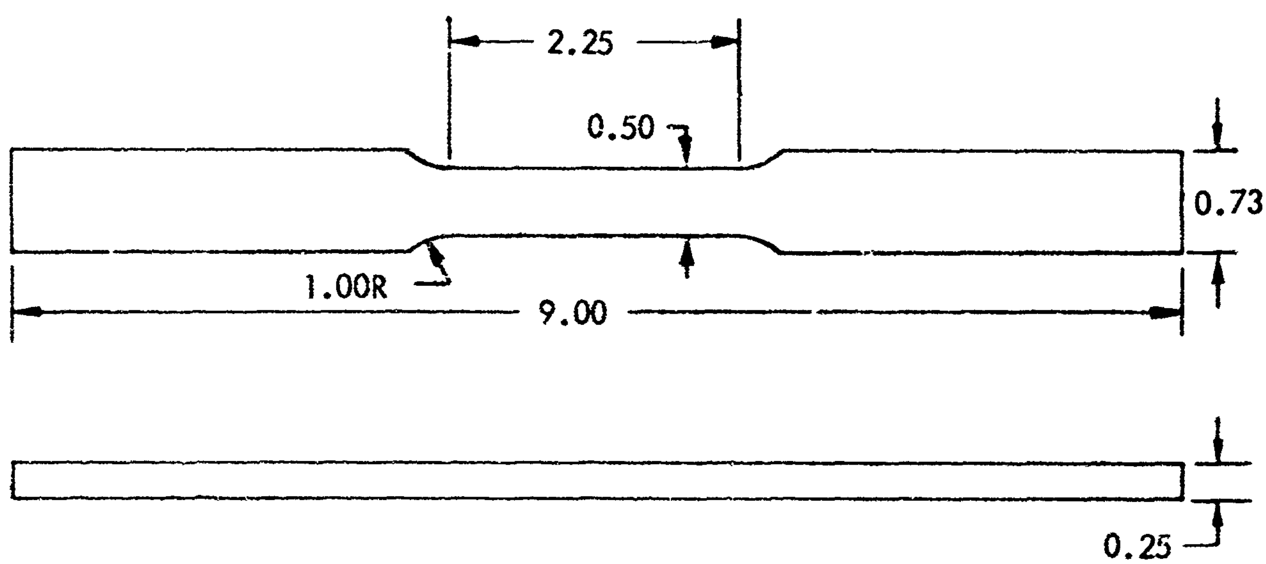

Dimensions in Inches

Figure 22: Flat Tensile Specimen

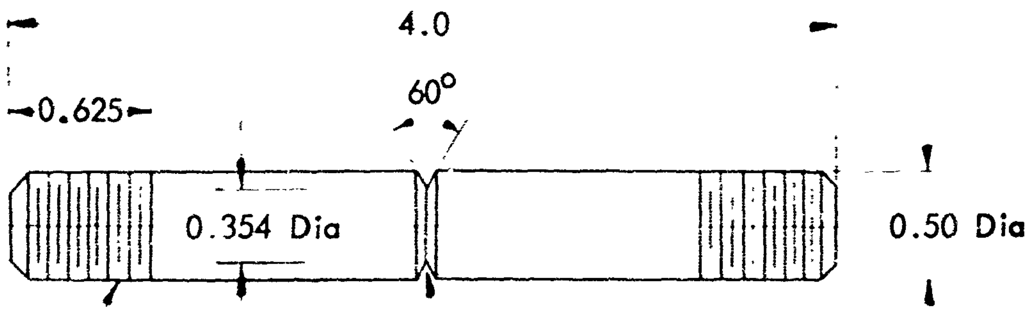

1/2 - 20UNF-3A Thd

Root Radius*

Dimensions in Inches

*The root radius is machined on a lathe using carefully ground tool bits. The specimen is then subjected to low-stress tension-tension to terminate the initial notch in a fatigue crack extending around the entire periphery of the initial notch.

Figure 23: Sharply Notched Round Bar Fracture Toughness Specimen

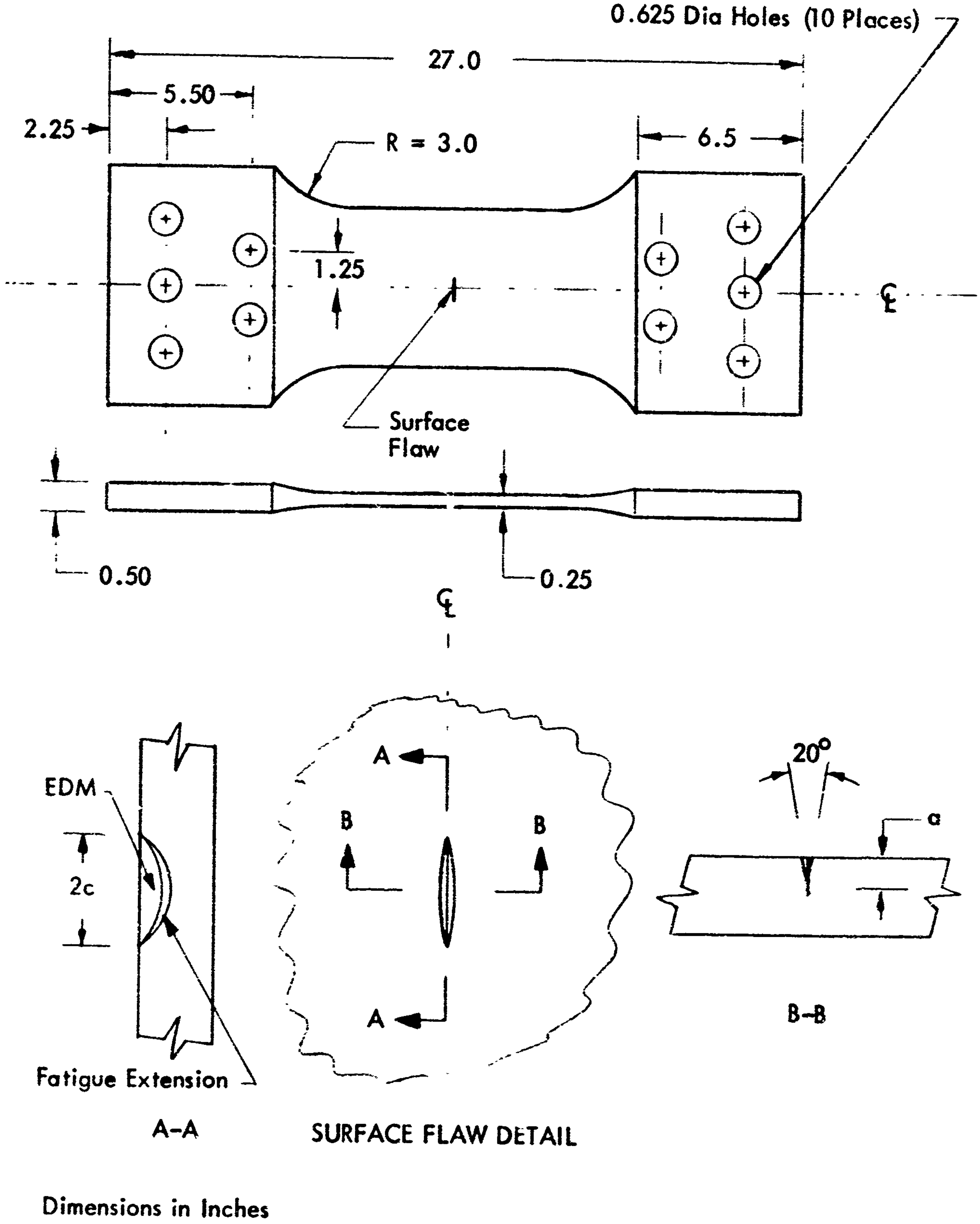

Figure 24: Surface Flawed Flat Fracture Toughness Specimen

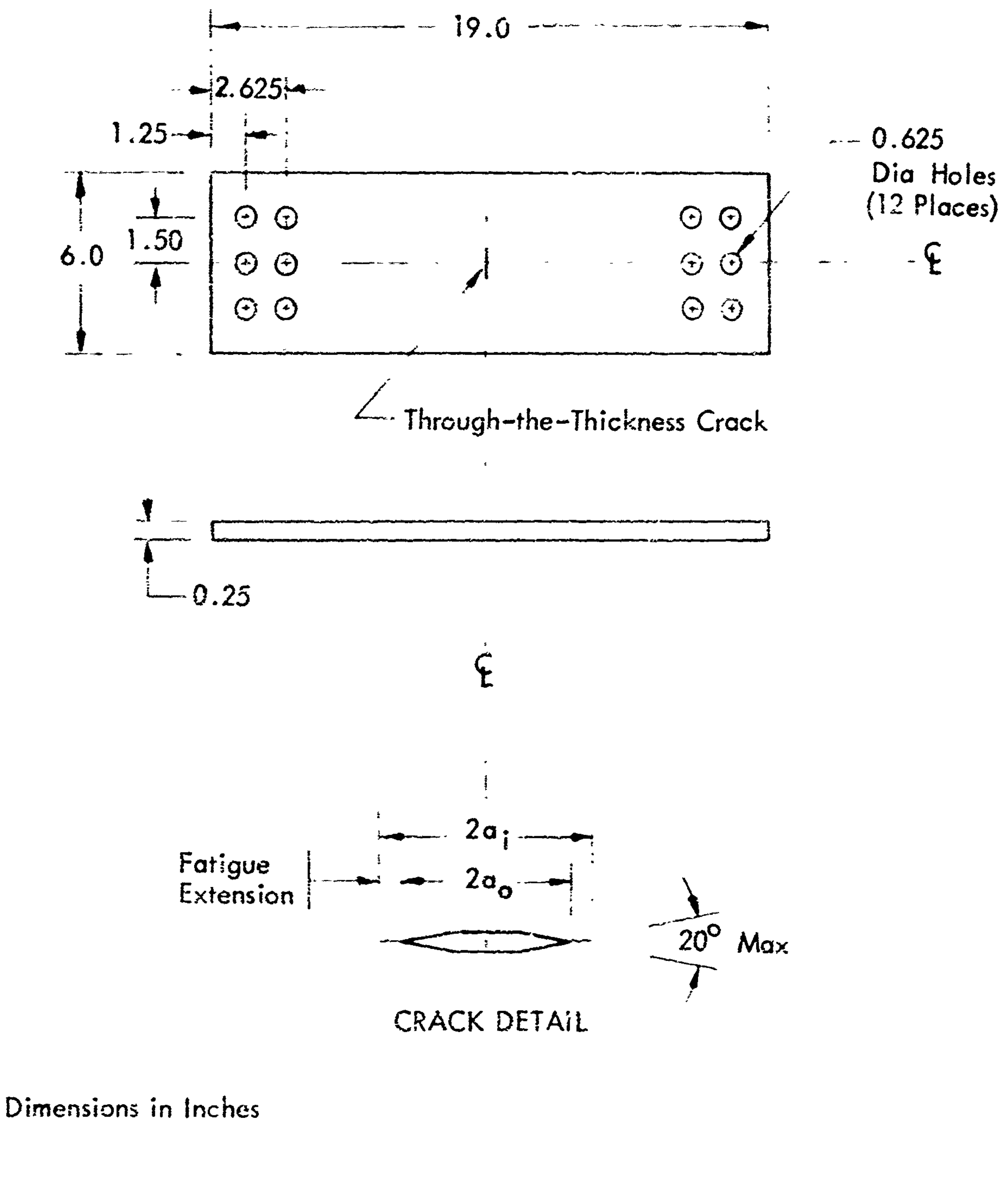

Figure 25: Through-the-Thickness Centrally Cracked Fracture-Toughness Specimen

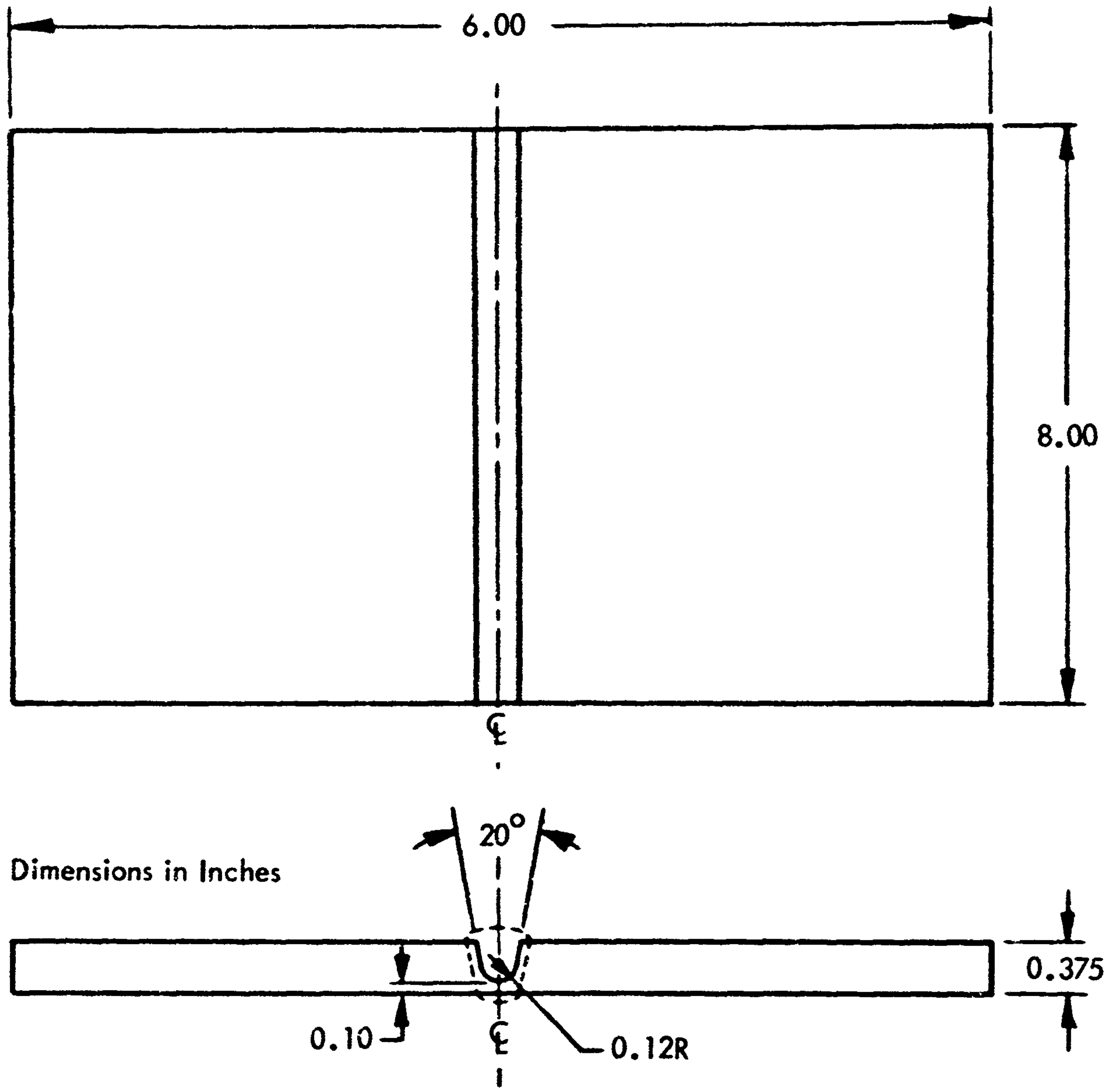

Figure 26: Weld Test Panel

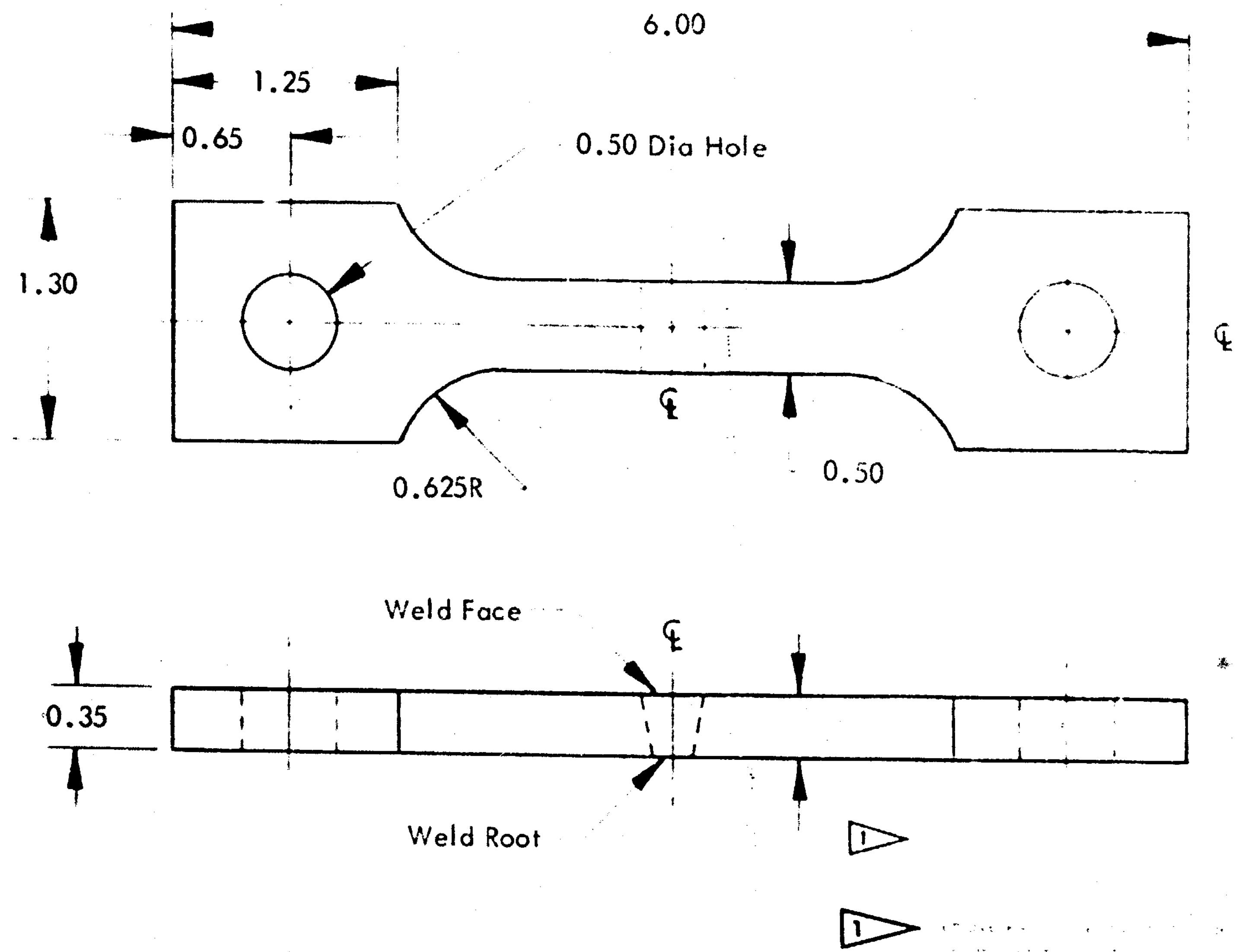

Figure 27: Tensile Test Specimen

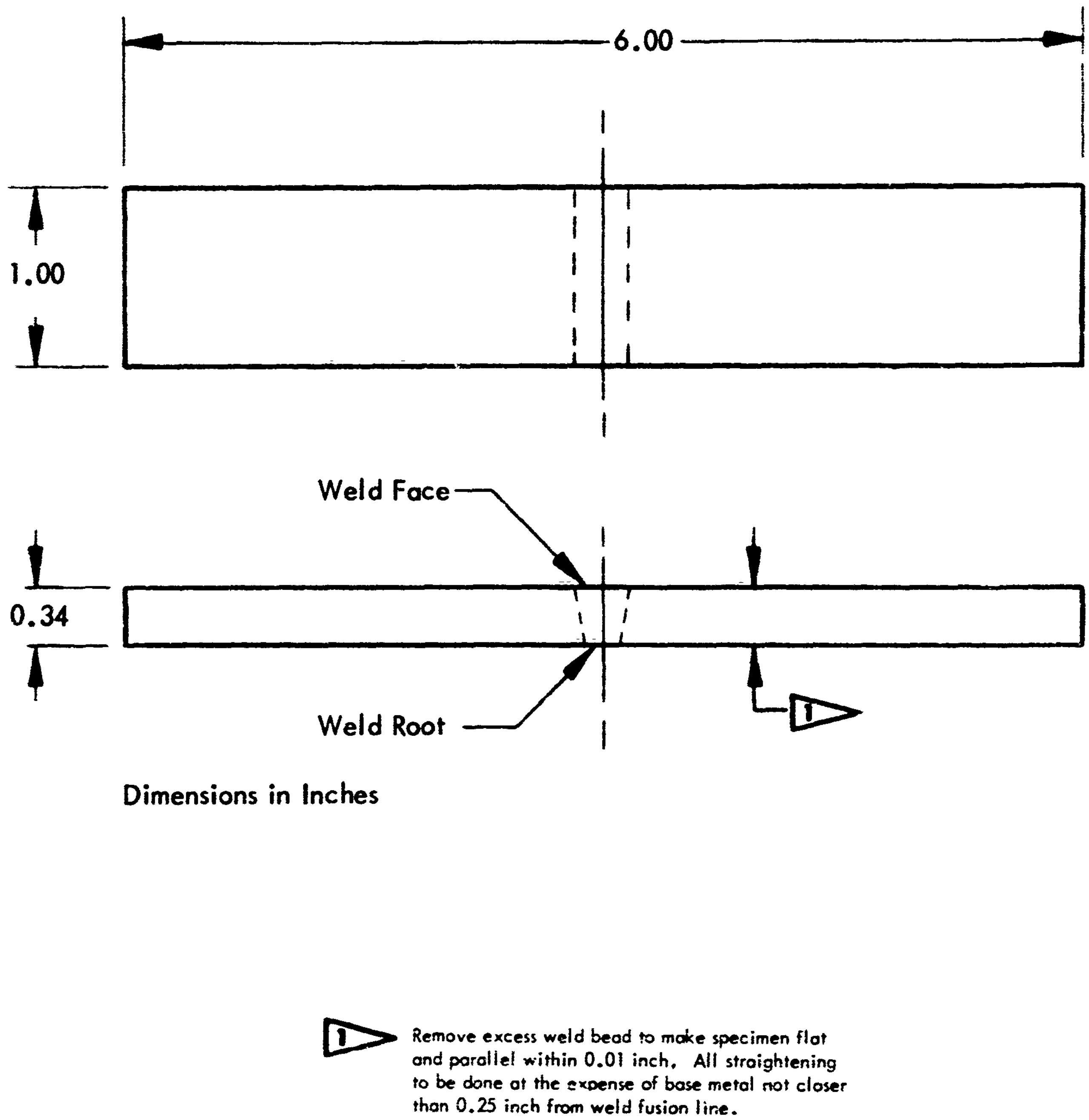

Figure 28: Bend Test Specimen

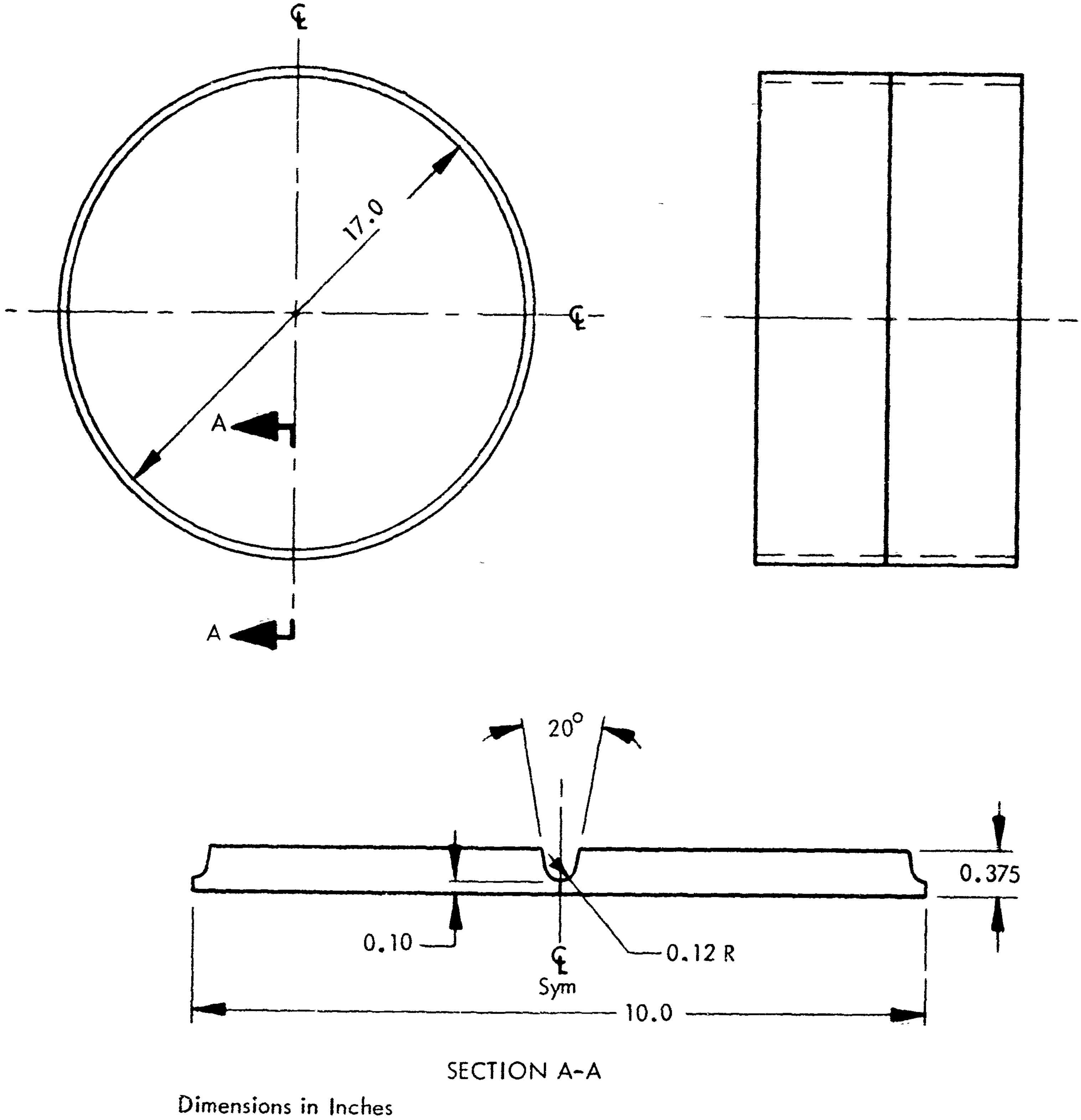

Figure 29: 17-Inch Diameter Test Shell

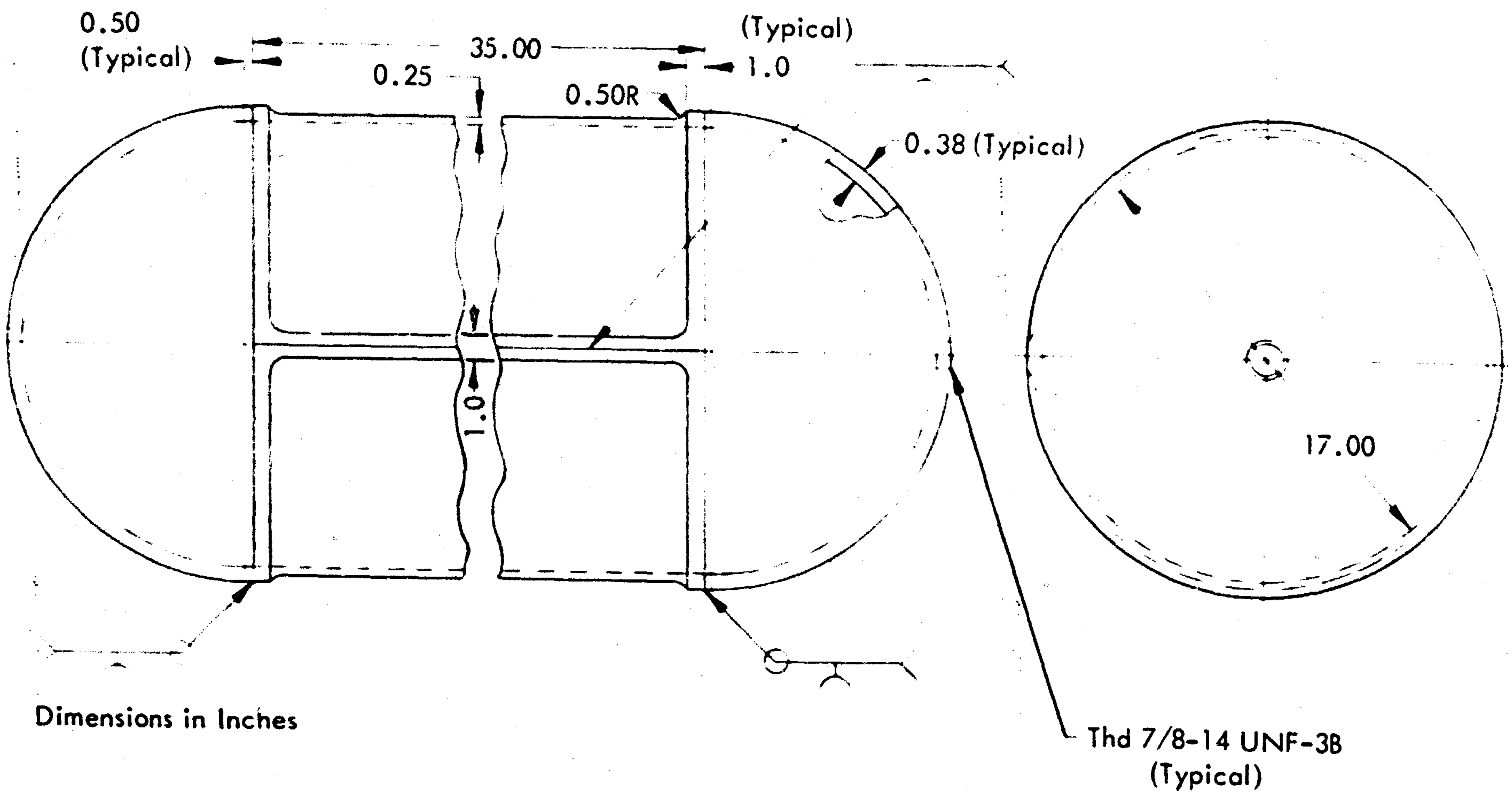

Figure 30: 17-Inch Diameter Test Pressure Vessel

APPENDIX III

TEST SETUP

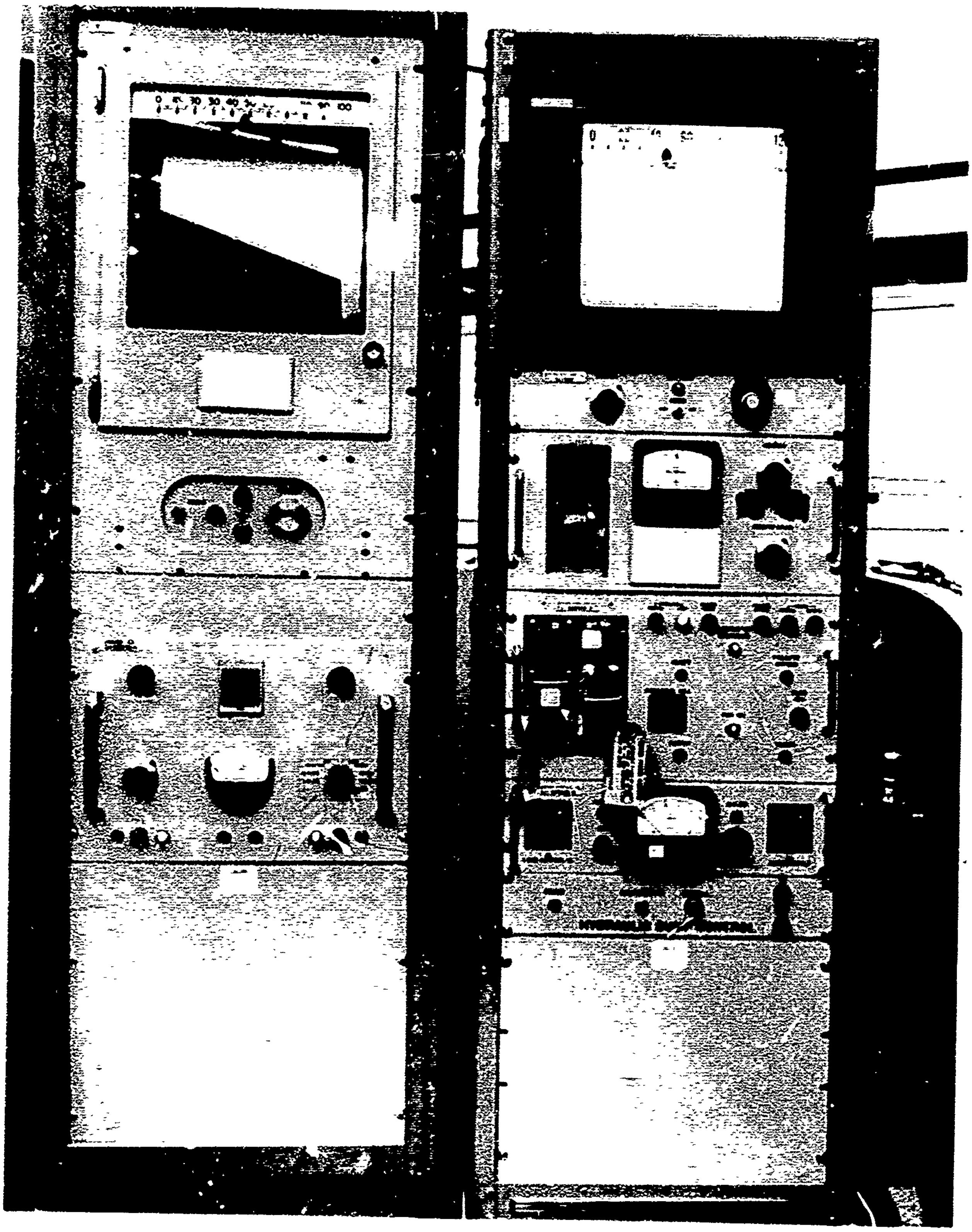

Figure 31: Trapezoidal Load Programmer

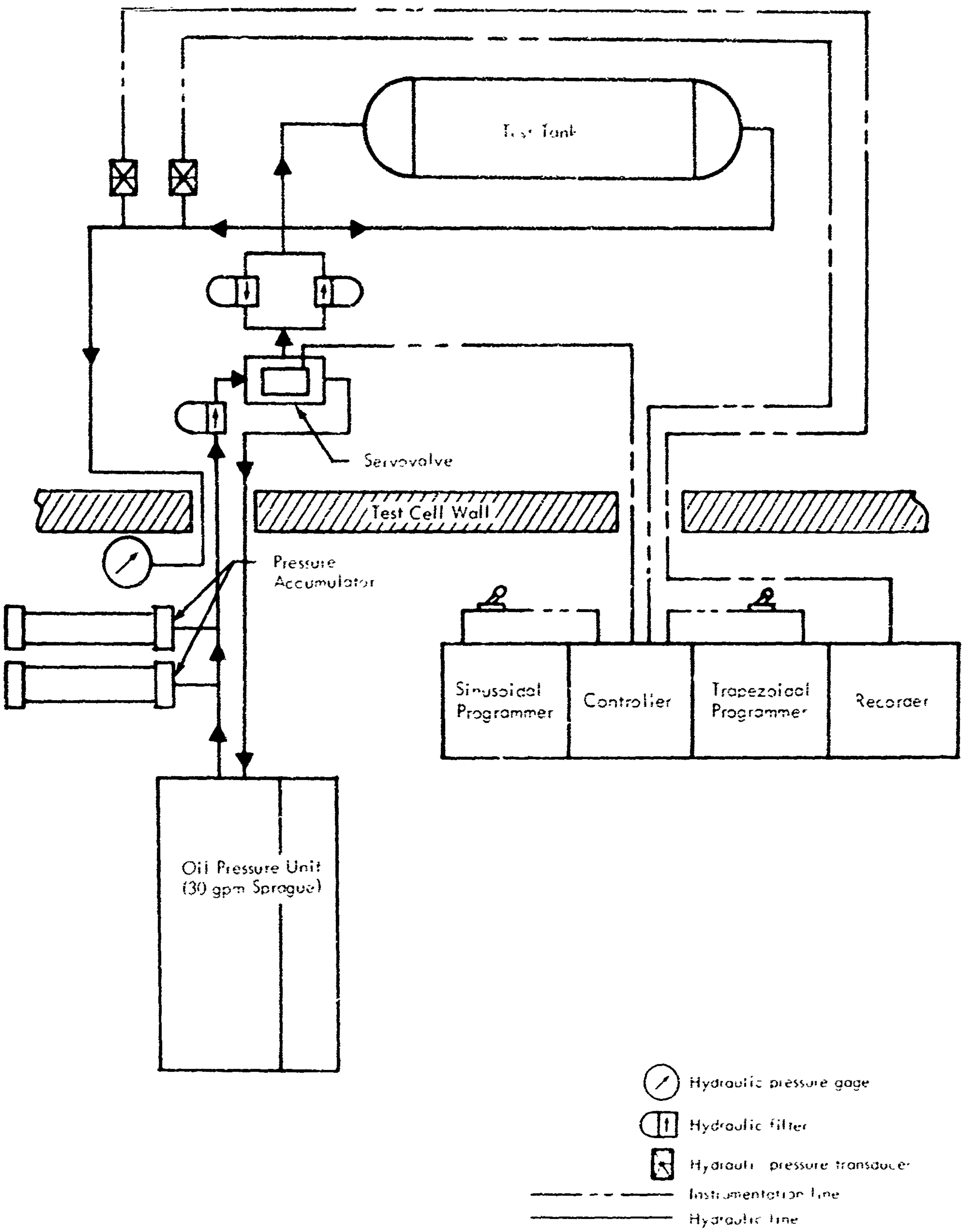

Figure 32: Schematic Representation of 17-Inch Diameter Pressure Vessel Test Setup

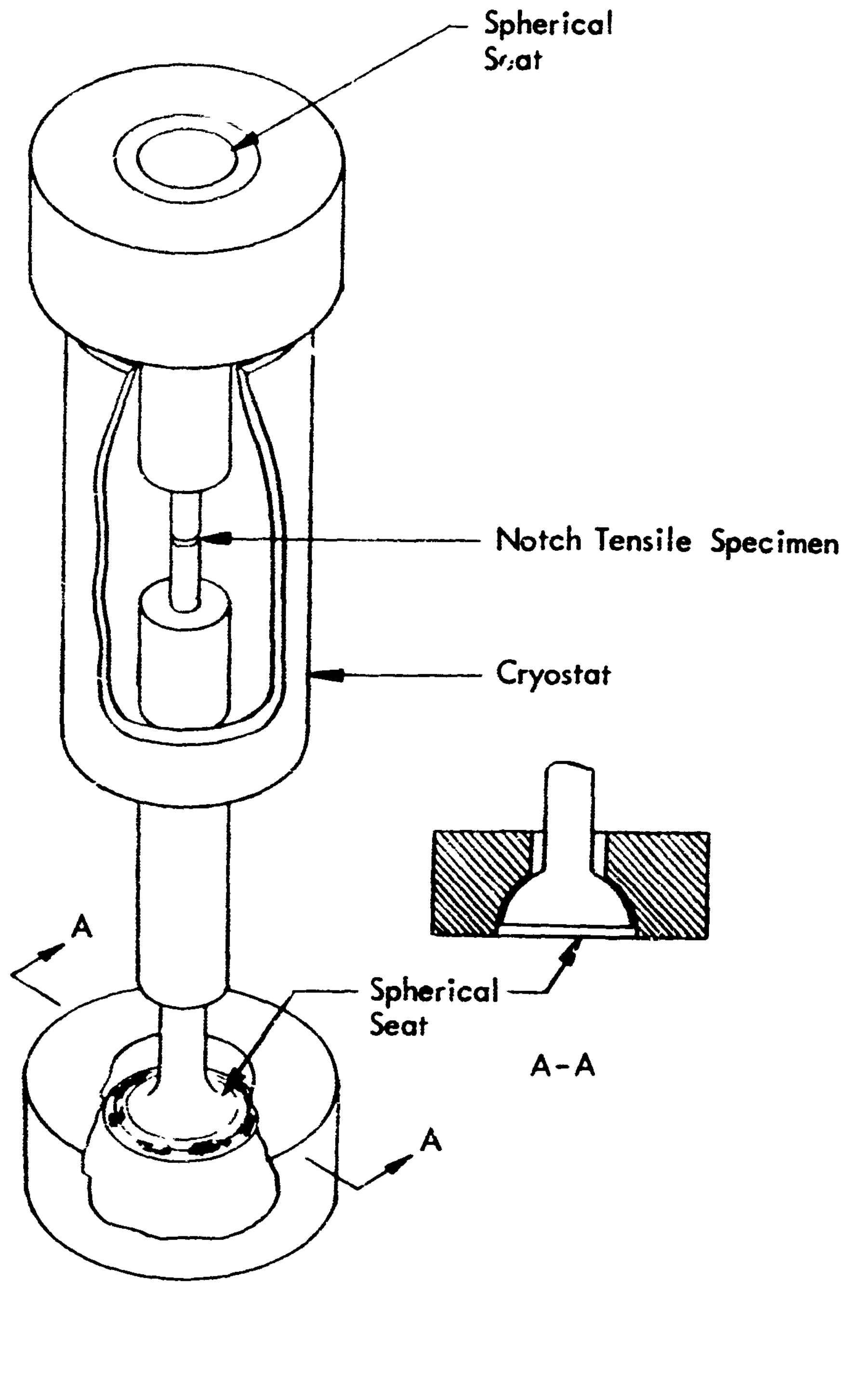

Figure 33: Schematic Representation of Test Fixture for Static and Cyclic Testing

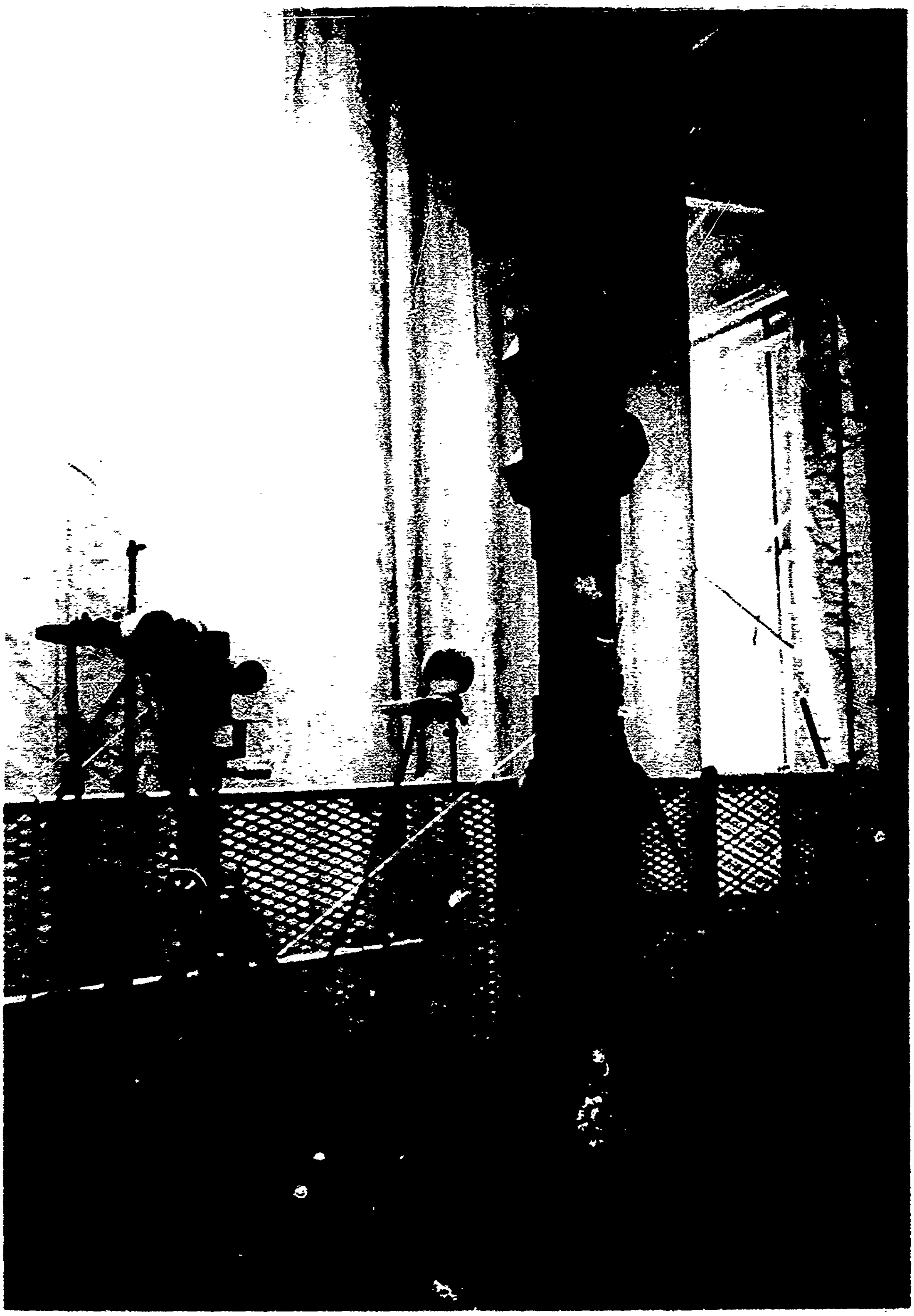

Figure 34: Photographic Setup for Recording Crack Growth in 18 Ni(300) Test Specimen

APPENDIX IV

SAMPLE FRACTOGRAPHS

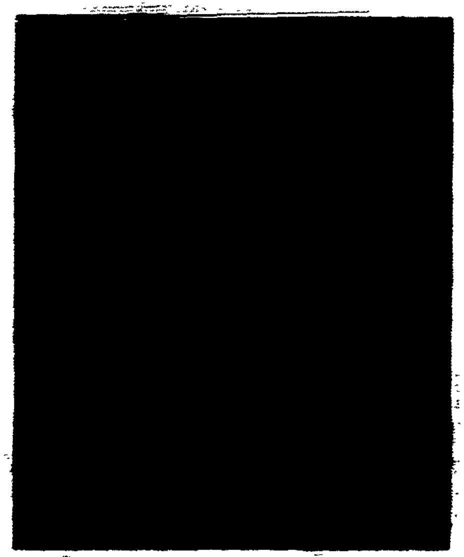

7X R-26

ECCENTRIC FATIGUE NOTCH (LOW K_{Ic} VALUE)

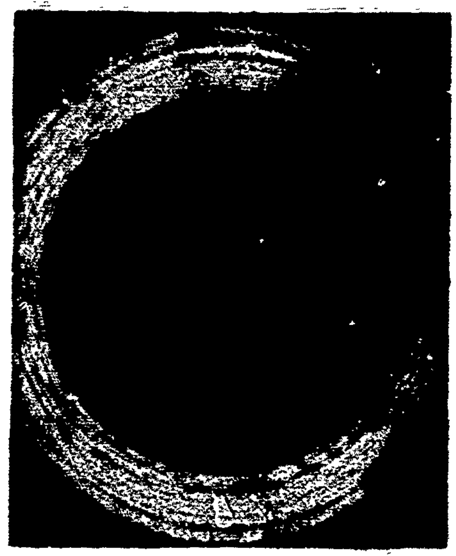

7X R-5

INADEQUATE FATIGUE NOTCH (HIGH K_{Ic} VALUE)

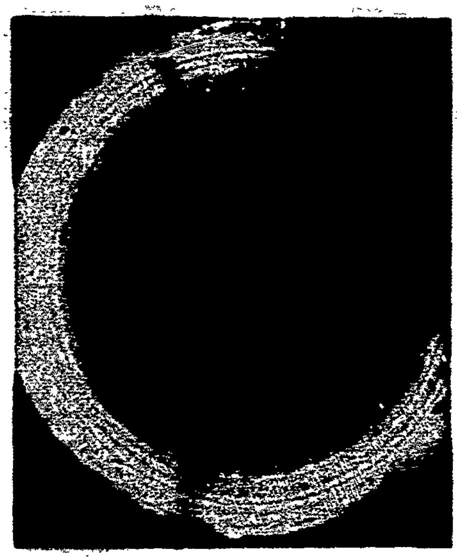

7X R-28

GOOD FATIGUE NOTCH (VALID K_{Ic} VALUE)

Figure 35: Sample Fractographs of Ladish D6A-C Sharply Notched Round Bar Specimens (Static Test)

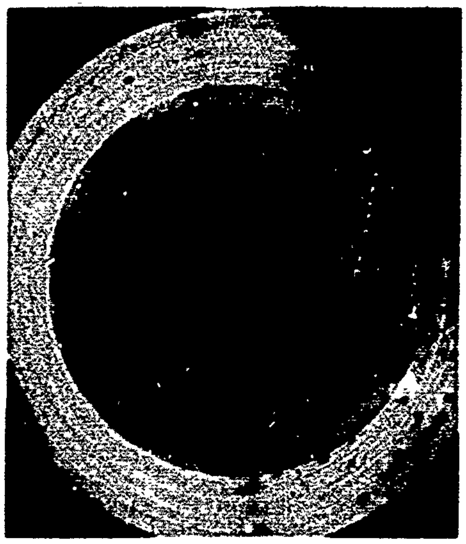

7X R-23

ECCENTRIC INITIAL AND FINAL CYCLIC FLAW EXTENSIONS

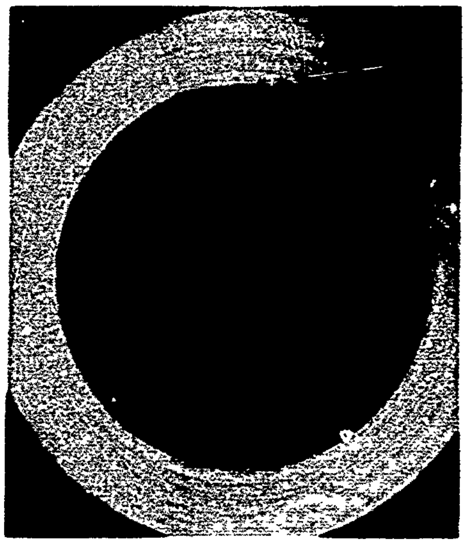

7X R-12

ADEQUATE FLAW EXTENSIONS

Figure 36: Sample Fractographs of Ladish D6A-C Steel Sharply Notched Round Bar Specimens (Cyclic Test)

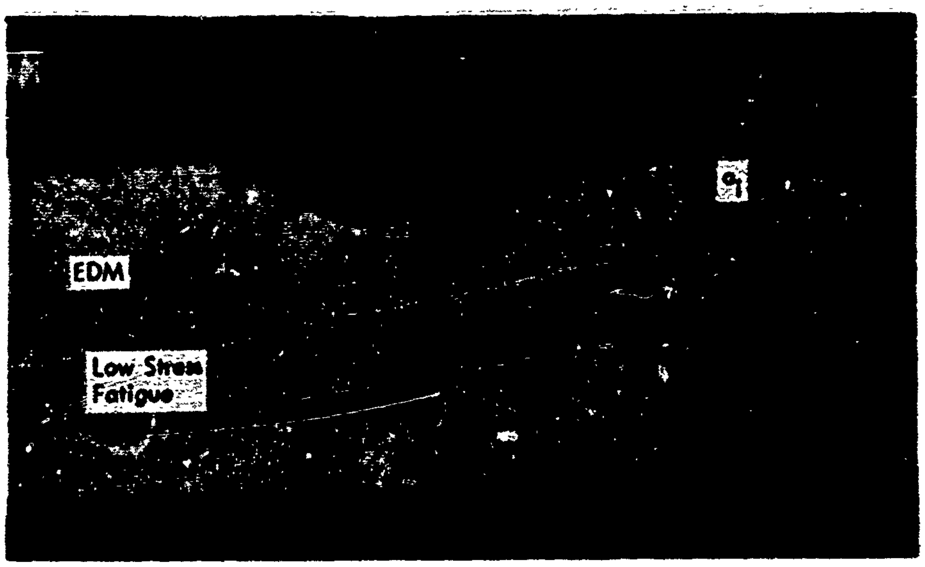

7X LS-1

STATIC TEST

7X LS-5

CYCLIC TEST

Figure 37: Sample Fractographs of Ladish D6A-C Steel Surface-Flawed Specimens

TESTED AT ROOM TEMPERATURE

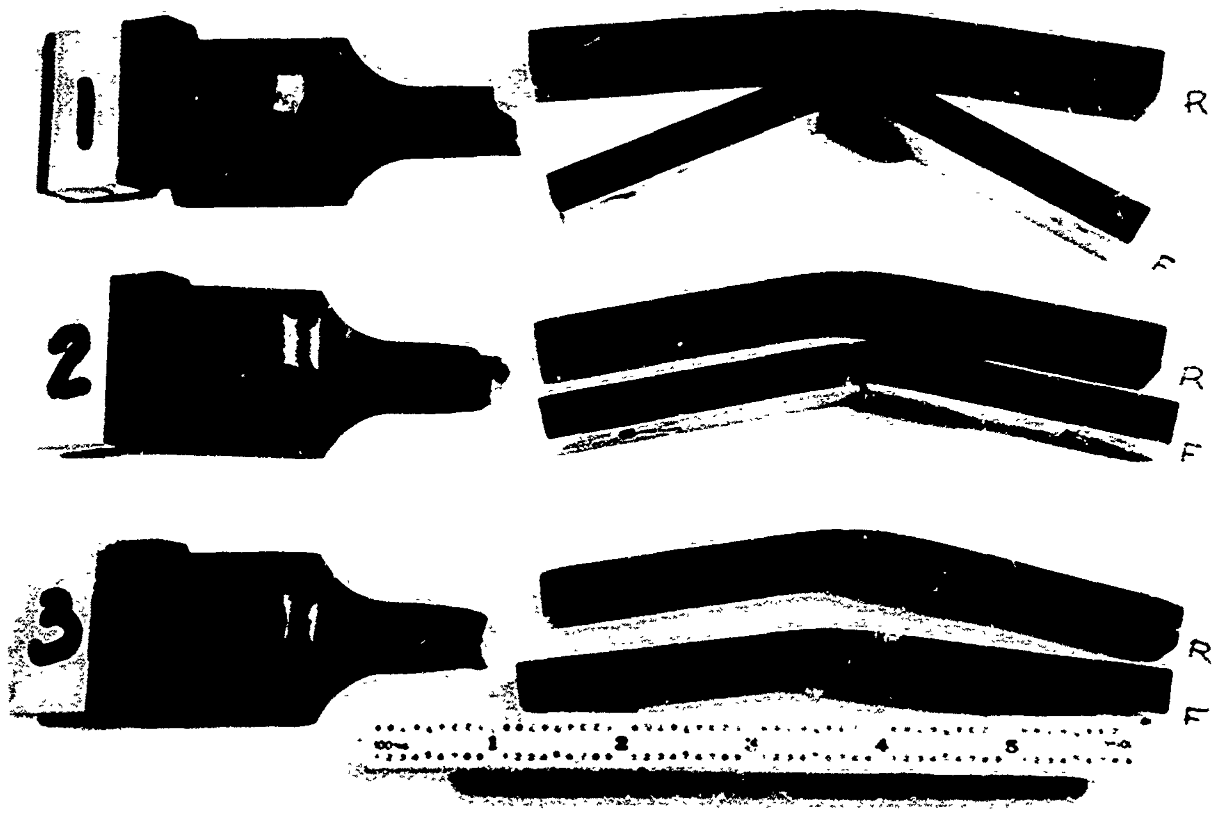

Figure 38: Tensile and Bend Weld Point Specimens of Ladish D6A-C Weld

TEST PANELS WELDED WITH DIFFERENT WELD WIRES

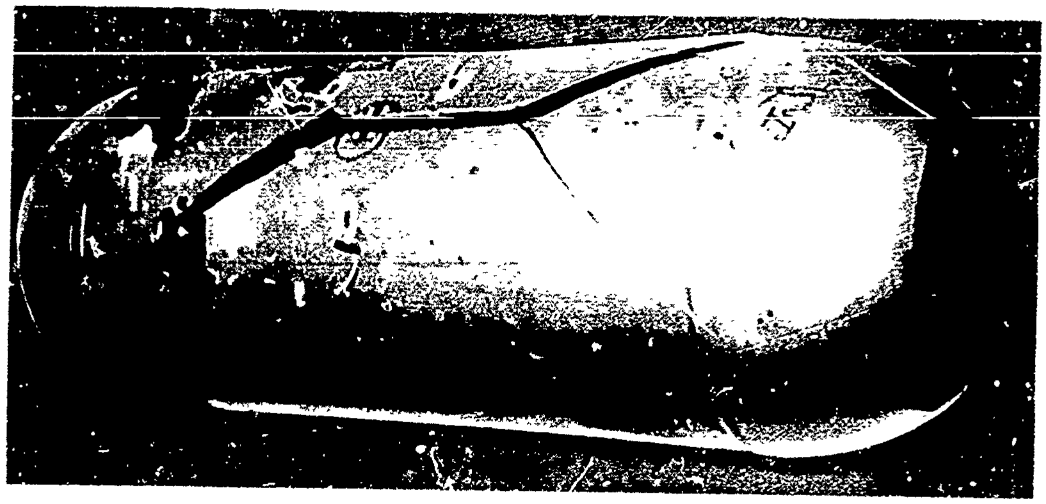

TANK I

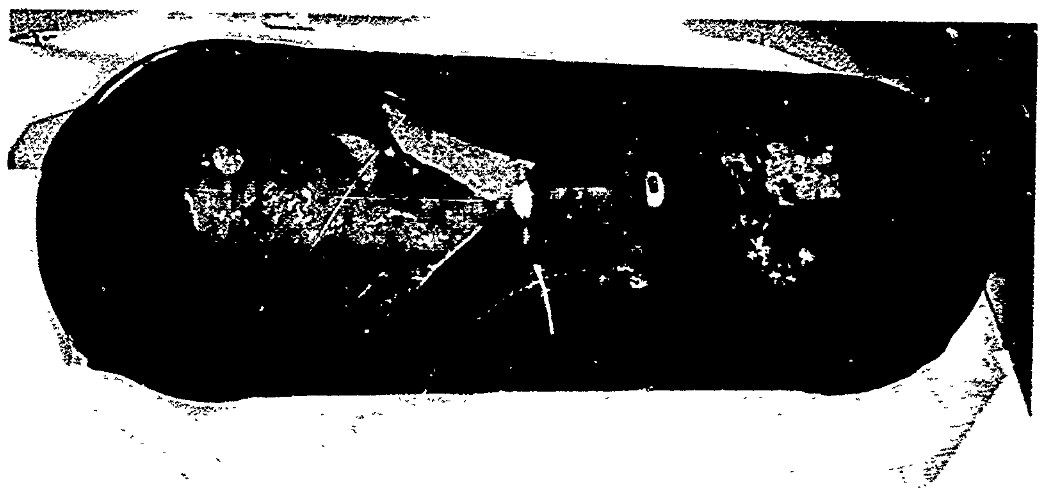

TANK II

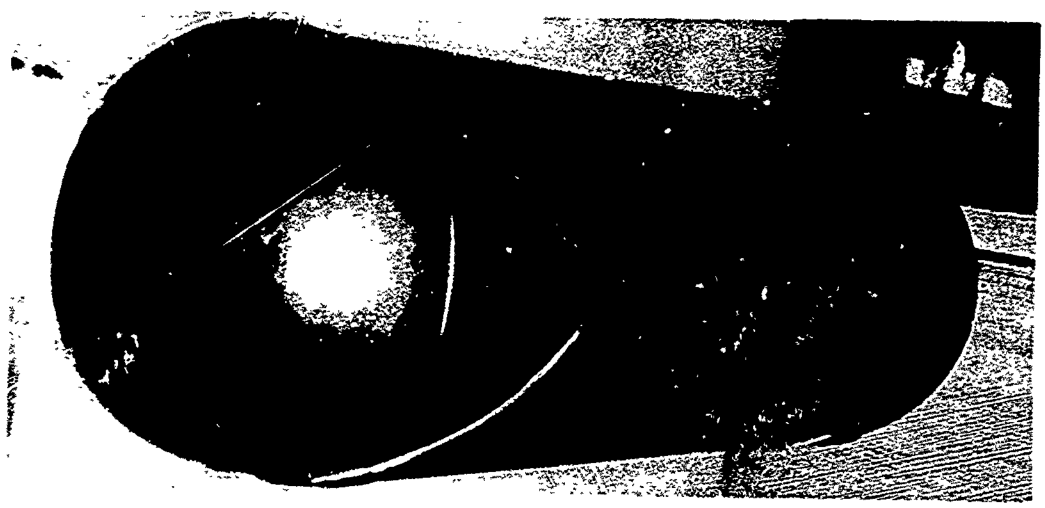

TANK III

Figure 39: Fractured Ladish D6A-C 17-Inch Diameter Tanks I, II, and III

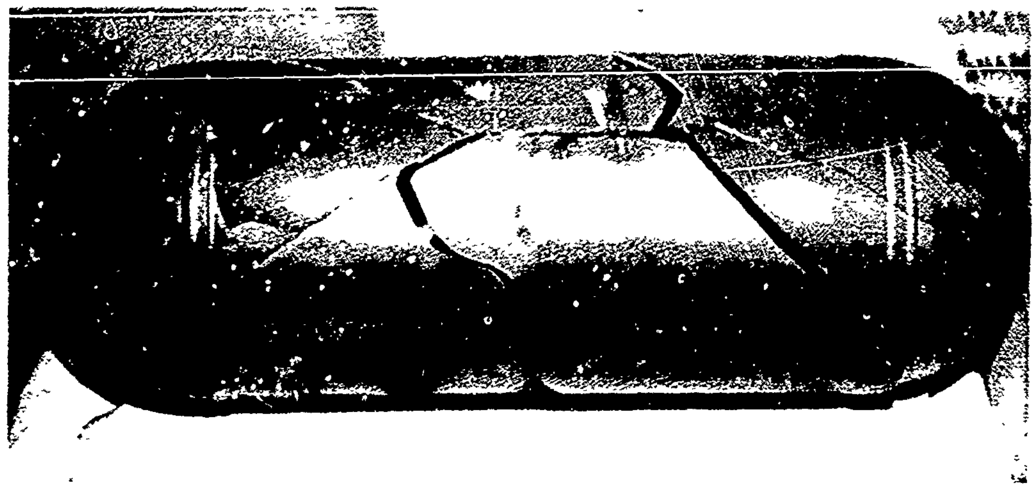

TANK IV

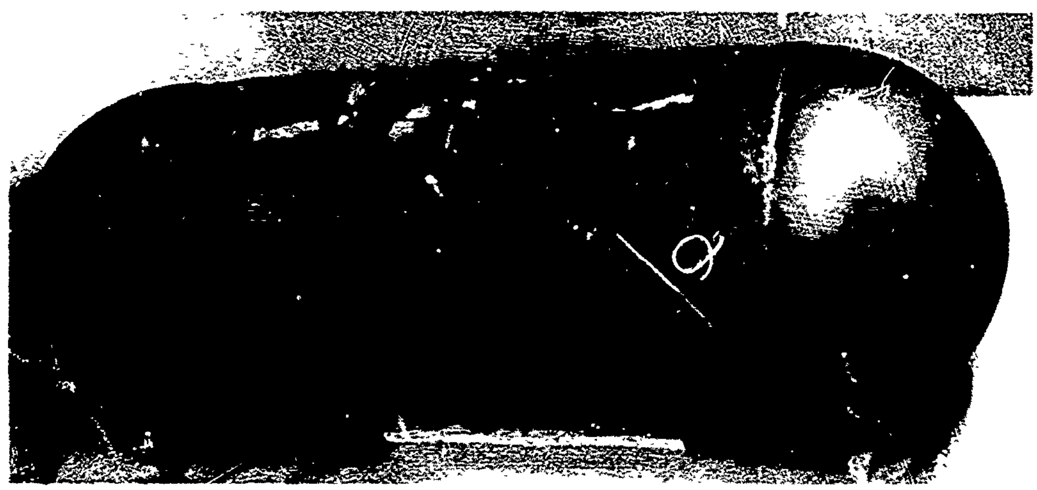

TANK V

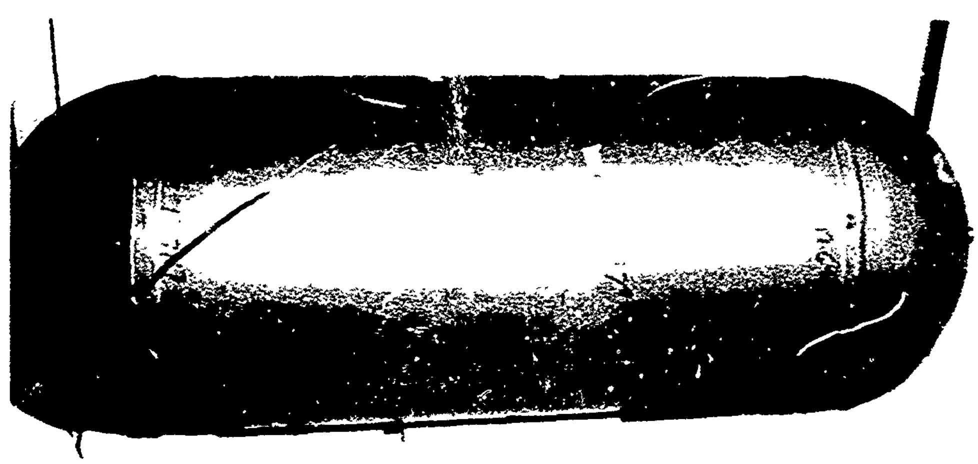

TANK VI

Figure 40: Fractured Ladish D6A-C 17-Inch Diameter Tanks IV, V, and VI

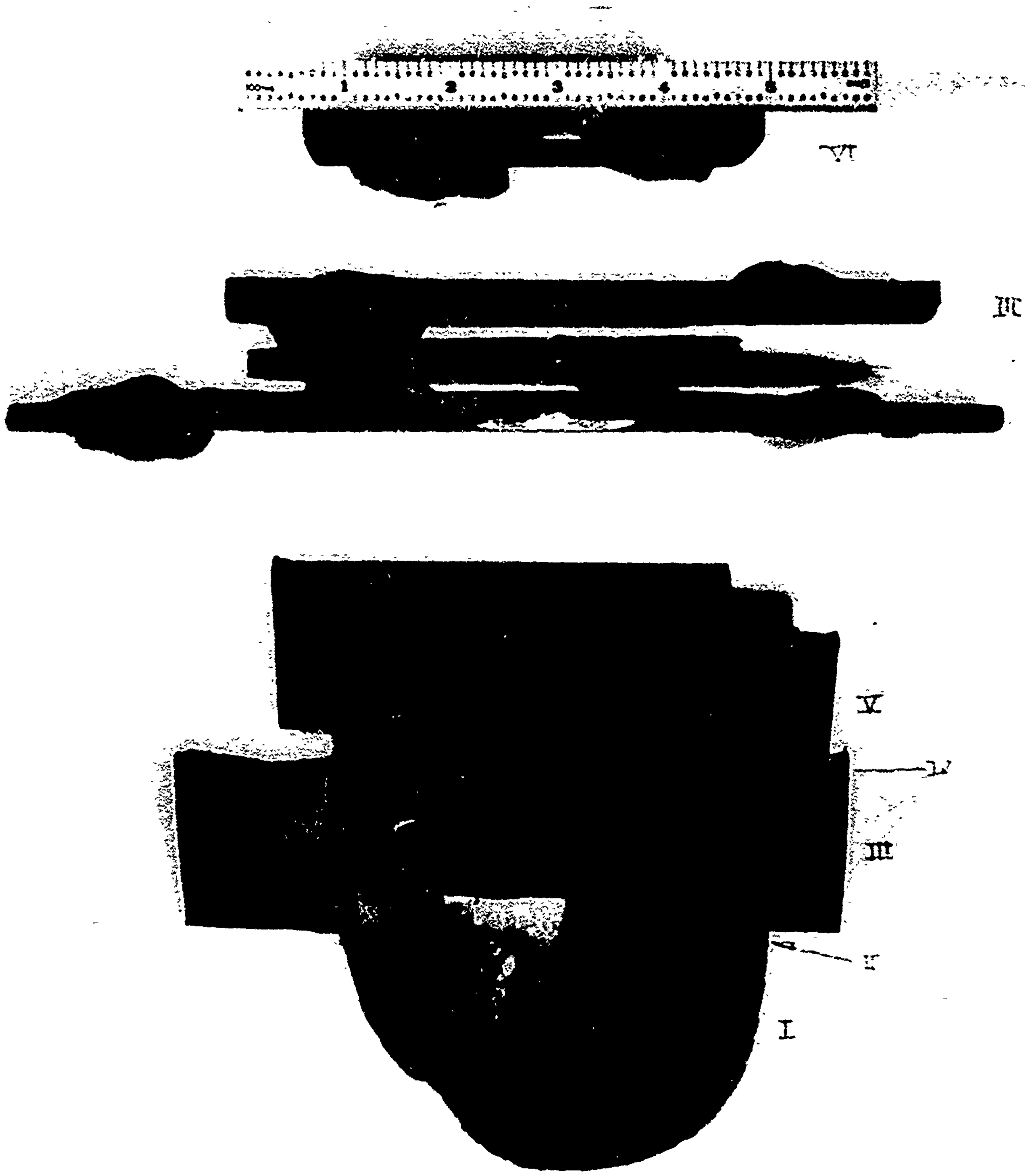

Figure 41: General Appearance of 17-Inch Diameter Tank Samples Containing Fracture Origin

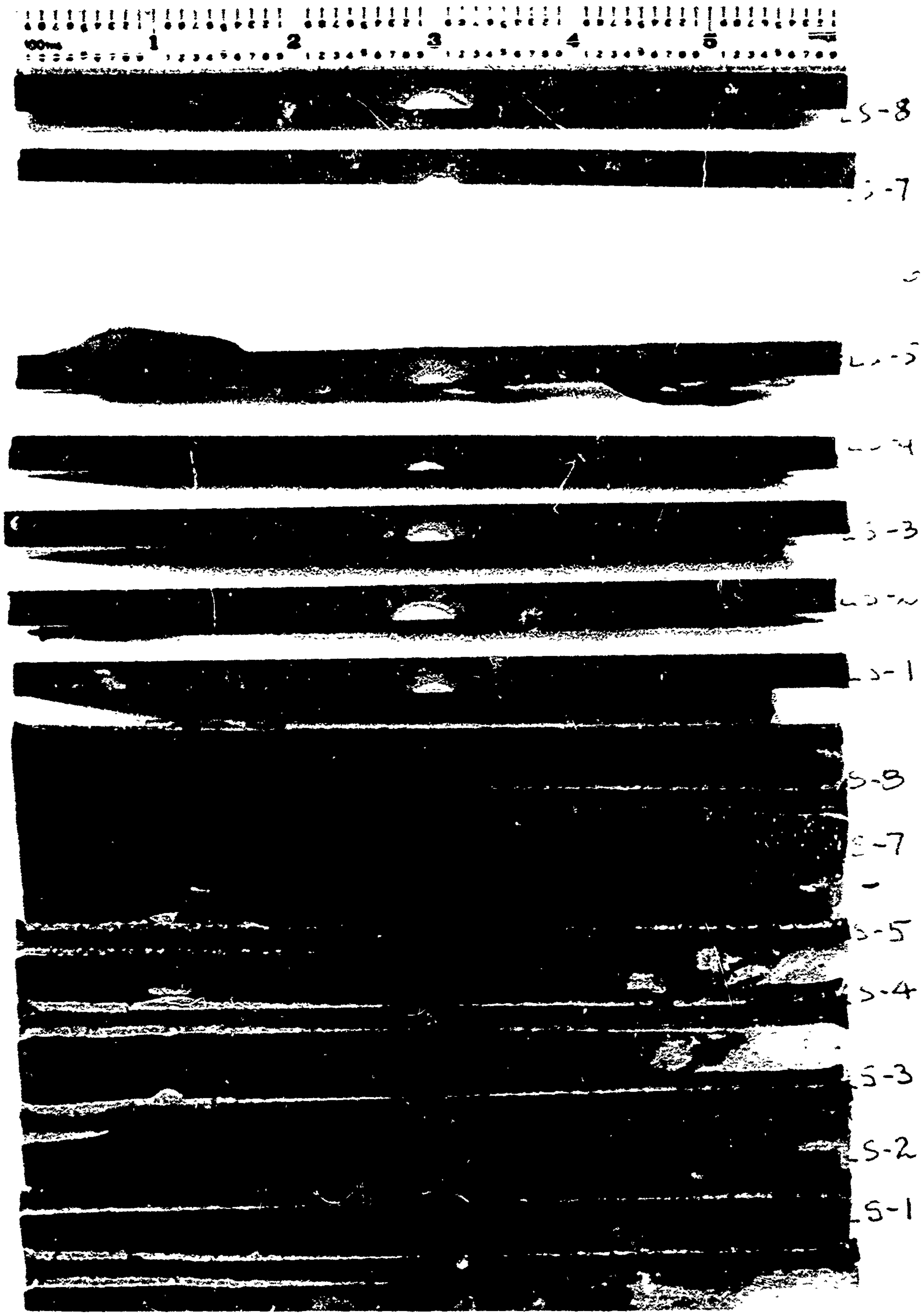

Figure 42: General Appearance of Ladish D6A-C Surface-Flawed Specimen Samples Containing Fracture Origin

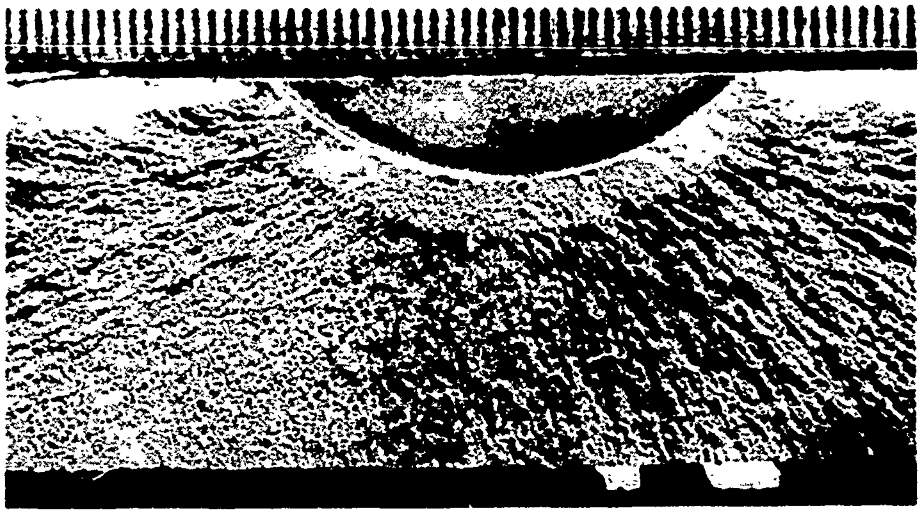

TANK I

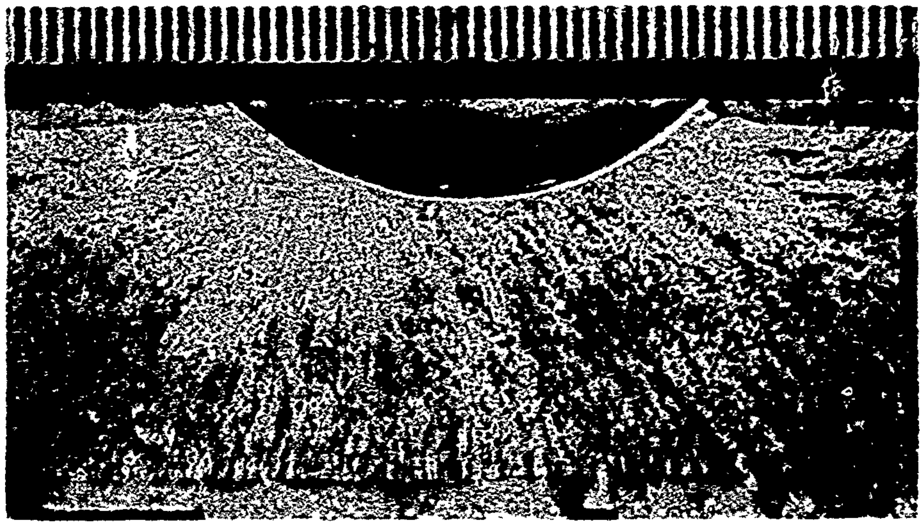

TANK II

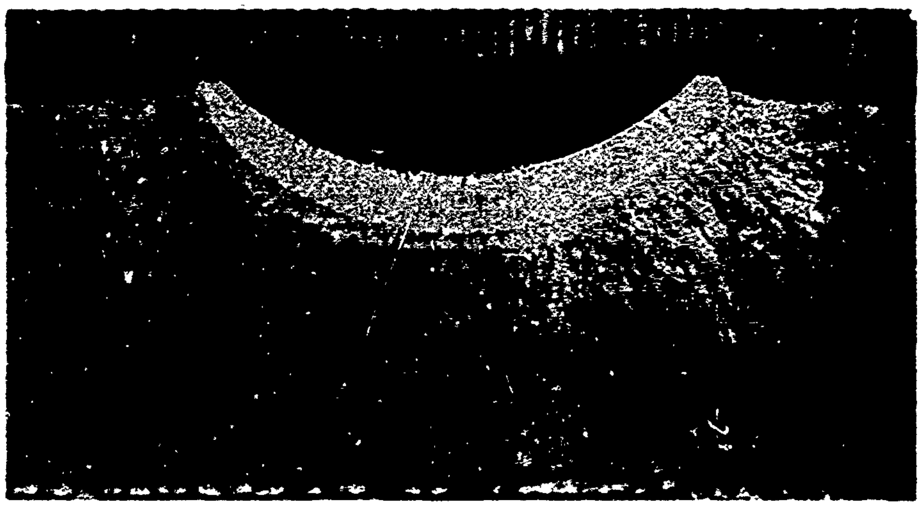

TANK III

Figure 43: Fractographs of Ladish D6A-C 17-Inch Diameter Tanks I, II, and III

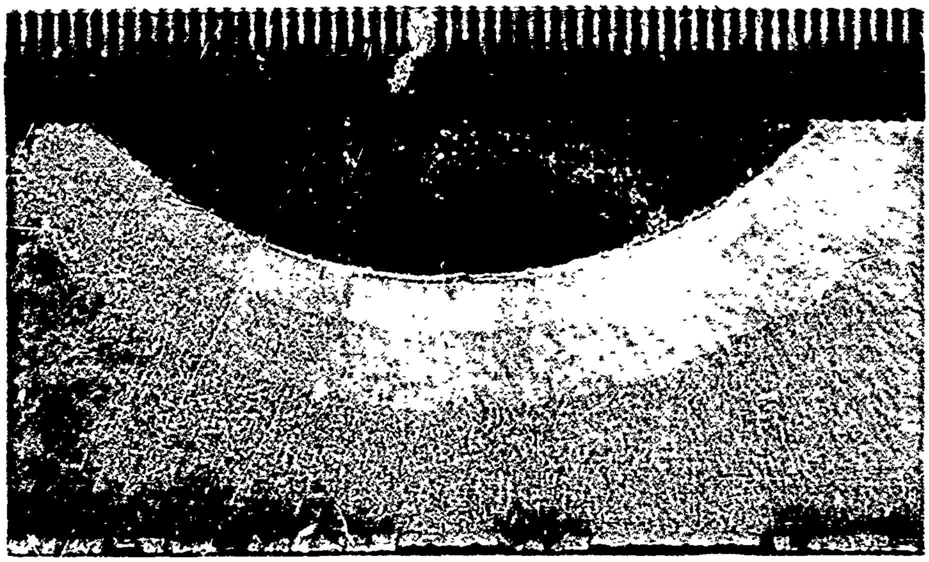

TANK IV

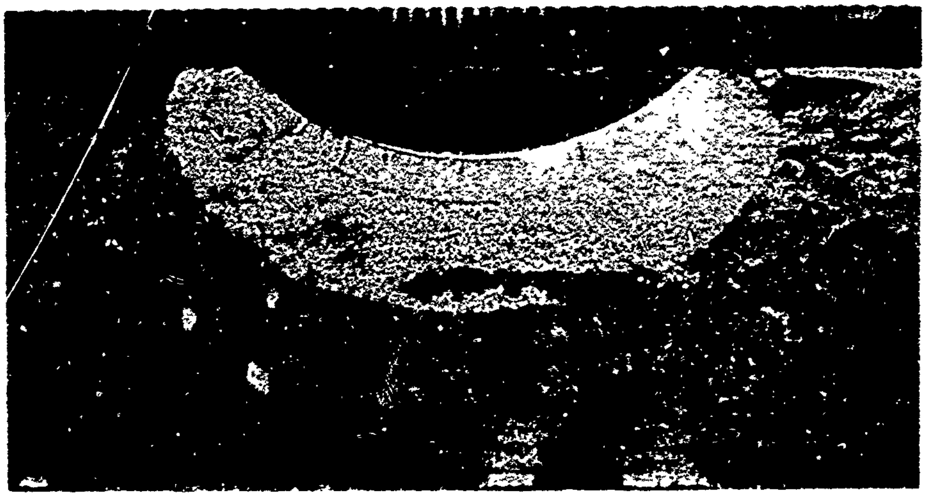

TANK V

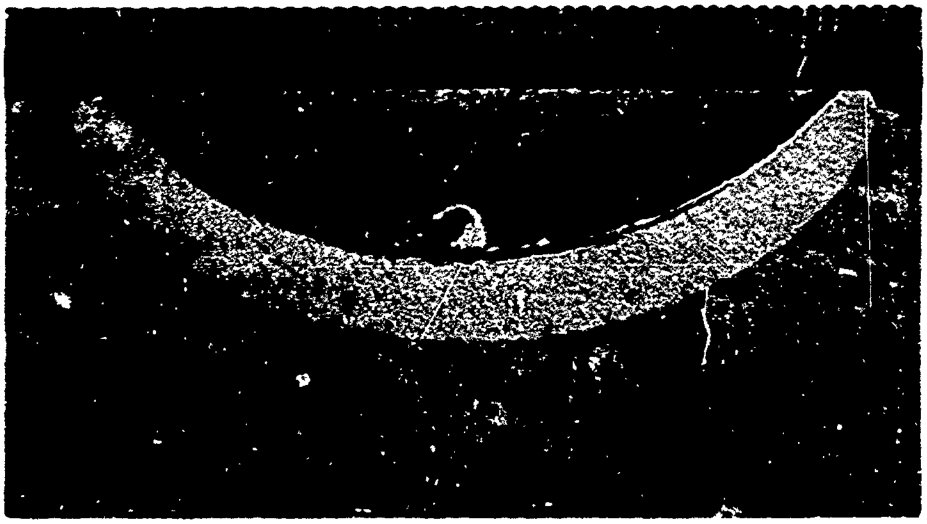

TANK VI

Figure 44: Fractographs of Ladish D6A-C 17-Inch Diameter Tanks IV, V and VI

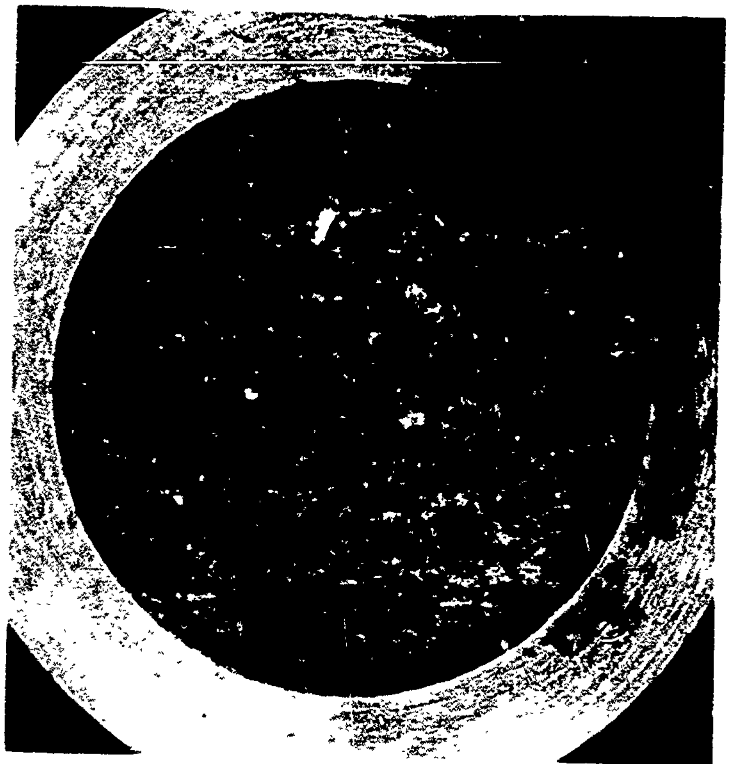

R-3 STATIC TEST 8X

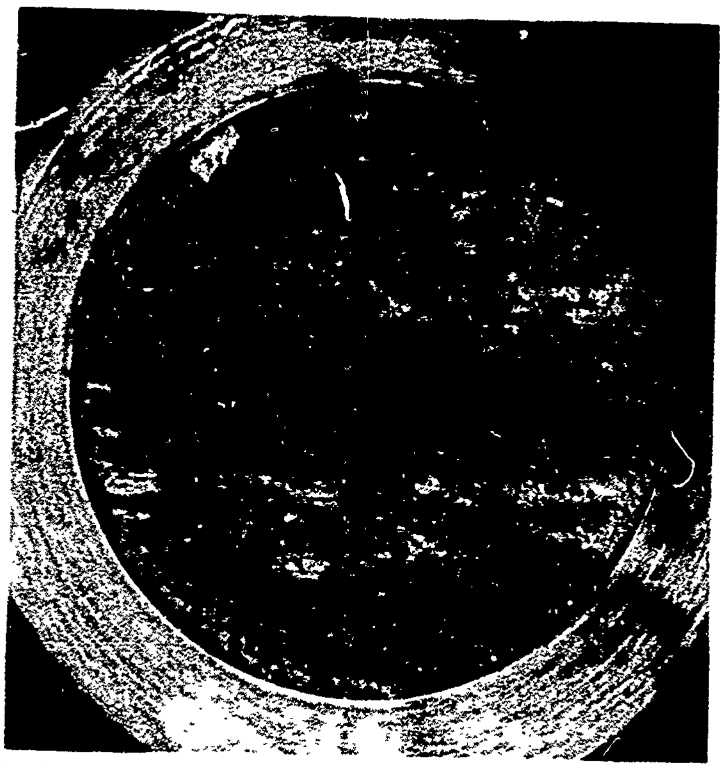

R-1 CYCLIC TEST 8X

Figure 45: Sample Fractographs of 6Al-4V Titanium Sharply Notched Round Bar Specimens

TESTED AT -320°F

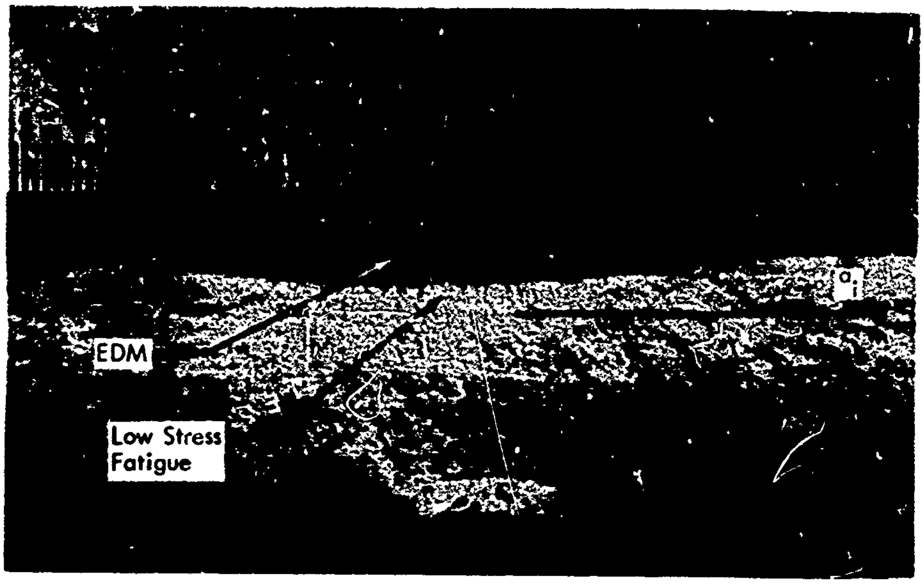

5X TS-4

STATIC TEST

5X TS-3

CYCLIC TEST

Figure 46: Sample Fractographs of 6Al-4V Titanium Surface-Flawed Specimens

TESTED AT -320°F

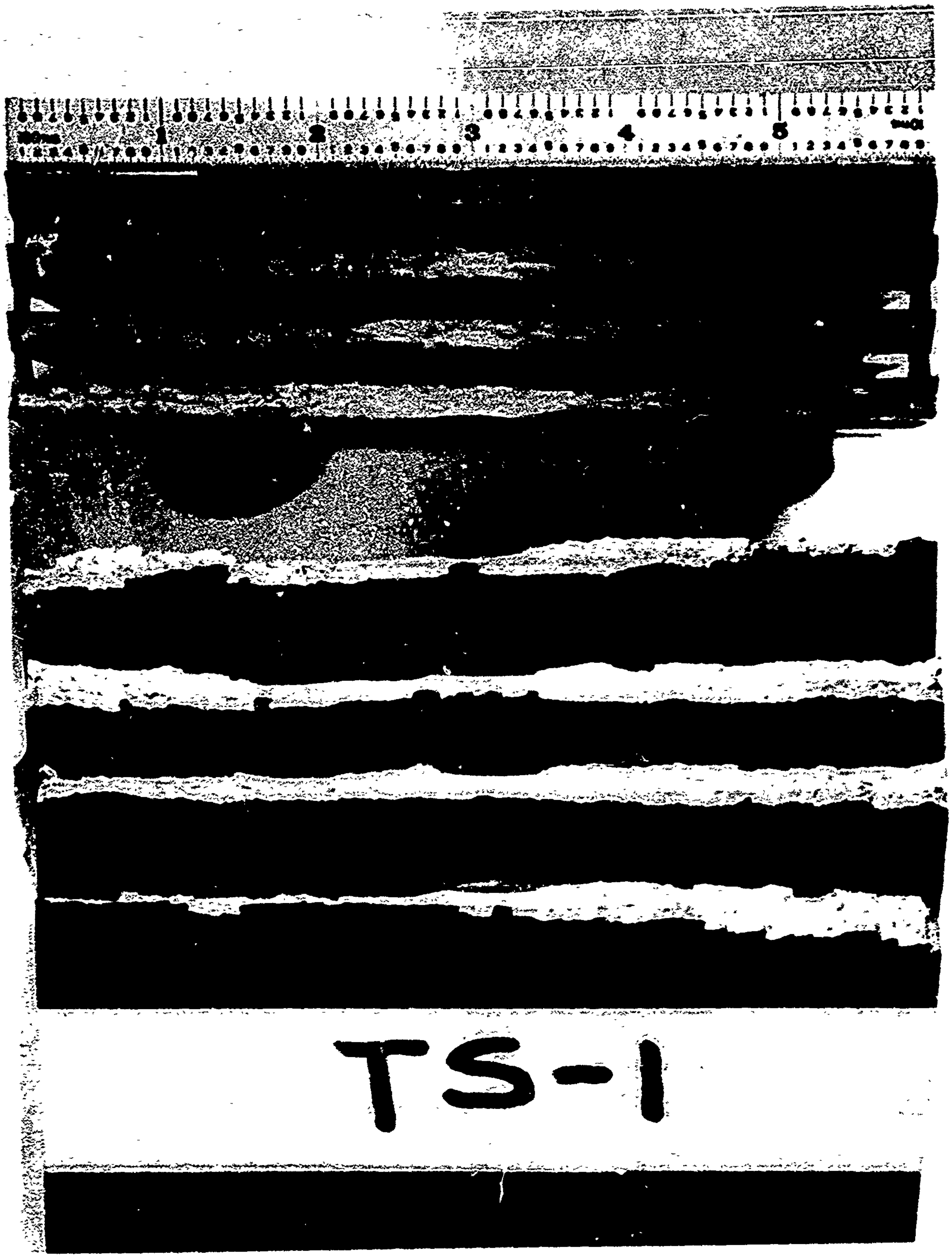

Figure 47: General Appearance of Fractured 6Al-4V Titanium Surface-Flawed Specimen

TESTED AT -320°F

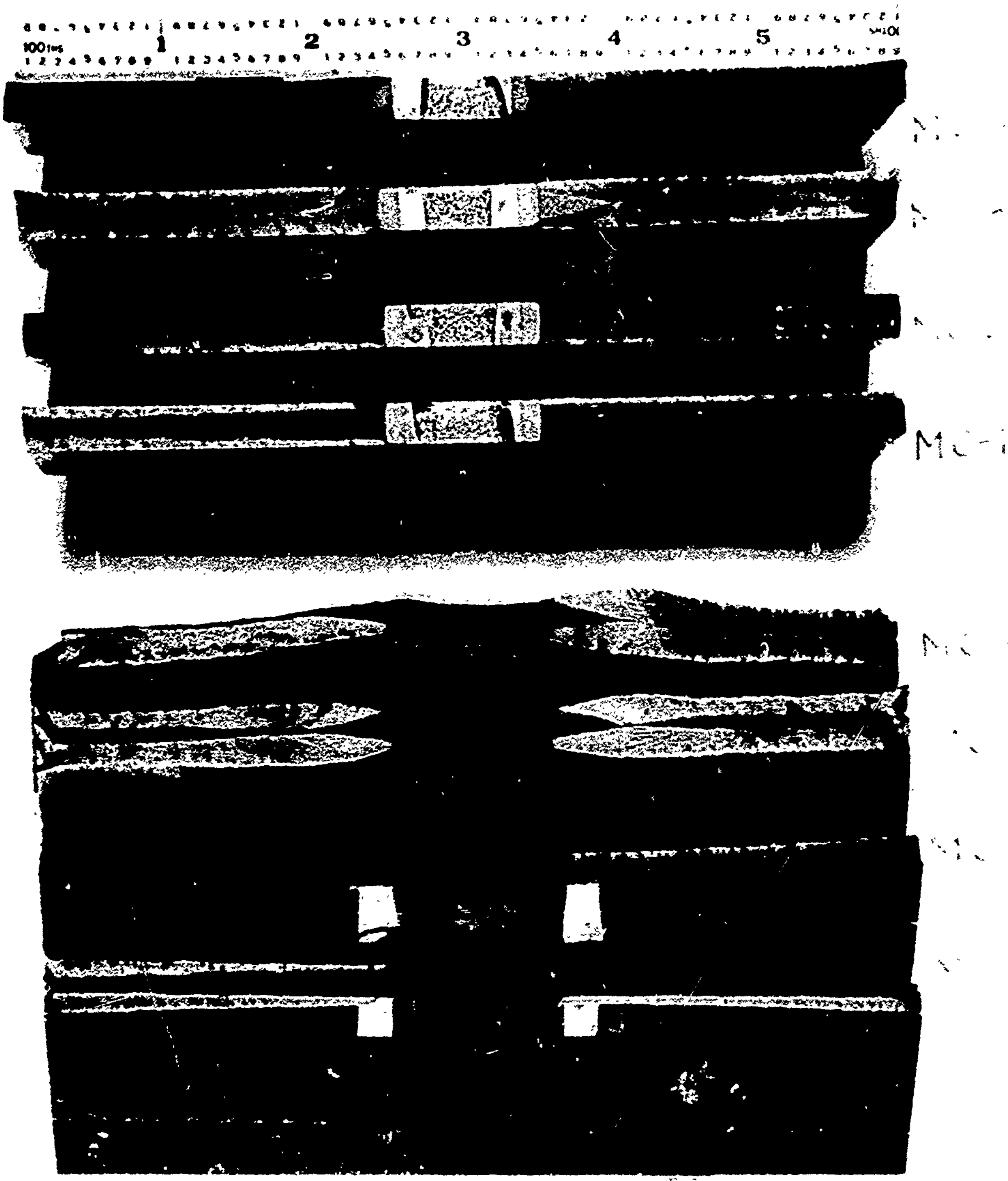

Figure 48: General Appearance of Fractured 18 Ni(300) Through-the-Thickness Cracked Specimens

TESTED AT ROOM TEMPERATURE

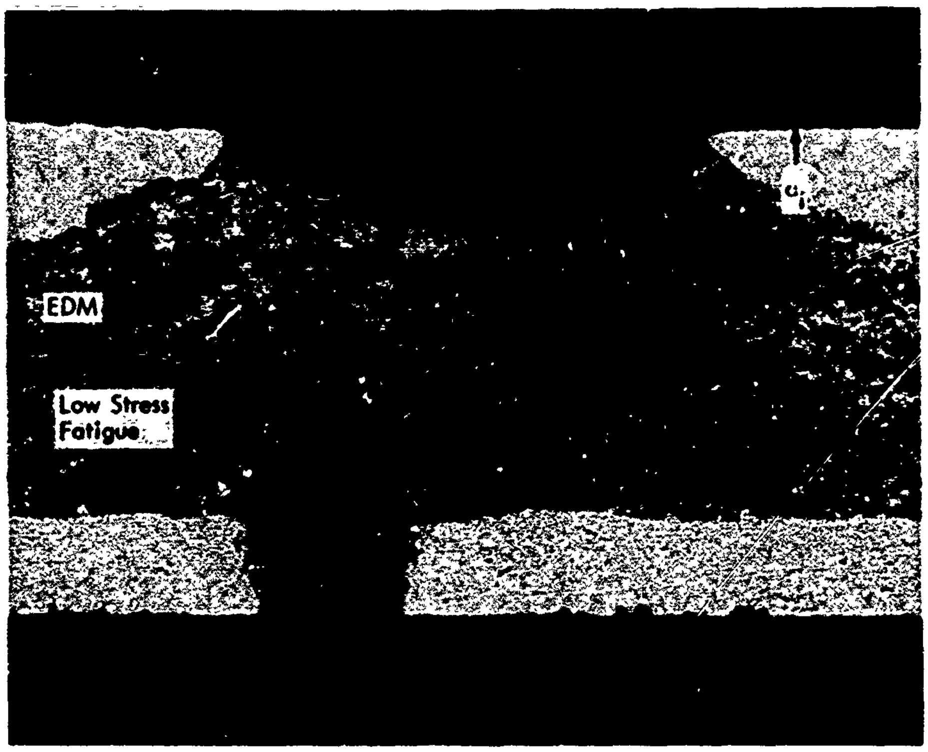

8X MS-1

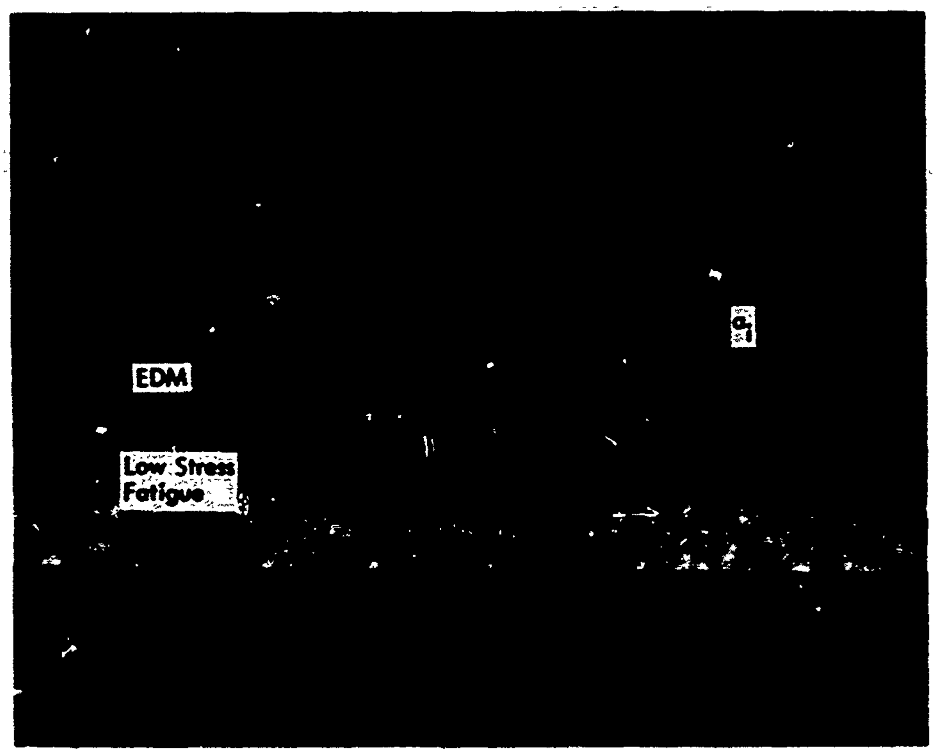

5X MC-5

Figure 49: Sample Fractographs of Surface-Flawed 18 Ni(300) Maraging Steel Specimens

TESTED AT ROOM TEMPERATURE (STATIC TEST)

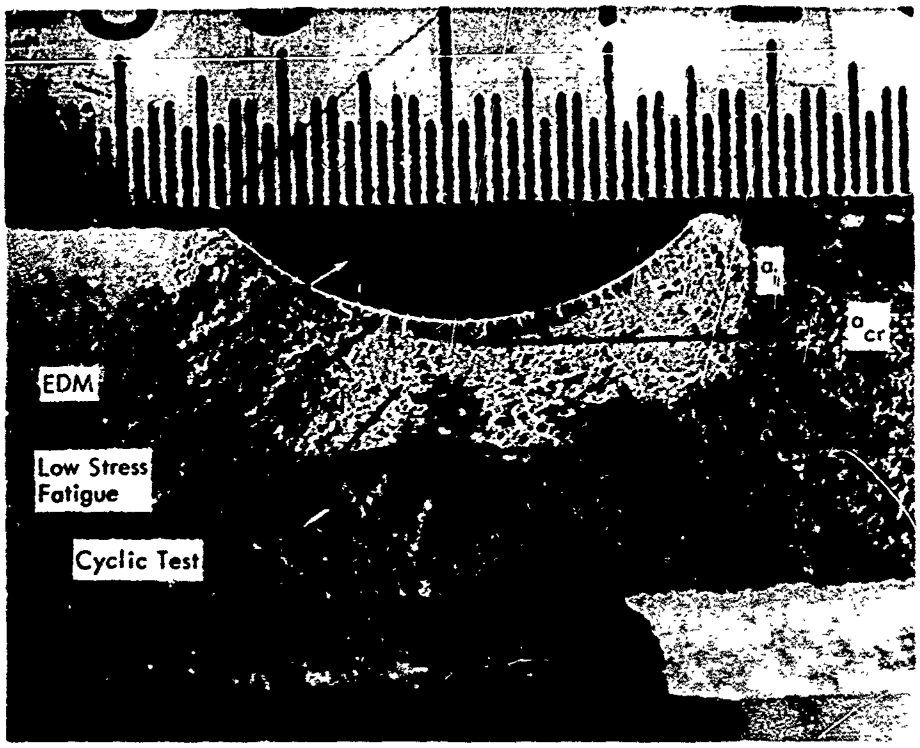

8X MC-8

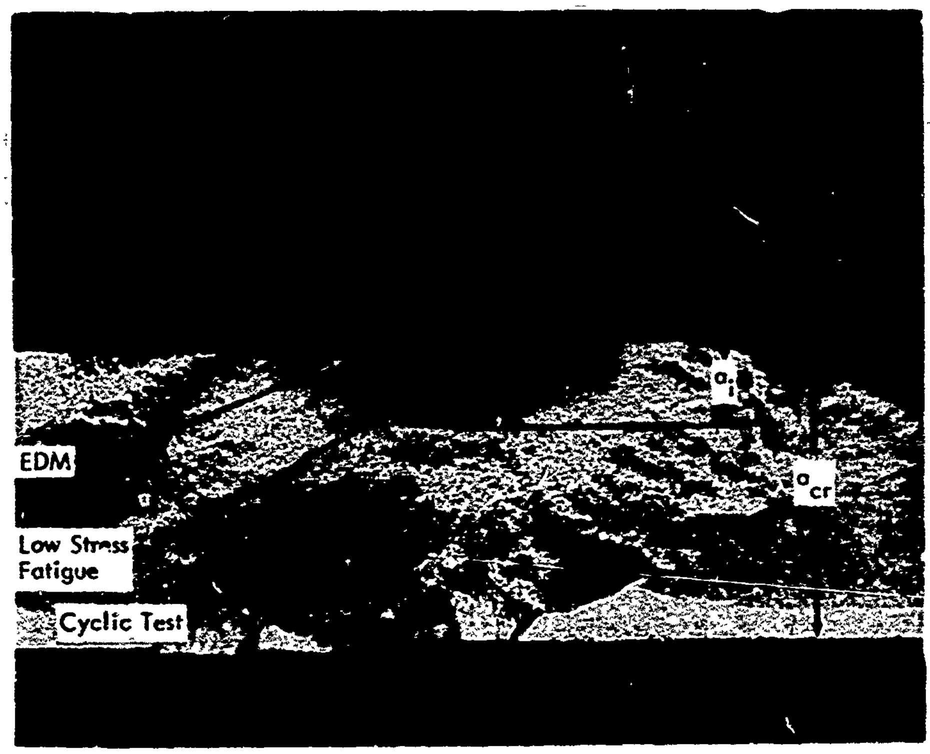

5X MC-2

Figure 50: Sample Fractographs of Surface-Flawed 18 Ni(300) Maraging Steel Specimens

TESTED AT ROOM TEMPERATURE (CYCLIC TEST)

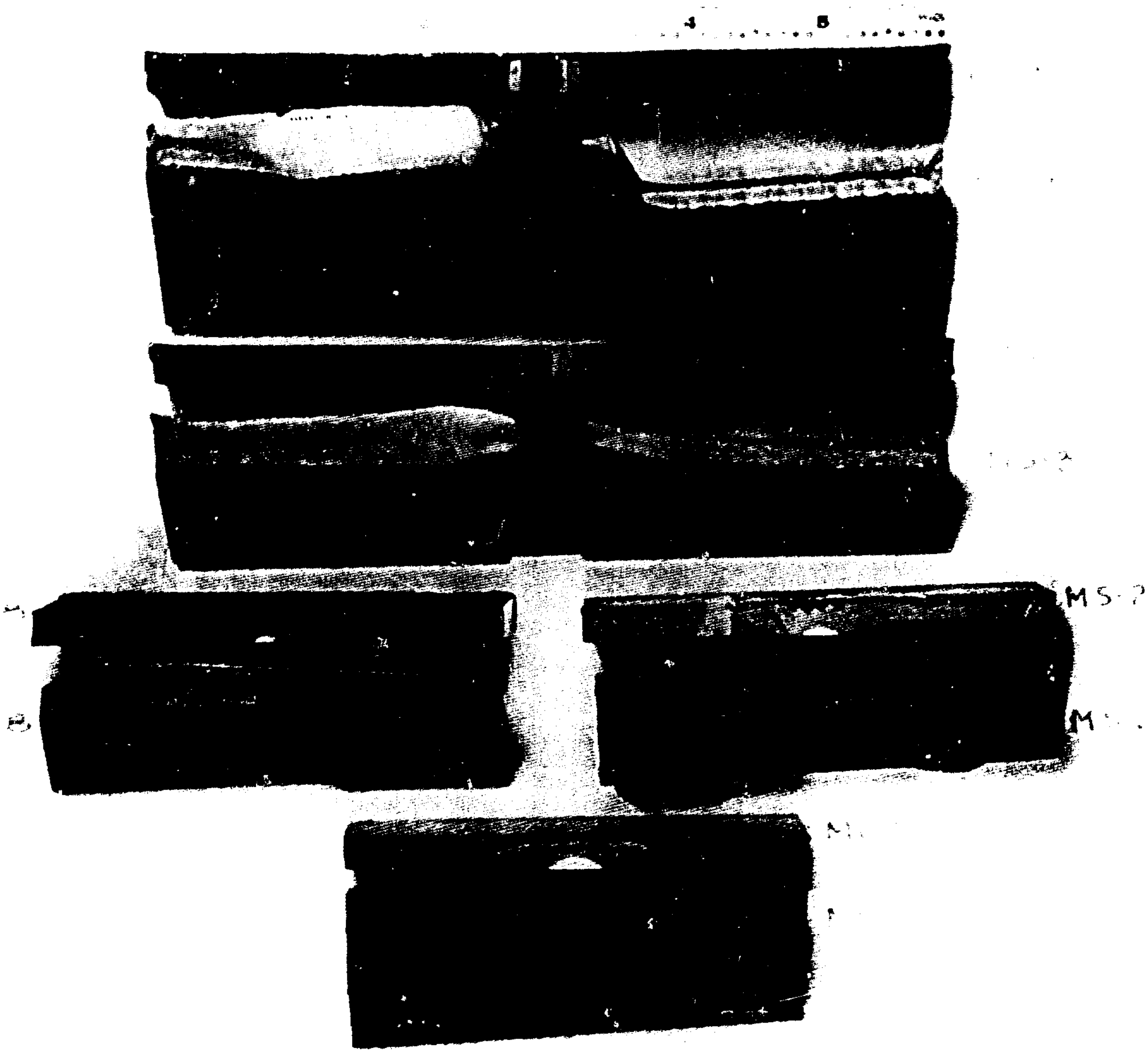

Figure 51: General Appearance of Fractured 18 Ni(300) Surface-Flawed Specimen

TESTED AT ROOM TEMPERATURE